

# Plasma-assisted conversion of carbon dioxide

Proefschrift voorgelegd tot het behalen van de  
graad van doctor in de wetenschappen: chemie  
aan de Universiteit Antwerpen te verdedigen door

**Igor Belov**

Promotor  
prof. dr. Annemie Bogaerts, PLASMANT



## Plasma-assisted conversion of carbon dioxide

Proefschrift voorgelegd tot het behalen van de graad  
doctor in de wetenschappen: chemie  
aan de Universiteit Antwerpen  
te verdedigen door

**Igor Belov**

Promotors:

prof. dr. Annemie Bogaerts, PLASMANT, Departement Chemie

dr. ir. Sabine Paulussen, SuMAT, VITO

Antwerp, 2017



## Acknowledgement

First of all, I would like to thank my supervisors Sabine Paulussen and Annemie Bogaerts for their amazing attitude and dedication to my project. I sincerely cannot imagine having better mentors. This work would not be possible without the team of VITO Plasma: Erwin Van Hoof, Danny Havermans, Pieter Lens, Jan Cools, Annick Vanhulsel, Bert Verheyde. I'm grateful to them for sustaining a friendly and cooperative work atmosphere and their willingness to discuss and help me with research and technical problems. Achim von Keudell and Anna Maszl-Kantner were leading the organization of the RAPID project and I'm grateful to them and other RAPID PI's for the opportunity to receive a Marie Curie grant and participate in numerous interesting workshops. Raymond Kemps and Myrjam Mertens performed SEM, EDX, STEM, XRD measurements used in this thesis, while their ideas and advice were crucial for my project. Vincent Vermeiren and Antonin Berthelot from the PLASMANT group of University Antwerp helped with the simulation of the MW plasma system. I'm grateful to Philip Martin, Christopher Whitehead and Shaojun Xu for hosting my research visit to Manchester University. Maurits Ceuppens and Carine Vanloffelt made sure that my stay at VITO was as smooth as possible. Ivo Thijs provided me with the most important thing in Boeretang: VITO-bike.

Jens Vanneste and Simge Danaci were fellow VITO students, with whom I could arrange novel experiments, discuss project ideas and talk about everyday struggles of PhD life. Special gratitude goes to RAPID fellows, the group of people, with whom we only talk about plasma. I would like to acknowledge Petr, Tatiana, Claudia, Sam, Julia, Alexey, Enrique and other members of the Boeretang Kingdom community for being with me during these 3 years.

Lastly, I would like to thank my family for all their love and encouragement.



---

## Contents

<b>List of figures</b>	<b>v</b>
<b>List of tables</b>	<b>x</b>
<b>Chapter 1 Introduction</b>	<b>1</b>
1-1 Introduction	2
1-2 Plasma and CO <sub>2</sub>	3
1-3 Plasma-based CO <sub>2</sub> conversion	4
1-3-1 Dielectric Barrier Discharge systems	5
1-3-2 Why is the CO <sub>2</sub> conversion in a DBD inherently limited?_	8
1-3-3 Control over E/n	10
1-3-4 Microwave (MW) discharge reactors	11
1-3-5 Gliding arc plasma systems	13
1-4 Aim and Outline of the PhD Dissertation	15
<b>Chapter 2 Experimental</b>	<b>17</b>
2-1 DBD reactor set-up	18
2-1-1 Reactor set-up	18
2-1-2 MD and DD configuration of the DBD	19
2-1-3 Overpressured DBD set-up	21
2-2 MW discharge system	22
2-2-1 Reactor design	22
2-2-1 Microwave system	22
2-2-2 Gas supply and vacuum scheme	24
2-3 Process control, diagnostics and analytical techniques	24
2-3-1 Power measurement	24
2-3-2 Gas chromatography (GC) analysis	25
2-3-3 Optical emission spectroscopy (OES)	26

2-3-4	Material preparation and characterisation _____	26
<b>Chapter 3 Influence of the electrode surface on the CO<sub>2</sub> conversion in a DBD _____</b>		<b>28</b>
3-1	Introduction _____	29
3-2	System description _____	31
3-3	Electrical characteristics for the MD configuration _____	32
3-3-1	Effect of the conductive film on the discharge properties _____	37
3-4	Comparison of DD and MD configurations _____	41
3-4-1	Discharge characterisation in the various configurations _____	41
3-4-2	CO <sub>2</sub> conversion in the various configurations. _____	45
3-4-3	OES spectra in the various configurations _____	47
3-5	Discussion _____	49
3-6	Conclusion _____	53
<b>Chapter 4 CO and CO<sub>2</sub> DBDs _____</b>		<b>54</b>
4-1	Introduction _____	55
4-2	System description _____	57
4-3	Discharge comparison: electrical signals _____	57
4-4	Discharge comparison: gas phase analysis _____	59
4-5	Discharge comparison: optical emission spectroscopy _____	62
4-6	Solid products analysis _____	66
4-6-1	Morphology and elemental composition _____	66
4-6-2	Structural characterization _____	69
4-7	Discussion _____	75
4-7-1	CO discharge and COd sample _____	75
4-7-2	CO <sub>2</sub> discharge and CO <sub>2</sub> d sample _____	77
4-7-3	Can we produce carbon materials by means of atmospheric pressure CO <sub>2</sub> plasma? _____	80

---

4-8	Conclusions	81
<b>Chapter 5 Pressure as a control handle for atmospheric plasma processes</b>		<b>83</b>
5-1	Introduction	84
5-2	System description	86
5-2-1	Deposition experiment	86
5-2-2	Conversion experiment	86
5-3	Results	87
5-3-1	O <sub>2</sub> DBD and its production rate of nanopowder	87
5-3-2	CO <sub>2</sub> DBD and its conversion	93
5-4	Discussion	97
5-4-1	How can pressure stimulate the single microdischarge current in the O <sub>2</sub> and CO <sub>2</sub> DBDs?	97
5-4-2	How can pressure stimulate deposition of nanopowder in the O <sub>2</sub> DBD?	98
5-4-3	How can a pressure increase stimulate CO <sub>2</sub> conversion?	101
5-5	Conclusion	102
<b>Chapter 6 Carbon Dioxide Dissociation in a Microwave Plasma Reactor</b>		<b>103</b>
6-1	Introduction	104
6-2	System description	105
6-3	Results and discussion	108
6-3-1	Effect of the pressure	108
6-3-2	Effect of the flow rate in the vortex configuration	111
6-3-3	CO <sub>2</sub> conversion in the MW discharge at 200 mbar	112
6-3-4	Post-discharge temperature measurement	115
6-3-5	Analysis and comparison with literature results	120
6-4	Conclusion	127

<b>Chapter 7 Conclusion and outlook</b>	<b>129</b>
7-1 Properties of microdischarges and CO <sub>2</sub> conversion	130
7-2 CO <sub>2</sub> conversion in MW plasma	131
7-3 How can we further improve the CO <sub>2</sub> decomposition process?	132
<b>Summary</b>	<b>135</b>
<b>Samenvatting</b>	<b>136</b>
<b>List of Peer-Reviewed Publications</b>	<b>138</b>
<b>List of Conference Contributions</b>	<b>139</b>
<b>References</b>	<b>140</b>

## List of figures

<b>Figure 1-1.</b> Common dielectric barrier discharge configurations (taken from <sup>[25]</sup> ).	5
<b>Figure 1-2.</b> Fractional electron energy transferred to different channels of excitation, ionization and dissociation of CO <sub>2</sub> , as a function of the reduced electric field (E/n) (taken from <sup>[48]</sup> ).	9
<b>Figure 1-3.</b> Schematic representation of a MW configuration (taken from <sup>[52]</sup> ).	11
<b>Figure 1-4.</b> Conventional gliding arc, schematic image (left, where i-ignition point, ii-point of developed gliding arc, iii-extinction zone) and picture of the flat GA discharge	13
<b>Figure 2-1.</b> Dielectric barrier discharge reactor in the a) Metal-Dielectric (MD) and b) Double Dielectric (DD) configuration.	20
<b>Figure 2-2.</b> Experimental setup of the tubular Dielectric Barrier Discharge reactor used for a) nanomaterial production in O <sub>2</sub> DBD and b) gas conversion in CO <sub>2</sub> DBD, when using overpressure.	21
<b>Figure 2-3.</b> Drawing and photo of the MW discharge system.	23
<b>Figure 2-4.</b> Gas supply and vacuum scheme of the set-up.	24
<b>Figure 3-1.</b> Electrical signal of the DBD reactor in the MD configuration: (a) CO <sub>2</sub> ; (b) O <sub>2</sub> ; (c) N <sub>2</sub> (discharge power: 180W; feed flow rate: 0.2 SLM; frequency: 30 kHz for all three cases; dielectric material: alumina).	33
<b>Figure 3-2.</b> Electrical signal in one period of applied voltage for the CO <sub>2</sub> discharge (discharge power: 180W; feed flow rate: 0.2 SLM; frequency: 30 kHz; dielectric material: alumina).	34
<b>Figure 3-3.</b> Measured current and voltage signal for positive (a) and negative (b) HC (180W-0.2 SLM CO <sub>2</sub> -30 kHz).	35
<b>Figure 3-4.</b> Electrical signal of the CO <sub>2</sub> DBD reactor, without the coating (a) and with the coated walls (b) (discharge power: 60W; feed flow rate: 0.6 SLM; frequency: 4 kHz; dielectric material: alumina).	39

**Figure 3-5.** Charge transfer induced by the high-amplitude component of the discharge current (Discharge current > 35 mA) for the cases of 150W, 70W, 20W – 4 kHz power input at 0.6 SLM CO<sub>2</sub>. .....40

**Figure 3-6.** Comparison of the current waveforms in various reactor configurations (discharge power: 180W; CO<sub>2</sub> feed flow rate: 0.2 SLM; frequency (from left to right): 30 kHz; 25 kHz; 1 kHz; dielectric material: alumina). .....42

**Figure 3-7.** Lissajous figures of the CO<sub>2</sub> DBD in the DD configurations, with clean and coated dielectric surface (discharge power: 180W; feed flow rate: 0.2 SLM; frequency: 30 kHz; dielectric material: alumina). .....43

**Figure 3-8.** Comparison of current measurement by means of the Rogowski coil (red) and the derivative of the capacitor probe charge measurements (grey) of the total current (a) and the discharge current (b) achieved after subtraction of the displacement current. CO<sub>2</sub> DBD in the DD configurations, with coated dielectric surface (discharge power: 180W; feed flow rate: 0.2 SLM; frequency: 30 kHz; dielectric material: alumina). .....44

**Figure 3-9.** CO<sub>2</sub> conversion rate for the different DBD configurations, as a function of SEI (frequency: 10-30 kHz; dielectric material: alumina). .....46

**Figure 3-10.** Emission spectra of the CO<sub>2</sub> DBD in MD, coated DD and clean DD configurations (discharge power: 180W; feed flow rate: 0.2 SLM; frequency: 30 kHz; dielectric material: alumina). .....47

**Figure 3-11.** Emission spectra of the CO<sub>2</sub> DBD, in the three different configurations, normalized at 368 nm (discharge power: 180W; feed flow rate: 0.2 SLM; frequency: 30 kHz; dielectric material: alumina). .....48

**Figure 4-1.** Electrical signal of the (a) CO<sub>2</sub> and (b) CO DBD (Discharge power: 600 W; gas flow rate: 1 SLM; frequency: 50 kHz). .....59

**Figure 4-2.** Molar concentrations of the CO<sub>2</sub> discharge products as a function of the specific energy input (SEI). .....60

**Figure 4-3.** Measured optical signals of a DBD plasma in (a) CO<sub>2</sub>; (b) CO; and (c) O<sub>2</sub> at 600 W and 1 SLM gas flow rate. .....62

---

<b>Figure 4-4.</b> Emission spectrum of the CO discharge at 400 W and various feed flow rates (normalized at 482.8 nm).....	64
<b>Figure 4-5.</b> SEM images of the CO and CO <sub>2</sub> discharge products (denoted as COd and CO2d) at 600 W and 1 SLM (9.1 eV/molecule). ....	67
<b>Figure 4-6.</b> SEM image of the CO discharge product (COd) at 400 W and 0.25 SLM (24.3 eV/molecule).....	68
<b>Figure 4-7.</b> STEM image of nanoparticles agglomerate formed in the CO <sub>2</sub> discharge at 600 W and 1 SLM (9.1 eV/molecule).....	68
<b>Figure 4-8.</b> FTIR spectra of the COd and CO2d samples, formed at 600 W and 1 SLM (9.1 eV/molecule).....	70
<b>Figure 4-9.</b> FTIR spectra of the COd sample, formed at 400 W and various gas flow rates.....	70
<b>Figure 4-10.</b> Raman spectra of the COd and CO2d samples, formed at 600 W and 1 SLM (9.1 eV/molecule).....	73
<b>Figure 4-11.</b> XRD spectra of the COd and CO2d samples, formed at 6000 W and 1 SLM (9.1 eV/molecule).....	74
<b>Figure 5-1.</b> Electrical signal of the O <sub>2</sub> DBD at (a) 1.13 and (b) 1.7 bar pressure; Discharge power: 650 W; gas flow rate: 1 SLM .....	88
<b>Figure 5-2.</b> Discharge current, represented by the average current pulse (ACM), in the positive HC of the O <sub>2</sub> DBD upon increasing pressure.....	88
<b>Figure 5-3.</b> Images of 1 SLM O <sub>2</sub> DBD (exposure time 1/25 sec.) at a) p=1.3 bar, b) p=2.1 bar. ....	89
<b>Figure 5-4.</b> Optical signals of the O <sub>2</sub> DBD at various pressures normalized at 459.2 nm. ....	90
<b>Figure 5-5.</b> OES intensity of the 358.1 nm Fe line obtained in O <sub>2</sub> DBDs upon increasing pressure.....	91
<b>Figure 5-6.</b> Production rate of nanopowder deposits on the reactor walls in the O <sub>2</sub> DBD, and pictures of the 0.22 μm membrane filters installed downstream the reactor after 2 hours of operation, at the corresponding pressure regimes. ....	92

---

<b>Figure 5-7.</b> Average current pulse in the positive HC of the O <sub>2</sub> DBD (top) and production rate of the collected powder (bottom) as a function of pressure.....	93
<b>Figure 5-8.</b> Measured optical signals (normalized at 337.1 nm) of the CO <sub>2</sub> DBD at various pressures.....	94
<b>Figure 5-9.</b> Average current pulse amplitude of the CO <sub>2</sub> DBD in the positive HC (top) and CO <sub>2</sub> conversion (bottom), as a function of pressure. Discharge power: 650 W; CO <sub>2</sub> flow rate: 0.5 SLM.....	95
<b>Figure 5-10.</b> Images of 0.5 SLM CO <sub>2</sub> DBD (exposure time 1/25 sec.) at a) p=1.3 bar, b) p=2.1 bar.....	96
<b>Figure 5-11.</b> Scheme of the nanoparticle production process in an O <sub>2</sub> /CO <sub>2</sub> DBD, and SEM image showing the cross section of the granular deposit.....	100
<b>Figure 6-1.</b> Various gas input configurations of the MW plasma reactor. ....	107
<b>Figure 6-2.</b> CO <sub>2</sub> conversion and energy efficiency obtained in the MW plasma at 4.75 kW input power and 15 SLM CO <sub>2</sub> flow rate (corresponding to an SEI of 4.8 eV/molec), for the three different gas inlet configurations, upon increasing the pressure.....	110
<b>Figure 6-3.</b> CO <sub>2</sub> conversion and energy efficiency in the MW plasma in the vortex configuration as a function of pressure, at a MW power of 4.75 kW and three different flow rates (15, 22.5 and 30 SLM).....	112
<b>Figure 6-4.</b> CO <sub>2</sub> conversion and energy efficiency in the MW plasma in reverse (a,c) and vortex configurations (b,d), as a function of input power, at 200 mbar and three different gas flow rates.....	114
<b>Figure 6-5.</b> Temperature distribution as a function of distance from the central axis, measured in the vacuum chamber, at a position 20 cm downstream of the MW discharge reactor (see <b>Figure 6-1</b> ), for the direct gas inlet configuration, at a power of 4.75 kW and a flow rate of 15 SLM CO <sub>2</sub> . ....	116
<b>Figure 6-6.</b> Exhaust temperature measurements for the direct, reverse and vortex gas inlet configurations of the MW plasma reactor, as a function of pressure, at a MW power of 4.75 kW and gas flow of 15 SLM CO <sub>2</sub> . ....	117

---

<b>Figure 6-7.</b> Post-discharge temperature measurements for the vortex gas inlet configurations of the MW plasma reactor, as a function of pressure and gas flow rate, at a MW power of 4.75 kW. ....	118
<b>Figure 6-8.</b> CO <sub>2</sub> conversion and energy efficiency in the MW plasma at 4.75 kW – 15 SLM (4.8 eV/molec) for the three different gas inlet configurations, upon increasing pressure. For the vortex configuration, the energy efficiency is also plotted at 30 SLM, while the values for the conversion as the same as at 15 SLM. Besides that, the conversion is presented for 5 SLM vortex gas flow at 200 mbar upon increasing power. In this case the regime is designated as “V5-X@ Y% e.e..” where X is power input in kW and Y is the corresponding energy efficiency. For the other configurations, no results are presented at other flow rates, because no stable plasma could be sustained in this wide pressure range.....	121
<b>Figure 7-1.</b> Comparison of CO <sub>2</sub> conversion and energy efficiency in a MW plasma reactor at 200 mbar and 1 bar (values for both reverse and vortex gas flow configuration) and in DBD at atmospheric pressure.....	132

## List of tables

<b>Table 2-1.</b> Summary of the reactor properties in both the MD and DD configuration .....	20
<b>Table 4-1.</b> CO <sub>2</sub> production in the CO discharge at 400 W and various feed flow rates (0.1-1 SLM) and corresponding specific energy input (SEI) values and gas residence times. ....	61
<b>Table 4-2.</b> Summary of the properties of the COd and CO2d samples obtained in the CO and CO <sub>2</sub> DBD plasmas, respectively, as well as the optical emission characteristics and gas composition in both plasmas, measured with GC, at 600 W input power and 1 SLM gas flow rate, corresponding to a SEI of 9.1 eV/molecule. ....	75
<b>Table 4-3.</b> Difference between the solid materials deposited in our CO DBD and the materials produced in the CO DBD by Geiger and Staack <sup>[148]</sup> .....	77
<b>Table 4-4.</b> Comparison between the production of the CO2d sample in this work and the reported NP production by Gushin <sup>[169]</sup> and Borra et al. <sup>[170]</sup> .....	79
<b>Table 6-1.</b> Summary of CO <sub>2</sub> conversion performance in different MW plasma reactors and for various discharge configurations and conditions. ....	126

# Chapter 1

## Introduction

---

---

*“The carbon dioxide (CO<sub>2</sub>) molecule is a relatively simple molecular system.*

*Nevertheless, much of the life on Earth, as well as the fate of our planet itself, depends heavily on the properties of this small triatomic C1 molecule”, - Michele Aresta*

### 1-1 Introduction

Today carbon dioxide plays a complex role in the modern world. On the one hand, it is an ubiquitous by-product of chemical processing and fuel combustion and thus a major contributor to the so-called *greenhouse effect*. On the other hand, CO<sub>2</sub> has a very good potential to be a negative value raw material for the chemical industry and, possibly, a feedstock for alternative fuels.<sup>[1]</sup> Besides numerous advantages of CO<sub>2</sub> as a feedstock (nontoxic, abundant, and economically attractive), our society has a solid motivation towards the development of carbon dioxide treatment technologies:

- Positive economic incentives for companies to apply capturing and treatment technologies;
- Development of carbon sequestration as a pathway for efficient storage of energy through the conversion of redundant electricity (especially from renewable energy resources);

The implementation of a CO<sub>2</sub> cycle can possibly introduce a system approach solution towards environmental issues and the fuel crisis in general. At the same time, the technological readiness level of carbon dioxide management is still low, while this task is considered as one the greatest engineering challenges of 21<sup>st</sup> century.<sup>[2]</sup> In addition, there are several techno-economical prerequisites that a potential CO<sub>2</sub> recycling process has to satisfy in order to be considered for future up-scaling:

- Switchability;
- A high degree of control and flexibility;
- Scarce materials should be avoided for device construction or catalytic materials;
- Usage of abundant electric power or direct use of solar energy as energy source;
- High efficiency;

Nowadays it is clear that, in order to create a sustainable low-carbon economy, we need to concentrate research focus not only on the reduction of CO<sub>2</sub> emissions into the atmosphere and the sequestration of captured CO<sub>2</sub>, but also on the utilisation of the waste CO<sub>2</sub> as a carbon product or building block. CO<sub>2</sub> conversion technology can be applied in a variety of green chemistry processes for generation of various added-value carbon-based products.<sup>[3]</sup> However in this work we concentrate on the synthesis of CO, while aiming for generation of the so-called solar fuels, as it can a play of the sustainable alternative for the fossil fuels.<sup>[4]</sup>

A lot of novel studies target conversion and decomposition of CO<sub>2</sub> and rely on a large variety of different technologies. There are several excellent reviews that cover the breadth of current developments including benchmarking of different methods and approaches utilized.<sup>[5-7]</sup> The scope of this thesis is, however, limited to the study of plasma-based conversion of CO<sub>2</sub>. This technology can satisfy all requirements listed above and has great potential to become a workhorse in CO<sub>2</sub> utilisation processes.

The following brief review presents the most prominent developments on the topic and highlights routes for improvement of the CO<sub>2</sub> decomposition energy efficiency in various plasma reactors.

## 1-2 Plasma and CO<sub>2</sub>

Interestingly, in the history of plasma chemistry, there were several substantial technological drivers for studying CO<sub>2</sub> plasmas (and accordingly CO<sub>2</sub> decomposition in gas discharges): CO<sub>2</sub> lasers<sup>[8, 9]</sup>, the Mars exploration mission<sup>[10-13]</sup>, gas conversion<sup>[14, 15]</sup> and solar fuels generation<sup>[16, 17]</sup>.

In the case of CO<sub>2</sub> lasers, a beam of infrared light with a wavelength of 9.4 or 10.6 μm is generated in a CO<sub>2</sub>-N<sub>2</sub>-He mixture at pressures up to some hundreds hPa, by populating the low lying vibrational levels of the CO<sub>2</sub> molecule. Both Radio-Frequency (RF) and glow discharges are used nowadays in industrial CO<sub>2</sub> laser systems for

pumping the gas medium.<sup>[9]</sup> Such systems are extensively used in industry for high power density applications (mostly cutting and welding).

The atmosphere of Mars is composed of CO<sub>2</sub> for up to 95.3%<sup>[18]</sup>. Luce described a Dielectric Barrier Discharge (DBD) reactor that was designed to be used onboard of a manned spacecraft to recover O<sub>2</sub> from abundant carbon dioxide on Mars via Reaction 1-1.<sup>[10]</sup> The possibility to realize a low-temperature and low-pressure process was considered as the main advantage of the technology in this context.



Gruenwald proposed a hybrid life support system based on a CO<sub>2</sub> RF or microwave (MW) discharge reactor. The complete dissociation of CO<sub>2</sub> to O<sub>2</sub> and solid carbon C(s) (cf. Reaction 1-2) supposedly allows not only to recover oxygen, but also to co-generate valuable solid carbon (C(s)) products.<sup>[12, 13]</sup>



The interest in the exploration of the red planet is continuously growing, for instance, the *Mars OXygen In-situ resource utilization Experiment* (MOXIE) on CO<sub>2</sub> dissociation using solid oxide electrolysis (SOE) technology will be performed on the next NASA Mars 2020 rover mission.<sup>[19]</sup> Thus, there is a reasonable chance to see a plasma device onboard of a spacecraft in this role as well (although the SOE technology is being tested at the moment for the purposes of the CO<sub>2</sub> decomposition and oxygen separation in this mission).

### 1-3 Plasma-based CO<sub>2</sub> conversion

The success of DBD industrialization for ozone production<sup>[20]</sup> attracted a lot of attention to plasma-based gas conversion technology. Plasma technology utilizes electrical energy and the reactor design is based on abundant constructional materials and can thus perfectly fit into a systematic approach of adopting CO<sub>2</sub> as a carbon

source and generating solar fuels.<sup>[4]</sup> Various plasma systems were tested to activate and decompose highly inert greenhouse gasses (especially  $\text{CO}_2$ <sup>[14, 16]</sup>,  $\text{CH}_4$ <sup>[21, 22]</sup> and chlorofluorocarbons<sup>[23, 24]</sup>). In this thesis, we concentrate on the  $\text{CO}_2$  decomposition reaction in non-thermal plasmas, because the latter have a potential to create a highly-efficient  $\text{CO}_2$  decomposition process by overcoming the thermodynamic barrier of Reaction 1-1 without the need of extensive heating.<sup>[25]</sup>

### 1-3-1 Dielectric Barrier Discharge systems

Dielectric Barrier Discharge (DBD) systems are applied in a variety of industrial applications. By means of this type of electrical discharge it is possible to create strongly non-equilibrium conditions at atmospheric pressure and at high power input levels without the need of sophisticated pulse power supplies. Due to the simple design, DBD reactors have already demonstrated a great potential to operate on a large scale.<sup>[20]</sup> The most common DBD arrangements are presented in **Figure 1-1**. The main feature of DBDs is that at least one of the electrodes is covered with a dielectric layer that limits the discharge current and thus allows to maintain non-equilibrium plasma conditions. In this way rather low-current microdischarges (MD) spread over the barrier layer surface, forming a large-volume discharge.

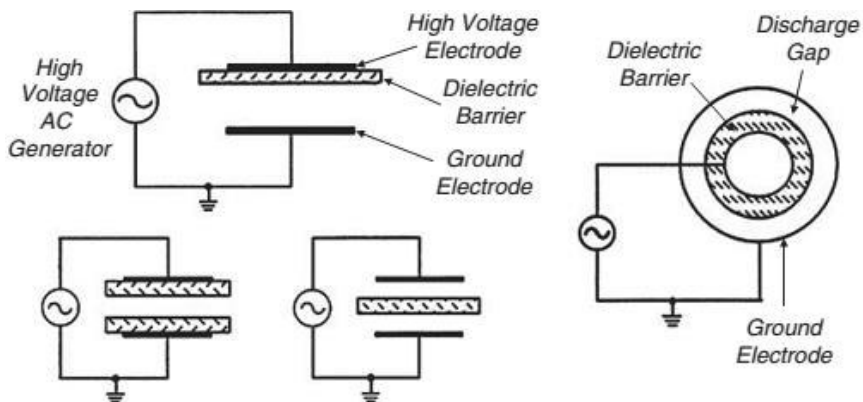


**Figure 1-1.** Common dielectric barrier discharge configurations (taken from <sup>[25]</sup>).

From an engineering point of view, DBDs are ideal for process up-scaling, due to the atmospheric pressure operation, modular design, rather available 1-100 kHz excitation frequency power supplies, low maintenance costs and experience gained with the industrialised ozone production technology. However, when it comes to CO<sub>2</sub> decomposition in a DBD reactor, the low energy efficiency achieved at laboratory scale somewhat limits the potential of these systems. Indeed, typically values between 1-10% are reported for a CO<sub>2</sub> conversion reaching 50-10%.<sup>[26]</sup> Moreover, usually a trade-off between conversion and energy efficiency is observed, i.e. high conversion is achieved at low energy efficiency, and *vice versa*.<sup>[15]</sup> At the same time, it was estimated by Spencer *et al.* that an energy efficiency of at least 52% is required for plasma-based CO<sub>2</sub> processes to eliminate all CO<sub>2</sub> emissions from a natural gas power plant and also be energetically net positive with zero carbon footprint.<sup>[27]</sup> This consideration underlines the need to develop novel pathways to increase the process efficiency. In order to achieve this, one needs to establish control over the properties of the discharge which is composed of numerous microdischarges (also called filaments), each of them acting as a chemical reactor.<sup>[28]</sup> Due to the temporally and spatially transient discharge operation, this can be done only indirectly, i.e. unfortunately, the discharge parameters inside microdischarges cannot be set externally.<sup>[29]</sup>

DBD systems can essentially be considered (and electrically modelled) as a capacitor<sup>[30]</sup>, and one of the ways to improve the CO<sub>2</sub> conversion efficiency in a DBD is to increase the effective capacitance of the reactor to obtain a higher discharge current. This can be done by utilizing high-permittivity dielectrics<sup>[31-35]</sup>, introducing packing materials<sup>[36-40]</sup> or decreasing the discharge gap<sup>[41]</sup>.

In a series of papers by Li *et al.*, the implementation of high-permittivity dielectric materials enabled a higher power discharge and consequently a higher CO<sub>2</sub> conversion.<sup>[31-34]</sup> It was also demonstrated that utilisation of Ca<sub>0.8</sub>Sr<sub>0.2</sub>TiO<sub>3</sub> (permittivity  $\epsilon$  of 208) as a barrier material allowed to achieve a discharge power of 68W and a CO<sub>2</sub> conversion of 18% with an energy efficiency of 0.5%. At the same time, an identical DBD system with the conventional Al<sub>2</sub>O<sub>3</sub> (permittivity  $\epsilon$  of 10.3) as the dielectric

material, yielded only 4W discharge power for the same applied voltage of  $\sim 3$  kV, and 4% conversion at an energy efficiency of 2%. It was assumed that the introduction of the higher permittivity dielectric allowed higher current microdischarges to be formed, also raising the discharge power. Besides that, formation of carbon deposits was reported and attributed to the observed high-current pulses when  $\text{Ca}_{0.8}\text{Sr}_{0.2}\text{TiO}_3$  barrier material was used. The major advantage of this approach is the opportunity to realise a high-power regime that yields rather high  $\text{CO}_2$  conversion. However, it can be seen that the energy efficiency of the DBD with the high-permittivity barrier layer is very low. It can be attributed to the fact that the electrical properties of this dielectric material were not stable with increasing temperature, which can be expected during a high-power DBD operation without cooling.

It was demonstrated by Mei *et al.* that introduction of a packing material (glass or  $\text{BaTiO}_3$  beads with 1 mm diameter) in a 3 mm gap DBD reactor allowed an effective substantial increase of the capacitance of the system.<sup>[36]</sup> Values of 54.4 pF, 70.2 pF and 91.5 pF (at 50W discharge power) were reported for the simple (i.e. non-packed) DBD and glass- and  $\text{BaTiO}_3$ - packed systems, respectively. Interestingly, the DBD reactor packed with  $\text{BaTiO}_3$  resulted in a significantly higher conversion than the glass-packed system and the DBD without packing (28%, 22% and 16% with energy efficiencies of 6%, 4.5% and 3% respectively) at the same power input of 50W. This was explained by the increased electric field due to the high surface area of the packing material (when compared to the surface area of a non-packed DBD), but also by the photocatalytic reaction of  $\text{BaTiO}_3$ , presumably activated<sup>[42]</sup> by plasma exposure.

It is important to notice that a packed reactor is usually compared with a non-packed DBD of rather large gap (usually around 3-6 mm in order to be able to incorporate the beads). However, it was demonstrated by Aerts *et al.* that a decrease of the discharge gap is beneficial for the  $\text{CO}_2$  DBD efficiency due to an increase of the effective capacitance of the system.<sup>[41]</sup> Also higher discharge current pulses were accompanied with a higher  $\text{CO}_2$  conversion when a smaller discharge gap of 1.8 mm or 2.3 mm was applied instead of a 3.3 mm gap. In this way at 40W power input,  $\sim 30\%$

conversion was achieved for both a 1.8 mm and 2.3 mm gap DBD, while only 20% was measured when the gap was 3.3 mm.

This idea was developed even further into the field of micro-plasma devices of sub-mm dimensions.<sup>[43-45]</sup> A micro-plasma Surface-DBD (SDBD) was utilised for the CO<sub>2</sub> decomposition in a number of works.<sup>[46, 47]</sup> The reactor, composed of 24 discharge channels with 200 µm width yielded a conversion of 2-10% at 9-12% energy efficiency. Besides the advantage of the small discharge dimensions (and thus higher power and electron density), the given set-up utilises the high surface area of nanoporous alumina, used as a dielectric material in this case, that can significantly steer the plasma-surface interactions. Nevertheless, the rather low maximum energy efficiencies achieved in various DBD systems might suggest that CO<sub>2</sub> conversion is inherently limited in this type of plasma. A closer look on the fundamental aspects of a DBD operation is needed to explain this effect.

### 1-3-2 Why is the CO<sub>2</sub> conversion in a DBD inherently limited?

The efficiency of a non-equilibrium plasmachemical process is largely determined by reaction kinetics, i.e. the channels to which the energy flows. However, these directions are mostly defined by the parameters of the gas discharge. The reduced electric field strength  $E/n$  ( $E$  is the electrical field strength and  $n$  is the density of neutral particles) is one of the major discharge parameters. This value determines the mean energy of the electrons in the plasma and accordingly, the ongoing chemical reactions. **Figure 1-2** demonstrates how the electron energy is transferred to different channels of excitation, ionisation and dissociation of CO<sub>2</sub> in a discharge at atmospheric pressure, as calculated by Aerts *et al.*<sup>[48]</sup> In spatially and temporarily transient DBD plasmas, the  $E/n$  is largely determined by the development of microdischarges and is typically above 200 Td.

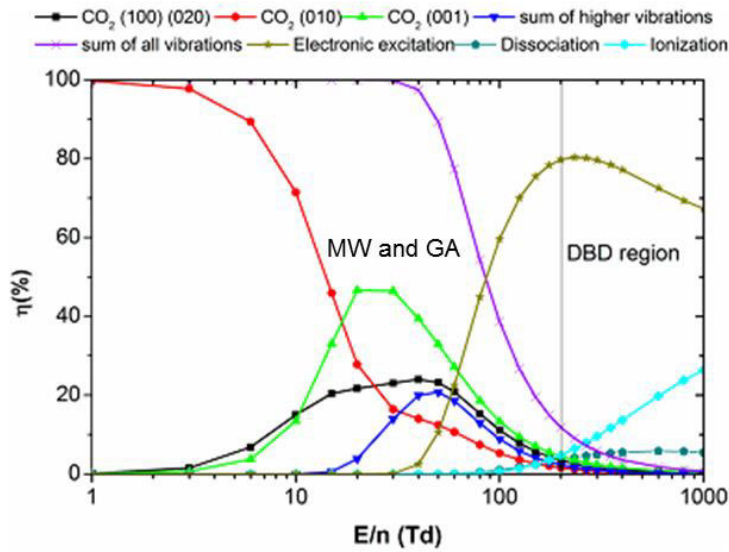
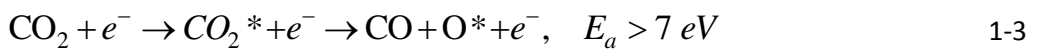


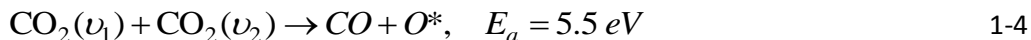
**Figure 1-2.** Fractional electron energy transferred to different channels of excitation, ionization and dissociation of  $\text{CO}_2$ , as a function of the reduced electric field ( $E/n$ ) (taken from <sup>[48]</sup>).

According to Aerts *et al.*, electron impact electronic excitation followed by dissociation (cf. Reaction 1-3) is dominant for a DBD plasma and thus the major reaction in the  $\text{CO}_2$  decomposition process.<sup>[48]</sup> This process requires an activation energy of more than 7 eV, while the dissociation energy of  $\text{CO}_2$  is only 5.5 eV. This mismatch between transmitted energy and the dissociation requirement results in heat dissipation and leads to the low energy efficiency of this channel<sup>[25]</sup> and thus illustrates the fundamental limitation of  $\text{CO}_2$  decomposition in a DBD.



Fridman and co-workers proposed a pathway to utilise precisely 5.5 eV for a single  $\text{CO}_2$  molecule dissociation.<sup>[25]</sup> It was stated that for gas discharges with an electron temperature around 1–2 eV (or a reduced electric field ( $E/n$ ) of about 20–40 Td), up to 97% of the total non-thermal discharge energy can be transferred from plasma electrons to vibrational excitation of  $\text{CO}_2$ . This process might be followed by a

more effective dissociation reaction stimulated by step-by-step vibrational excitation (cf. Reaction 1-4) and would require only 5.5 eV activation energy.



It can be seen that control over  $E/n$  would allow optimisation of the plasmachemical  $\text{CO}_2$  conversion. In case of a DBD, as already mentioned, the plasma is composed of numerous filaments, which are known to define the plasma chemistry.<sup>[28]</sup> The number of these filaments and their properties can, however, not be controlled externally, for instance by the applied voltage.<sup>[29]</sup> In the same way, parameters such as reduced electric field  $E/n$  or electron density  $n_e$  are not available for direct tuning. In this thesis (cf. **Chapter 4** and **5**), however, it will be demonstrated how we can have some degree of control over the properties of microdischarges.

It is known that other types of non-thermal plasmas (such as microwave or gliding arc discharges, which will be presented below) operate at somewhat lower  $E/n$  and thus maintain more favorable kinetics for  $\text{CO}_2$  dissociation. Moreover, in some instances it is possible to regulate the reduced electric field. The next section will demonstrate the experimental findings on this topic.

### 1-3-3 Control over $E/n$

As stated above, theoretically,  $E/n$  values of about 20-40 Td should induce the most favourable conditions for the  $\text{CO}_2$  decomposition reaction. This concept was proven experimentally in the work by Andreev *et al.*, where the  $\text{CO}_2$  decomposition in a non-self-sustained discharge with tuneable  $E/n$  was demonstrated.<sup>[49]</sup> The energy cost of the  $\text{CO}_2$  molecule splitting was minimal (10 eV/molec.) when the  $E/n$  was about 20 Td. In the same study,  $\text{CO}_2$  dissociation in a non-self-sustained ( $E/n$  set to 20 Td) and a self-sustained glow discharge ( $E/n \sim 100$  Td) was also compared at the same pressure and power input. The performance of the former was superior, as the minimal energy cost of the  $\text{CO}_2$  splitting in a self-sustained plasma was as high as 110 eV/molec. This paper

highlights the need to decrease and control  $E/n$  in a plasmachemical process. However, the up-scaling of reactor based on a non-self-sustained discharge with controllable  $E/n$  would be complicated due to the limited process window of such a system.<sup>[50]</sup> Another option to utilise the non-equilibrium character of a plasma with somewhat lower  $E/n$  are *warm* plasmas, including Microwave (MW) discharges or Gliding Arc (GA) systems, which are introduced in the next sections. Interestingly, the concept of  $E/n$  control was recently also demonstrated for  $\text{CO}_2$  decomposition in MW plasma systems, where waveguide dimensions can be used to tune the electric field.<sup>[17, 51]</sup> As expected, higher electric field values (which are often used for discharge ignition) were found to result in a decrease of  $\text{CO}_2$  decomposition energy efficiency. This in turn proves that the  $E/n$  should be considered as one of the main parameters defining the energy efficiency of  $\text{CO}_2$  decomposition in a plasma process.

### 1-3-4 Microwave (MW) discharge reactors

MW discharge systems are very versatile and can be sustained at various pressure and gas flow regimes. In case of MW, the applied excitation frequencies are in the range of 300 MHz to 10 GHz. **Figure 1-3** demonstrates a widespread design of a rectangular waveguide MW plasma system, while the description of the various alternative MW arrangements, such as microwave cavity discharges or surface wave sustained discharges, can be found elsewhere.<sup>[52]</sup>

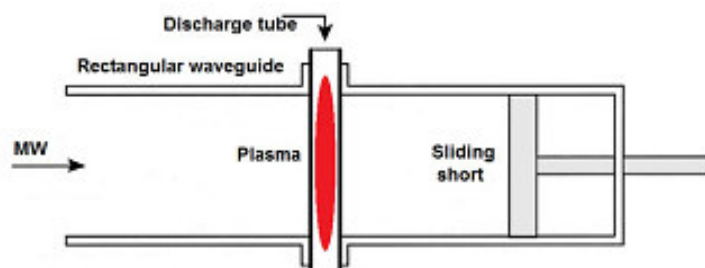


**Figure 1-3.** Schematic representation of a MW configuration (taken from <sup>[52]</sup>).

It was demonstrated by modeling that the lower electron temperature of a MW plasma allows utilization of more efficient channels of CO<sub>2</sub> decomposition, i.e., by vibrational kinetics as explained above, compared to a DBD.<sup>[53]</sup> From a technological point of view, MW plasma reactors represent an electrodeless solution with a high electric energy utilization efficiency and a fast switching on time.<sup>[54]</sup> The Soviet developments of MW discharge systems resulted in the most successful experiments on CO<sub>2</sub> decomposition in the 1980s.<sup>[25, 55]</sup> Energy efficiencies up to 90% at a CO<sub>2</sub> conversion of 10% were achieved when a supersonic flow regime was utilized at reduced pressure of about 200 mbar. The topic was brought up again recently in response to the spread of intermittent renewable electricity sources and the general acceptance of the need to fight global warming. Attempts to reproduce the conditions and results reported in the work of Fridman et al. have been made recently, but efficiencies of only up to 51% were demonstrated so far in this case.<sup>[17]</sup> Recently, a lot of novel approaches to improve the overall efficiency of the technology were studied: post-discharge catalytic<sup>[56-59]</sup> or oxidation<sup>[60, 61]</sup> treatment, utilization of Ar<sup>[62, 63]</sup>, N<sub>2</sub><sup>[64]</sup>, H<sub>2</sub><sup>[51, 65]</sup> and H<sub>2</sub>O<sup>[56, 58, 59, 61]</sup> gas admixtures. Despite all the recent attention to the technology, it is still unclear which process (i.e. pressure, gas flow regime) conditions are the most suitable for scale-up. Generally, operation at atmospheric pressure is preferred due to the lower operational costs<sup>[66, 67]</sup>; however, the highest energy efficiencies (~90%) for CO<sub>2</sub> MW plasma systems were reported for the reduced pressure regimes (~150 mbar).<sup>[25]</sup> It is known that thermalisation is occurring with increasing pressure, raising the gas temperature and decreasing the energy efficiency of the process.<sup>[66]</sup> In this way, the low-pressure MW plasma is usually referred to as non-equilibrium and “warm” plasma, while the MW discharge at atmospheric plasma is considered as “thermal”, characterized with lower energy efficiency.

### 1-3-5 Gliding arc plasma systems

In contrast to MW plasmas, gliding arc (GA) discharges allow to utilise the properties of non-equilibrium, warm plasma at atmospheric pressure.<sup>[68]</sup> A GA plasma indeed possesses features of both thermal and non-thermal plasmas. A GA discharge is a non-stationary arc discharge between two diverging electrodes in a gas flow (cf. **Figure 1-4**). The arc is ignited at the shortest electrode distance ("i" on **Figure 1-4**) and pushed by the gas flow towards the diverging electrode region. Convective cooling of the gas flow allows a GA plasma to preserve non-equilibrium properties even at discharge currents of up to 1 A.<sup>[68]</sup>

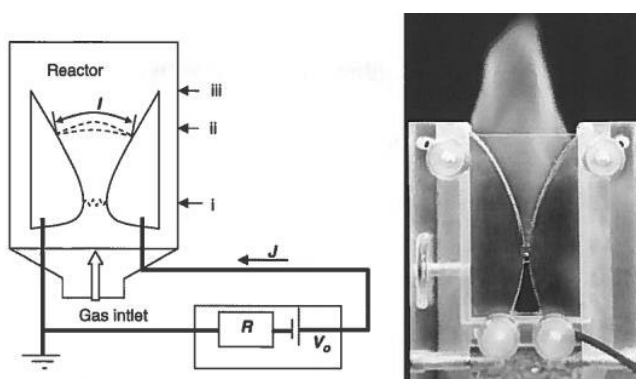


**Figure 1-4.** Conventional gliding arc, schematic image (left, where i-ignition point, ii-point of developed gliding arc, iii-extinction zone) and picture of the flat GA discharge (taken from <sup>[68]</sup>).

In this way, the electron temperature most favourable for  $\text{CO}_2$  decomposition, about 1 eV, can be obtained at atmospheric pressure and at non-equilibrium conditions. Only a limited amount of papers on  $\text{CO}_2$  decomposition in GA discharge systems is available. In the work of Nunnally *et al.* an energy efficiency of up to 43% with a conversion rate of around 5% at SEI of 0.3 eV/molec. was achieved in a GA reactor operating in a reverse vortex flow regime.<sup>[69]</sup> Kim *et al.* demonstrated  $\text{CO}_2$  conversion in a 3-phase GA plasmatron with 12.3% maximum conversion and 52.3% energy efficiency, that can be further improved with the introduction of a  $\text{CH}_4$  admixture.<sup>[70]</sup> Ramakers *et al.* recently

presented a GA plasma system that can operate in low (~50 mA) and high (260-380 mA) current regimes.<sup>[71]</sup> The highest energy efficiency in this case was measured for the low-current discharge (46% at a conversion of around 2%), while the high-current GA yielded the highest conversion (8.6% with an efficiency of 30%). GA set-ups show numerous advantages of warm plasmas and high energy efficiency of CO<sub>2</sub> decomposition at atmospheric pressure, but the scale-up of the gliding arc plasma reactor might be more difficult, the high plasma injection power injection would require higher flow rates (and thus shorter residence times) that would accordingly lead to increased volumes of by-passed and thus unreacted gas volumes.<sup>[72]</sup> On the contrary to that, miniaturisation of GA systems might also be considered as the way forward for the technology<sup>[73]</sup>, although this will reduce the throughput, and thus limit the upscaling possibilities.

## 1-4 Aim and Outline of the PhD Dissertation

Even when taking into account the overall progress and multiple innovative steps that were introduced recently, the energy efficiency of the plasma based CO<sub>2</sub> conversion still hinders further upscaling. Moreover, there is a clear mismatch between the most efficient technology (MW at low pressure) and the most scalable process (DBD at atmospheric pressure). It is also obvious that the tuning of the discharge systems is not trivial, because we cannot control the plasma parameters externally. In order to address these issues, the aim of this dissertation is to explore the CO<sub>2</sub> dissociation reaction in two types of plasma reactors, a DBD and a MW system, and to identify new ways to control and improve the process. In **Chapter 2** the experimental set-ups, diagnostics and gas and surface analysis are presented. **Chapter 3** describes how the surface resistivity of the electrodes in a DBD can significantly steer the microdischarge behaviour in electronegative gases (such as CO<sub>2</sub> and O<sub>2</sub>), and thus also the CO<sub>2</sub> dissociation processes. As the CO<sub>2</sub> conversion can reach quite high values in our DBD reactor it is interesting to note that the molar concentration of CO (product of CO<sub>2</sub> splitting) is reaching considerable values and thus can potentially induce deposition of solid carbon. In **Chapter 4** the possibility of nanomaterial co-generation in CO<sub>2</sub> and CO DBDs is discussed and a comparison between discharges in CO<sub>2</sub> and CO is made. From the literature it is known that a pressure increase over atmospheric conditions in a DBD can be beneficial for some plasmachemical processes. It is interesting to explore the influence of pressure rise for stimulating the CO<sub>2</sub> dissociation reaction in a DBD and thus in **Chapter 5** the effect of over-pressuring the reactor is studied and identified as an additional tool for controlling and improving the performance of CO<sub>2</sub> DBD systems. Furthermore, an O<sub>2</sub> DBD is also studied in this chapter to better illustrate the effect of metal electrode evaporation in oxygen-containing DBDs. In addition to DBDs, MW discharges are also considered as one of the most promising plasma systems for CO<sub>2</sub> decomposition. **Chapter 6** discusses the operation of a CO<sub>2</sub> MW discharge in a wide pressure range (200 mbar -1 bar), and the CO<sub>2</sub> conversion is evaluated for various gas

flow configurations. Finally, **Chapter 7** concludes the thesis and presents an outlook on the research directions that need to be further investigated in order to come to an efficient CO<sub>2</sub> dissociation process.

## Chapter 2

# Experimental

---

## 2-1 DBD reactor set-up

In order to explore the CO<sub>2</sub> dissociation reaction in the DBD reactor upon high energy input, a special system design is utilized. A cooling circuit is introduced to prevent the overheating of the glass tube and the formation of parasitic discharges on the sharp edges of the mesh electrode. In this way it is possible to operate at high power regimes and accurately measure the voltage and current waveforms. The description of the reactor design and its auxiliary systems are presented in the next sections.

### 2-1-1 Reactor set-up

The experimental setup is schematically shown in **Figure 2-1**. A discharge gap of 0.5 mm is obtained between two concentric cylinders, i.e., a grounded stainless steel central electrode (outer diameter 25 mm) and a dielectric tube (26 mm inner diameter, 29 mm outer diameter) made of borosilicate glass. It is demonstrated by Aerts et al. that using a smaller gap allows the rise of the reactor capacitance and a decrease of the onset voltage due to enhanced electric field intensity, which is beneficial for the system performance.<sup>[41]</sup> A stainless steel mesh is wrapped at the outside of the dielectric tube, acting as an outer electrode and at the same time defining the length of the plasma discharge (215 mm). The outer electrode arrangement is cooled with deionized water with a controlled conductivity of less than 0.5 μS·m. The central electrode is cooled with drinking water of standard quality.

The inner electrode is grounded while the outer electrode is connected to a power supply with a maximum peak-to-peak voltage of 40 kV and a variable frequency between 2 and 90 kHz (AFS G10S-V generator, AFS GT-10...80 transformers). The applied voltage and the total current are measured by a high voltage probe (Tektronics P6015A) and a Rogowski-type current meter (Pearson Model 4100, 35 MHz), respectively. It is important to mention that the bandwidth of the Rogowski coil limits the time resolution of the current measurements at ~29 ns. A discharge event faster

than this limit, would be smoothed out (for instance maximum peak intensity will be lower) or completely absent.

### 2-1-2 MD and DD configuration of the DBD

In **Chapter 3** the so-called Metal-Dielectric (MD) and Double Dielectric (DD) configurations of the DBD reactor is utilised in order to draw conclusions regarding the influence of the surface properties of the electrode material on the discharge properties. The DD DBD (**Figure 2-1, b**) is similar to the MD reactor with respect to the arrangement of the electrodes. The central electrode is in this case a borosilicate tube, filled with technical quality water, i.e. conductive water. A grounded stainless steel rod is introduced into the liquid for sustaining electrical contact. Water is circulated for cooling of the barrier tube. Due to the design of the MD reactor, it is not possible to introduce an external measuring capacitor in the electrical circuit of the reactor. The stainless steel grounded basement was used to bear the whole construction due to the rather high dimensions of the discharge zone (cf. **Table 2-1**) and the presence of the cooling system. The water-cooled metal electrode was designed in such a way that it was always electrically connected to the basement and thus to the ground. In this way it was not feasible to galvanically disconnect electrode from the ground (to install the capacitor in series) without compromising the robustness of the set-up. This diagnostic tool is implemented only in the DD configuration of the reactor, where a 5.5 nF capacitance is installed in series with the grounded electrode to obtain the transferred charge – voltage (Q-U) characteristics. The same electrical analysis and gas chromatography systems (described in the next sections) are applied for the experiments in the MD and DD reactors. **Table 2-1**, presented below, summarizes the properties of the MD and DD reactor configurations.

**Table 2-1.** Summary of the reactor properties in both the MD and DD configuration

Property	Reactor type	
	MD configuration	DD configuration
Gap, mm	0.5	0.5
Length of discharge zone, mm	215	215
Outer dielectric	Alumina or borosilicate glass	Alumina or borosilicate glass
Inner dielectric	-	Borosilicate glass
Discharge cell capacitance, pF	330 or 250 (for alumina or glass dielectric, resp.)	175 or 150 (for alumina or glass dielectric, resp.)
External capacitance, pF	-	5500

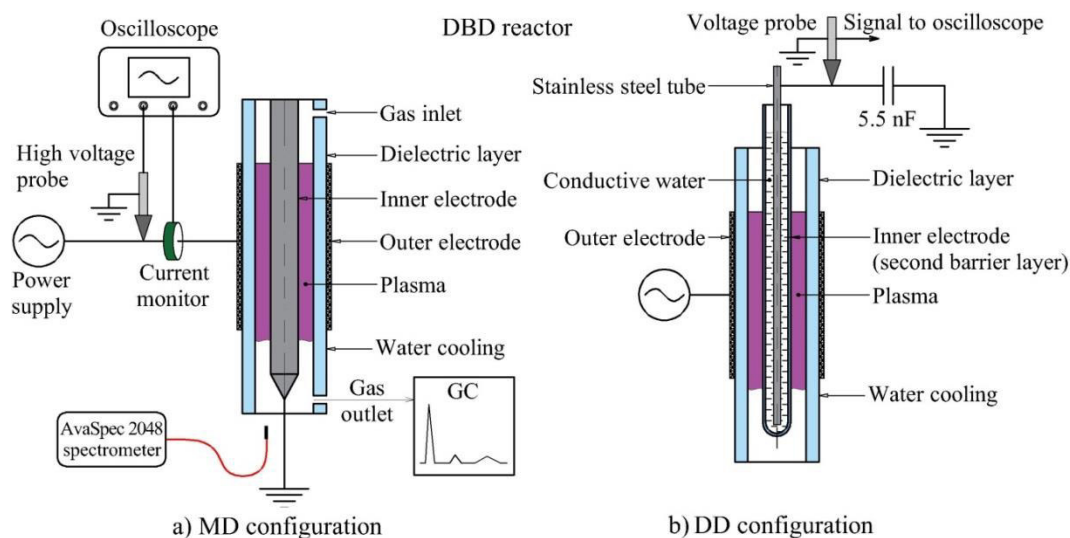


**Figure 2-1.** Dielectric barrier discharge reactor in the a) Metal-Dielectric (MD) and b) Double Dielectric (DD) configuration.

### 2-1-3 Overpressured DBD set-up

It is known that a 0.5-1 bar pressure increase (over atmospheric conditions) in a DBD reactor can be beneficial for some plasmachemical processes, for instance ozone generation.<sup>[74]</sup> It is interesting to utilise this idea for stimulating CO<sub>2</sub> dissociation in a DBD by increasing the pressure. Hence in **Chapter 5** the CO<sub>2</sub> DBD operation is presented when using overpressure. Besides that, the influence of the pressure on an O<sub>2</sub> DBD and nanomaterial production in this discharge is demonstrated to better illustrate the effect of metal electrode evaporation in oxygen containing DBDs (also discussed in **Chapter 4**). The arrangement presented in **Figure 2-2** is utilized and allows to set the pressure within the range of 1-3.5 bar via a pressure gauge and a control valve.

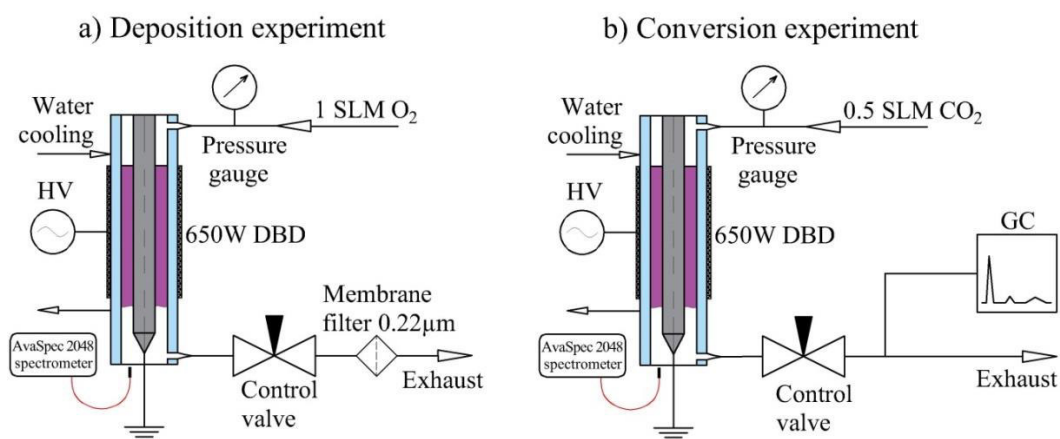


**Figure 2-2.** Experimental setup of the tubular Dielectric Barrier Discharge reactor used for a) nanomaterial production in O<sub>2</sub> DBD and b) gas conversion in CO<sub>2</sub> DBD, when using overpressure.

The overpressured O<sub>2</sub> and CO<sub>2</sub> DBD gives rise to strong erosion of the metal electrode surface and redeposition of the etched material in the form of a granular metal oxide nanoparticle film on the reactor walls. In this study the material is collected from the inner surface of the dielectric tube (where it is mostly deposited) in the form of a nanopowder and weighted. The production rate is evaluated via dividing

this value by the reaction time (120 minutes). A membrane filter (Millipore GPWP 02500; diameter, 25 mm; pore size, 0.22  $\mu\text{m}$ ) is installed in-line with the reactor to qualitatively demonstrate the presence of the produced nanoparticles downstream of the discharge.

### 2-2 MW discharge system

The study of  $\text{CO}_2$  MW discharge with various gas flow regimes in a wide pressure range (200 mbar – 1 bar) is targeted in **Chapter 6**. That requires a very versatile MW plasma reactor, as in many cases it is not possible to realise some operational regimes without vortex gas flow.<sup>[54]</sup> The set-up described in the next sections provides the opportunity to stably sustain MW plasma with various gas flow configurations in the whole desired pressure range.

#### 2-2-1 Reactor design

The  $\text{CO}_2$  decomposition experiments are performed in a system composed of the commercial IPLAS *CYRANNUS* plasma source mounted on top of the stainless steel vacuum chamber (**Figure 2-3**). The principle of the given microwave plasma source is based on a resonator with annular slot antennas.<sup>[75]</sup> This special set-up allows to sustain a MW discharge in a very wide pressure range, from low ( $10^{-2}$  mbar) to atmospheric pressure (1 bar).

#### 2-2-1 Microwave system

The 2.45 GHz magnetron supply with a maximum output of 6 kW microwave field is connected through a circulator and an E-H tuner to the resonator cavity. The plasma is formed in a cylindrical quartz tube with a diameter of 140 mm and a height of 140 mm that corresponds to a volume of 2.1 liters. The discharge tube is connected via the DN350 flange to the chamber that has a height of 235 mm and overall volume of 22 liters. The reflected power is measured via a microwave

detector installed in the circulator and minimized by an E-H tuner, which is used as an impedance matching device. The circulator, magnetron and the plasma-exposed parts of the discharge cell are all water-cooled, while the resonator and the outer surface of the quartz tube are air-cooled.

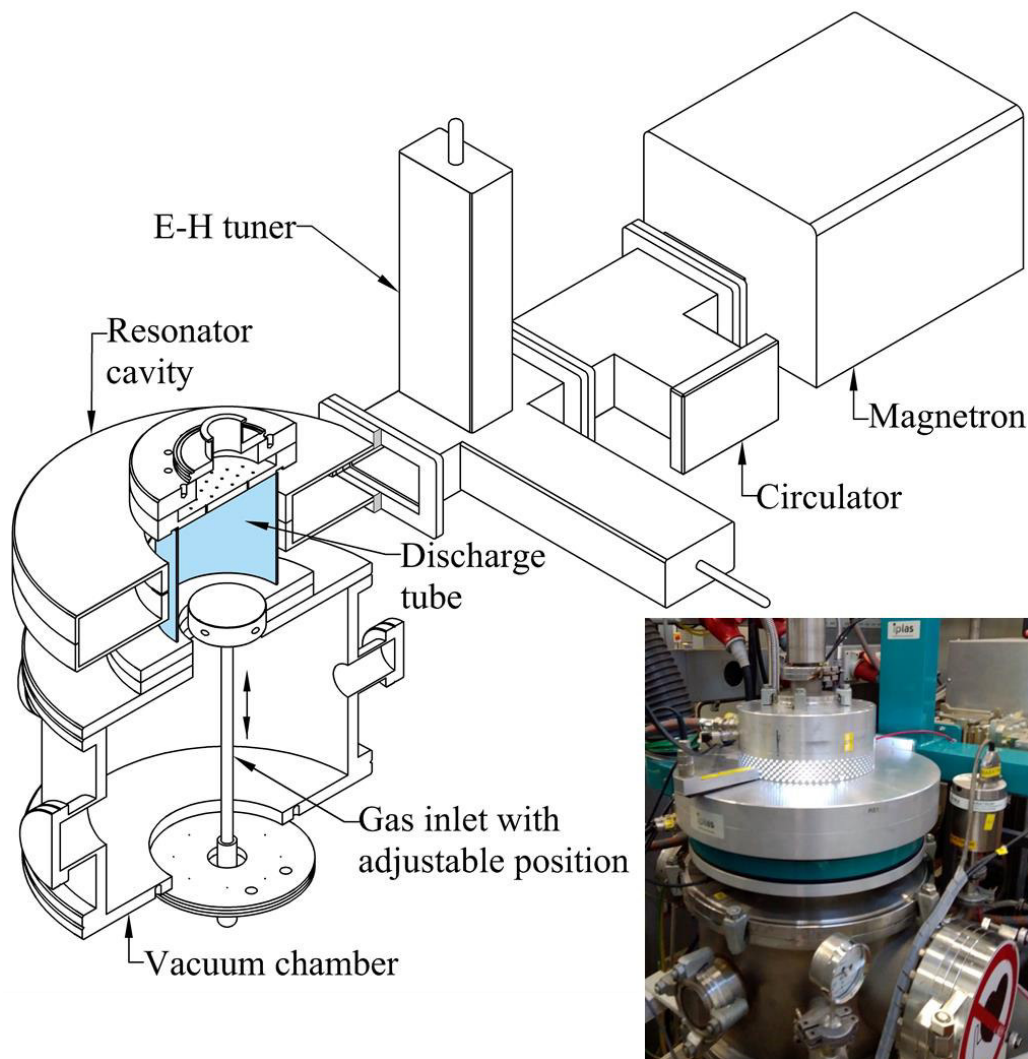


**Figure 2-3.** Drawing and photo of the MW discharge system.

### 2-2-2 Gas supply and vacuum scheme

The gas supply and vacuum systems are demonstrated in **Figure 2-4**. Prior to operation the vacuum chamber is pumped down to 20 mbar via the rotary and Roots pump installed in series. The pressure is set via the controlled valve and the pressure gauge, while CO<sub>2</sub> flow is supplied through the Mass Flow Controller (MFC). With 2-6 kW MW power input the discharge can be ignited without an additional inert gas admixture or electric field concentrator at a maximum pressure of about 100 mbar when 5-30 SLM CO<sub>2</sub> is supplied to the system. After the breakdown, the pressure in the chamber can be further increased up to 1 bar, while the plasma remains to be sustained.

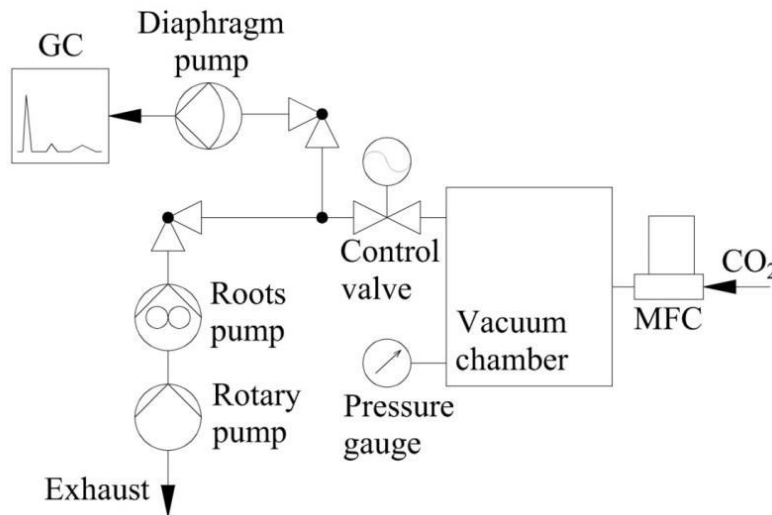


**Figure 2-4.** Gas supply and vacuum scheme of the set-up.

## 2-3 Process control, diagnostics and analytical techniques

### 2-3-1 Power measurement

The process is monitored by a 25 MHz PicoScope 2205 digital oscilloscope, while the electrical signals are recorded by a 2.5 GS/s 500MHz Tektronics TDS 3052 (S/s =

number of samples per second). In our system, the energy input in the discharge is controlled by setting the power of the generator and calculating the corresponding value (Equation 2-1):

$$P_{Input} = \frac{1}{T} \int_0^T I(t)U(t)dt \quad 2-1$$

where  $T$  is the period of the AC, and  $I(t)$  and  $U(t)$  are the measured current and applied voltage signals, respectively. Previous calorimetric studies of the system confirmed the accuracy of this method.

### 2-3-2 Gas chromatography (GC) analysis

The gaseous products of the reaction are analysed by gas chromatography (Trace-GC, Interscience), equipped with a thermal conductivity detector (TCD).  $CO_2$  dissociation is taking place in the plasma according to (Equation 2-2):



To evaluate the  $CO_2$  conversion and corresponding energy efficiency in the MW discharge, the gas mixture is sampled from the exhaust pipe to the gas chromatograph (GC) through a diaphragm pump. The formulas below are used to calculate the  $CO_2$  conversion (Equation 2-3), specific energy input (SEI, Equation 2-4) and energy efficiency of the process<sup>[76]</sup> (Equation 2-5):

$$CO_2 \text{ Conversion (\%)} = \left[ 1 - \frac{\text{moles } CO_{2, Plasma \text{ ON}}}{\text{moles } CO_{2, Plasma \text{ OFF}}} \right] \times 100\% \quad 2-3$$

$$SEI \text{ (eV/molec.)} = \frac{P_{Input} \text{ (W)} \cdot 6.24 \times 10^{18} \text{ (eV / J)} \cdot 24.5 \text{ (L / mol)} \cdot 60 \text{ (sec / min)}}{\text{Flow rate (mL / min)} \cdot 6.022 \times 10^{23} \text{ (molecule / mol)}} \quad 2-4$$

$$\text{Energy efficiency (\%)} = CO_2 \text{ Conversion (\%)} \cdot \frac{\Delta H \text{ (eV/molec.)}}{SEI \text{ (eV/molec.)}} \quad 2-5$$

The systematic error of the GC measurements was evaluated to be around 5%, which is indicated on the graphs as error bars.

### 2-3-3 Optical emission spectroscopy (OES)

A UV/VIS (180-750 nm) survey fiber spectrometer (Avantes, AvaSpec 2048) with 2.3 nm FWHM resolution is used for monitoring the process in DBD reactors, collecting light through a 6 mm collimating lens. The lens is pointed on the gas gap through the optical window (90% transmittance in the 320-600 nm range) installed downstream the reactor parallel to the electrode axis.

### 2-3-4 Material preparation and characterisation

In **Chapter 4** the solid material deposited on the reactor walls is collected from the inner surface of the dielectric tube in the form of a powder.

A field emission gun **Scanning Electron Microscope (SEM)**, FEGSEM, JSM-6340F, JEOL) is used to obtain images to evaluate the microscopic structure and to determine the elemental composition of the formed structures.

**Fourier Transform Infrared spectroscopy (FTIR)** is performed with a Thermo Nicolet Nexus spectrometer in Attenuated Total Reflectance (ATR) mode. Typically 0.015 g of powder is spread over the diamond crystal and pressed to improve the contact between the crystal and the sample. The spectrum is recorded between 4000 and 400  $\text{cm}^{-1}$  over 128 scans in order to achieve an acceptable signal to noise ratio.

**X-Ray Diffraction (XRD)** patterns are recorded using PHILIPS X'PERT PRO with  $\text{Cu K}\alpha$  radiation in a  $2\theta$  range between  $0^\circ$  and  $120^\circ$  ( $0.04^\circ$  scan step size) at room temperature.

**Raman Spectroscopy** measurements are employed to identify the chemical bonding characteristics of carbon with a Renishaw Raman Microscope with a 1800 lines/mm grating and using a laser line of 512 nm as the excitation source.

Finally, an **X-ray Photoelectron Spectroscopy (XPS)** system PHI-5600ci (Physical Electronic) is used to perform quantitative elemental analysis at the surface of the

solid materials by spectroscopy of the emitted photo electrons. The powder is applied on indium foil and measured from the area with a diameter of 800  $\mu\text{m}$ .

## Chapter 3

# Influence of the electrode surface on the CO<sub>2</sub> conversion in a DBD

---

This chapter examines the properties of a dielectric barrier discharge (DBD) reactor, built for CO<sub>2</sub> decomposition, by means of electrical characterization, optical emission spectroscopy and gas chromatography. It will be shown that besides conversion into CO and O<sub>2</sub>, the CO<sub>2</sub> DBD also results in the deposition of a coating on the reactor walls. Interestingly, the presence of this film on the dielectric surface induces the modification of the electrical properties of the CO<sub>2</sub> DBD. Moreover, the deposition of this coating on the walls of the double-dielectric (DD) DBD configuration can also stimulate CO<sub>2</sub> conversion. These effects can be correlated with the small conductivity of the coating.

---

This chapter has been published as: I. Belov, S. Paulussen, A. Bogaerts, Appearance of a conductive carbonaceous coating in a CO<sub>2</sub> Dielectric Barrier Discharge and its influence on the electrical properties and the conversion efficiency, *Plasma Sources Sci. Technol.* 2016 **25** 015023.

### 3-1 Introduction

It is known that the properties and dynamics of microdischarge formation in a DBD are strongly related to the electrode arrangement of a discharge cell.<sup>[29]</sup> In this chapter the CO<sub>2</sub> conversion will be explored in various configurations of a DBD reactor (cf. **Figure 2-1**) to identify the influence of the electrode lay-out on the behaviour of microdischarges in a CO<sub>2</sub> DBD and thus on the CO<sub>2</sub> conversion. First, we investigate the asymmetric current waveforms observed for a CO<sub>2</sub> discharge, composed of high-amplitude sparse peaks in the positive half-cycle (HC) and limited discharge current in the negative one. An asymmetry of the current waveform of the CO<sub>2</sub> discharge is indeed also observed in literature for a system with a metal electrode and an electrode covered with a dielectric material (further denoted as metal-dielectric or MD configuration)<sup>[15, 33]</sup> and suggests the dissimilarity of microdischarge activity in the positive and negative HC. This phenomenon can be expected, given the asymmetric nature of a coaxial DBD reactor in a MD configuration<sup>[77, 78]</sup> and the principles of microdischarge formation.<sup>[79-81]</sup> Nevertheless, the asymmetric properties of the discharge activity are mostly reported for surface barrier discharge set-ups<sup>[82-86]</sup>, while asymmetric current waveforms consisting of uniform glow-like and strong filamentary phases are typically observed for these systems.<sup>[87-89]</sup> Depending on the polarity of the applied voltage, the half-cycles are denoted as M+D- when the metal electrode is positive and M-D+ in the other case. Folkstein *et al.* studied the asymmetry of the microdischarge properties in N<sub>2</sub>-O<sub>2</sub> mixtures and found that M-D+ microdischarges are less intense, but more frequent than M+D- ones.<sup>[90]</sup> Hoder *et al.* observed differences in the microdischarge development and propagation in various single filament DBD reactor configurations by means of cross-correlation spectroscopy<sup>[81]</sup>. Osawa and Yoshika demonstrated an asymmetrical current waveform using a 50 Hz DBD system arranged by two different dielectric materials<sup>[91]</sup>.

During the CO<sub>2</sub> splitting experiments reported in this work, a conductive coating (characterised and described in the next chapter) is also found on the reactor

walls. Interestingly, coke deposition during pure CO<sub>2</sub> processing in a DBD reactor is typically not observed by other authors.<sup>[92-94]</sup> Zheng *et al.* found solid carbonates only when using CO as a feed gas instead of CO<sub>2</sub>.<sup>[95]</sup> On the other hand, Li *et al.* also reported carbon deposition, and associated this to the high-current discharge peaks, resulting from the use of a high-permittivity dielectric.<sup>[34]</sup> Tomai *et al.* utilized a DBD reactor under super-critical conditions to achieve carbon deposition from CO<sub>2</sub> feedthrough.<sup>[96, 97]</sup>

An interesting implication of this conductive coating deposition on the electrodes is the modification of the electrical signal of the CO<sub>2</sub> discharge. A shift from an asymmetric current waveform to a symmetric one is observed and attributed to the appearance of this conductive film on the dielectric surface. To the best of our knowledge, this effect was not described before, although the influence of the dielectric material conductivity or of conductive coatings on the dielectric material was investigated for various gas mixtures.<sup>[35, 98-100]</sup> Both Kim *et al.* and Choi *et al.* correlated the improvement of N<sub>2</sub> discharge uniformity to the conductivity of the dielectric surface.<sup>[98, 99]</sup> Guoqing *et al.* observed a decrease in the number of filaments and in the discharge power for the case of highly conductive dielectric surfaces in a N<sub>2</sub>-Ar mixture.<sup>[100]</sup> Wang *et al.* reported a higher discharge current and efficiency of CO<sub>2</sub> conversion in a MD reactor by means of custom-made high-permittivity dielectrics with a higher concentration of glass, i.e. a lower surface resistivity.<sup>[35]</sup> In this way the effect of the high-permittivity dielectric conductivity on the CO<sub>2</sub> discharge in the MD configuration was explored. However, it is not clear yet whether it is possible to modulate the CO<sub>2</sub> discharge current and CO<sub>2</sub> conversion by means of enhancing the conductivity of conventional dielectric material surfaces (e.g. borosilicate glass, alumina).

To address this problem, we also explore a double dielectric (DD) configuration of a DBD reactor, and we compare it to the MD one, by applying the conductive coating on one of the dielectric layers of the DD reactor. Falkstein *et al.* examined the different operation of the DD configuration in dry and wet air, and associated the rise

of microdischarge amplitude with a water film appearing on the electrodes.<sup>[90]</sup> Brehmer *et al.* utilized a quartz DD reactor for CO<sub>2</sub> decomposition and observed a symmetric waveform with limited discharge current amplitude of about 35 mA, while no carbon deposition was found during the process.<sup>[101]</sup> Tu *et al.* used a DD configuration for dry reforming of methane in a mixture of CH<sub>4</sub> and CO<sub>2</sub> and observed coke deposition, although the effect of the coating on the electrical properties or conversion was not discussed.<sup>[102]</sup> Clearly, there is a lack of understanding in how the reactor wall conductivity can influence the discharge regime and thus the CO<sub>2</sub> conversion. Moreover, such a study is also crucial from the industrial point of view, as the contamination of the electrodes is inevitable in a large scale operation. In this chapter, the introduction of the conductive coating on one of the dielectric walls of the DD configuration significantly enhances the discharge current in one of the HCs and subsequently the CO<sub>2</sub> conversion. To the best of our knowledge, this effect was not yet reported before. In general, it is clear that the surface conductivity of the dielectric walls can greatly influence the electrical current profiles, and thus also the CO<sub>2</sub> conversion, but a systematic study of these effects has not yet been performed. This is exactly the aim of the present Chapter.

### 3-2 System description

To demonstrate the influence of the electrode surface properties on the microdischarge parameters and CO<sub>2</sub> conversion reaction in the DBD reactor, two configurations are utilized (cf. **Figure 2-1**). The Metal-Dielectric (MD) one is the conventional tubular DBD reactor with one metal and one dielectric electrode. In case of the Double Dielectric (DD) configuration, the central electrode is a quartz tube, filled with technical quality water, i.e. conductive water. A grounded stainless steel rod is introduced into the liquid for sustaining electrical contact. Water is circulated for cooling of the quartz tube. In this configuration it is possible to introduce an external

measuring capacitor in the electrical circuit of the reactor to obtain the transferred charge – voltage (Q-U) characteristics.

### 3-3 Electrical characteristics for the MD configuration

**Figure 3-1** shows the applied voltage and measured current waveforms of the MD DBD configuration for CO<sub>2</sub>, as well as for O<sub>2</sub> and N<sub>2</sub>. Indeed, besides CO<sub>2</sub>, we also investigate another electronegative gas (O<sub>2</sub>), as well as an electropositive gas (N<sub>2</sub>), to compare the electrical signals of the discharges. As the critical electric field for N<sub>2</sub> breakdown is lower than that of CO<sub>2</sub> or O<sub>2</sub>, a rather different discharge properties might be expected. The studies performed in the single-filament DBD reactors equipped with advanced optical diagnostics demonstrated that the properties of the microdischarges (maximum charge transfer, duration, radius, etc) can significantly deviated in various discharge configurations<sup>[103]</sup> and various gas mixtures.<sup>[104]</sup> It is known that the total current is a superposition of a quasi-sinusoidal displacement one and numerous discharge pulses. The former corresponds to the capacitive nature of the DBD system and does not depend on the gas composition. Meanwhile, the latter gives evidence for the filamentary character of the discharge, consisting of randomly distributed individual filaments, although the amplitude of these current pulses for CO<sub>2</sub> and O<sub>2</sub> is clearly higher than for N<sub>2</sub>. Moreover, the current waveform of the CO<sub>2</sub> and O<sub>2</sub> discharge appears to be asymmetric, i.e. the discharge current in the positive HC has a different structure than in the negative one.

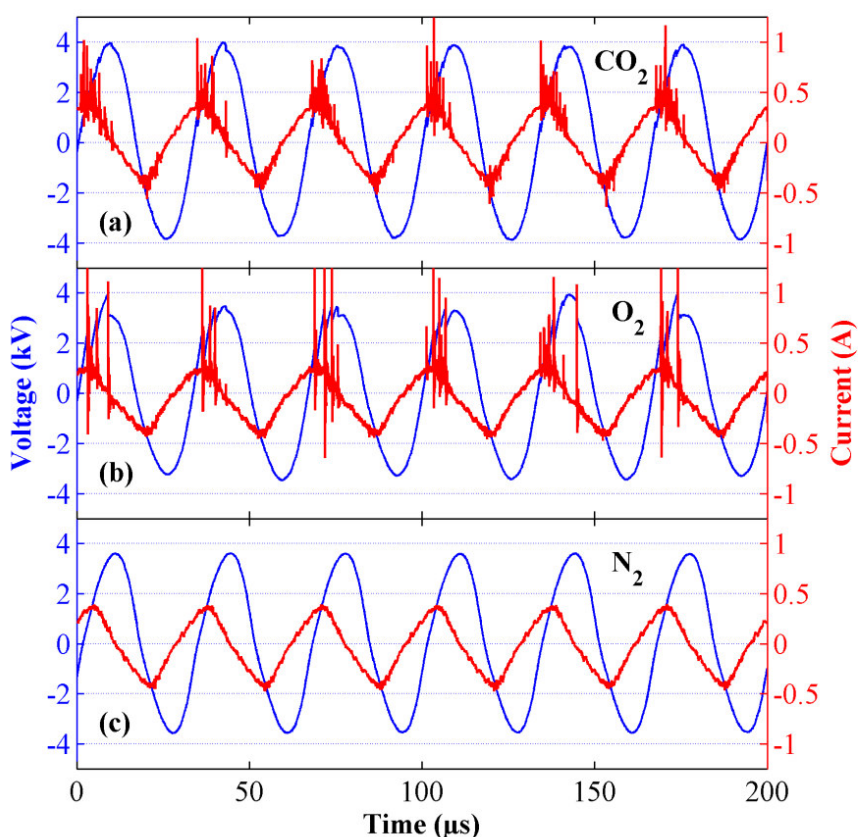


**Figure 3-1.** Electrical signal of the DBD reactor in the MD configuration: (a) CO<sub>2</sub>; (b) O<sub>2</sub>; (c) N<sub>2</sub> (discharge power: 180W; feed flow rate: 0.2 SLM; frequency: 30 kHz for all three cases; dielectric material: alumina).

One period of applied voltage, in case of the CO<sub>2</sub> discharge, is shown in **Figure 3-2** after subtraction of the displacement current from the total current. The discharge current in the positive HC is composed of relatively high sparse peaks (with values up to 1-2 A) and the applied voltage waveform is correspondingly distorted by sharp voltage drops up to 1 kV (better seen in **Figure 3-3, a**), while a more uniform discharge appears in the negative HC. Interestingly, this remarkable asymmetric behaviour is not observed for the N<sub>2</sub> discharge at the same conditions (**Figure 3-1, c**) or other tested gases (Ar, CO, CH<sub>4</sub>). This feature of the CO<sub>2</sub> discharge is observed for the whole range

of discharge gaps examined in our system, ranging from 0.5 to 2 mm, i.e. a central electrode outer diameter between 25 and 22 mm.

Besides the bandwidth of the oscilloscope, the sampling rate (represented in number of samples per second) is the parameter that might influence the precision of measurements. Depending on the frequency of the applied voltage the oscillograms are recorded with a sampling rate from 10 MS/s to 50 MS/s (million samples per second). Up to the tested 2.5 GS/s, the asymmetric structure described above is preserved.

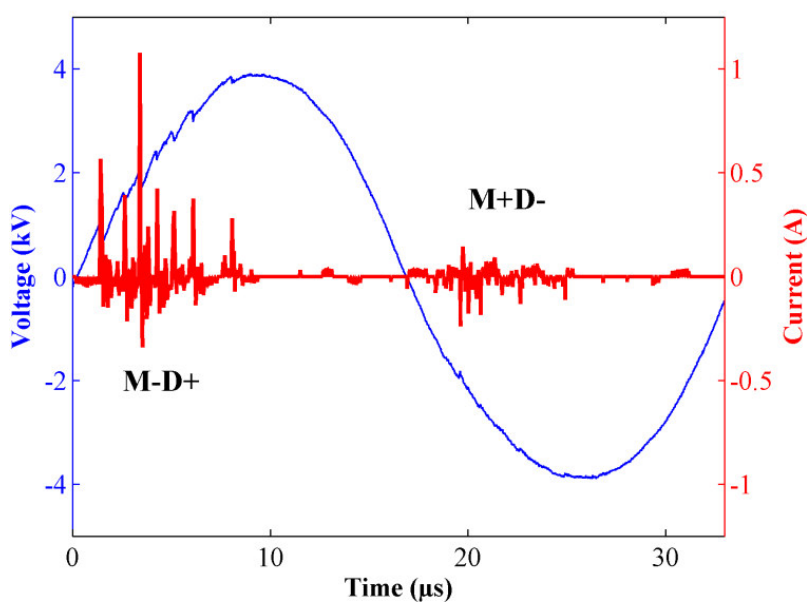


**Figure 3-2.** Electrical signal in one period of applied voltage for the CO<sub>2</sub> discharge (discharge power: 180W; feed flow rate: 0.2 SLM; frequency: 30 kHz; dielectric material: alumina).

The comparison of the pulses for positive and negative HC is presented in **Figure 3-3**. The rise time of the current peaks is about 10 ns and is similar for both HCs. This value is close to usable rise time. The ringing (i.e. oscillation of the measured signal) of the current signal is observed after the current pulse propagation. This effect is known to be a drawback of Rogowski coil current meters.<sup>[87]</sup> As a result of that it is

important to mention that the presented analysis of the microdischarge properties bears rather qualitative character. It is known that synchronization of filaments can take place (which can also be seen **Figure 3-3 (a)**, where several peaks clearly overlap). This will in turn result in the increase of the measured peak amplitude. To quantitatively characterise microdischarge behaviour, the single-filament DBD reactors should be utilised.<sup>[81]</sup>

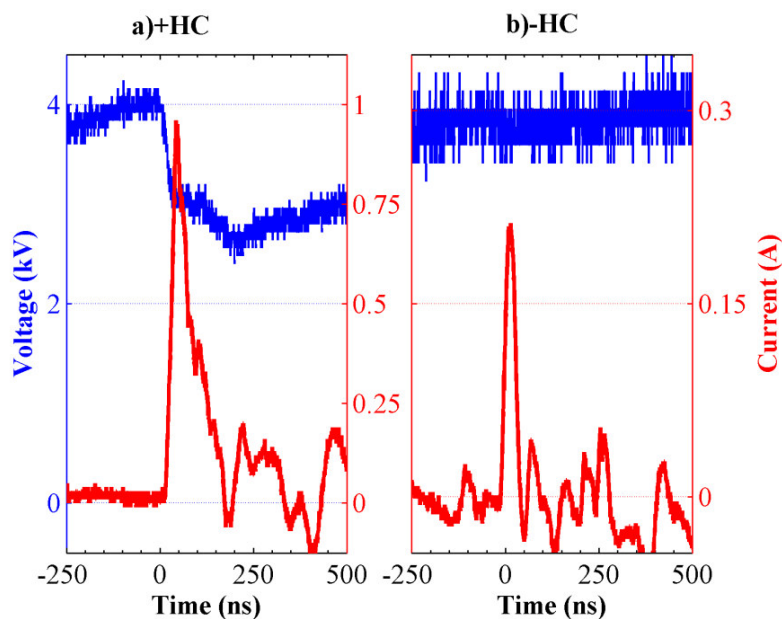


**Figure 3-3.** Measured current and voltage signal for positive (a) and negative (b) HC (180W-0.2 SLM CO<sub>2</sub>-30 kHz).

An asymmetric current waveform was also observed by Guaitella *et al.*<sup>[105]</sup> in a similar metal-dielectric DBD (6 mm gap) system operating in air at 50 Hz excitation frequency. Remarkably, the high-current structure was observed in the M+D- polarity (“M+Q-” notation is used in their paper), which is opposite to our observations. A structure similar to our case of the CO<sub>2</sub> discharge current was observed by Li *et al.* in the MD configuration, although the reported waveforms are not so irregular in the positive and negative half-cycles, possibly because of the high-permittivity dielectric being used.<sup>[33, 34]</sup> The distortion of the voltage signal might be related to the reaction of

the power supply to the high current pulses. A somewhat similar behaviour in terms of current discharge asymmetry and amplitude can be seen on the oscillograms presented by Mei *et al.* for a system with a wider discharge gap of 3 mm.<sup>[36]</sup> In the work by Aerts *et al.*<sup>[41]</sup>, modifications in the waveform due to a rise in discharge gap or energy input variations were presented. No clear asymmetry was observed in this study, and the discharge current amplitude was somewhat lower than in our system. Ramakers *et al.* explored the discharge properties in mixtures of CO<sub>2</sub> with Ar and He.<sup>[106]</sup> Notably different waveforms were presented both for the case of discharges of pure CO<sub>2</sub> and CO<sub>2</sub> diluted with Ar. As will be shown below, the asymmetry of the current waveform is highly dependent on the surface quality of the dielectric material. Contaminated or aged dielectrics can yield a symmetric waveform for a discharge in CO<sub>2</sub>. Another point is that the mesh electrode exposed to the atmosphere can induce a parasitic discharge<sup>[107]</sup>, which will create additional noise in the current measurements. Finally, the discharge conditions (discharge gap, gas flow rate, applied frequency) used by Aerts *et al.*<sup>[41]</sup> and Ramakers *et al.*<sup>[106]</sup> were somewhat different, so it is dangerous to draw conclusions about the different current waveforms.

From the presented waveforms (**Figure 3-1** and **Figure 3-2**), it can be concluded that the discharge regime in case of the electronegative gases (CO<sub>2</sub> and O<sub>2</sub>) is significantly different in the positive half-cycle of the applied voltage, when the grounded electrode has a negative polarity (M-D+ configuration), compared to the negative half-cycle (M+D-). This behaviour is similar to the asymmetric properties of surface barrier discharges<sup>[82-89]</sup> but is in distinct contradiction with the studies of microdischarge formation in a N<sub>2</sub>-O<sub>2</sub> atmosphere<sup>[90, 104]</sup>, where more intense and irregular microdischarges were reported for the M+D- configuration. Moreover, a prominent decrease of the microdischarge amplitude was correlated with the addition of oxygen. However, considering the electronegativity of CO<sub>2</sub> and O<sub>2</sub> and the lower ionization potential of these gases compared to N<sub>2</sub> (i.e., 13.8 and 12.1 eV, vs. 15.6 eV), one might expect sparse and high intensity filaments for the CO<sub>2</sub> and O<sub>2</sub> discharges. Audier *et al.* studied the morphology of surface barrier discharges in mixtures of N<sub>2</sub>-

O<sub>2</sub><sup>[108]</sup>. It was shown that the addition of the electronegative oxygen gas results in fewer, stronger and brighter filaments. Notably, in pure O<sub>2</sub> the current pulses were the strongest, as more filaments were ignited at the same locations, utilizing the strong channels of the extinguished filaments. This is also in correlation with our results, where no strong current peaks are observed in the electropositive N<sub>2</sub> discharge, in contrast to the electronegative CO<sub>2</sub> and O<sub>2</sub> discharges. It might appear that the amplitude of current pulses is limited and thus depends on the capacitance available for a single filament. A somewhat similar behaviour was shown experimentally (for the CO<sub>2</sub> discharge) by Li *et al.*<sup>[33, 34]</sup> and theoretically by Akishev *et al.*<sup>[109, 110]</sup>. Accordingly, the MD discharge asymmetry might be explained by this hypothesis: the capacity of the electron supply (i.e. charge transferred after streamer breakdown) of the M-D+ polarity is significantly larger than in the case of the M+D- one. This allows the flow of high-current pulses of the CO<sub>2</sub> or O<sub>2</sub> discharges in the M-D+ configuration, while the discharge current peaks are limited in the M+D- polarity. The current waveforms present an integrated picture of a bulk discharge, i.e. we cannot deconvolute the information out of it for a single microdischarge. Nevertheless, we can conclude that the microdischarge activity processes are different in the M+D- and the M-D+ configurations.

### 3-3-1 Effect of the conductive film on the discharge properties

As mentioned above, during the experiments on CO<sub>2</sub> decomposition, it is noted that a black-coloured coating is deposited both on the central metal electrode and on the inner surface of the dielectric tube. The formation of the film is observed for both of the tested dielectric materials, i.e. alumina and borosilicate glass. For the borosilicate glass, the adhesion is not so strong and the coating could be removed with a tissue. The achieved coating is absorbing in the visible spectrum, i.e. no light could be extracted through the coated borosilicate glass walls.

The electrical properties of this coating are measured with a multimeter and it is revealed that the coating is conductive. The resistivity value of the powder scratched

from the dielectric tube is in the order of  $1\text{-}2\cdot 10^3$  Ohm·m, which corresponds to resistive material. However, the dielectrics used in the experiments are characterized by several orders of magnitude higher resistivity values ( $10^6\text{-}10^{10}$  Ohm·m for the borosilicate glass and  $10^{10}\text{-}10^{12}$  Ohm·m for the alumina). It should be noted that the resistivity can change drastically with variation of the applied frequency and temperature, thus the behaviour of the material can be rather complex, considering the conditions of the DBD operation.<sup>[29]</sup>

The appearance of the coating is associated with the modification of the current waveform, as shown in **Figure 3-4**. The case when the conductive coating is covering both reactor walls is denoted as “Coated system” while the “Clean system” represents the condition when no conductive coating is deposited. It can be seen that the current waveform shifts from an asymmetric structure (“clean system”) to a symmetric one (“coated system”) with an irregular high peak structure appearing in both negative and positive HC, as described above. Interestingly, the introduction of the conductive coating and the subsequent rise of the discharge current in the negative HC has little or no influence on the efficiency of the CO<sub>2</sub> conversion in the MD reactor configuration. For instance, for an energy input of 60W at 0.2 SLM CO<sub>2</sub> flow, the conversion in the clean system is found to be  $12.9\pm 2\%$ , while a value of  $12\pm 2\%$  is obtained in the coated reactor.

Another point is that the deposited structure might act as a catalyst, enhancing the backward reactions<sup>[66]</sup> and thus decreasing the effect of the current amplification.

The modification of the electrical properties of the CO<sub>2</sub> DBD over time may be presented in the following way. The charge transfer is calculated via the integration of the discharge high-current component ( $I > 35$  mA) (cf. **Figure 3-5**). The value of 35 mA is chosen just to illustrate the transition of the discharge regime and is based on the evaluation of the intensity of the the current peaks in the negative HC. Hence, the modification of the current amplitude distribution for the negative HC might be spotted. In this way we estimate the charge transfer only by a high-current component of the discharge. At the beginning of the operation (“clean system”) only low-current

component is present for the case of the negative HC (the current peaks below 35 mA) and thus is shaved out from the calculation (**Figure 3-5, b**). The coverage of the dielectric surface with a conductive coating induces the higher-current peaks, and thus the charge transferred (**Figure 3-5, "3 hours"**). After several hours of operation (depending on the regime) the stable operation is achieved, as the charge transfer calculated in this way is equal in both HCs.

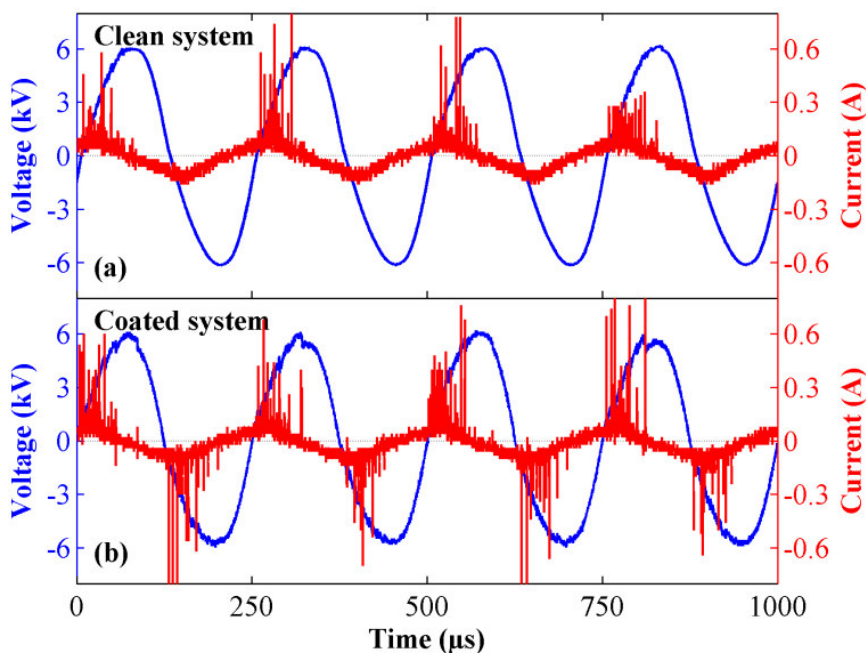


**Figure 3-4.** Electrical signal of the CO<sub>2</sub> DBD reactor, without the coating (a) and with the coated walls (b) (discharge power: 60W; feed flow rate: 0.6 SLM; frequency: 4 kHz; dielectric material: alumina).

Notably, the charge transfer in the positive HC (**Figure 3-5, a**) is rather stable in time, which indicates that the coating is not influencing the discharge in the positive HC. The coverage time is highly dependent on the power input regime, ranging from tens of hours for 1-5 eV/molec. power input down to 1-3 hours for a power input of 10-15 eV/molec.

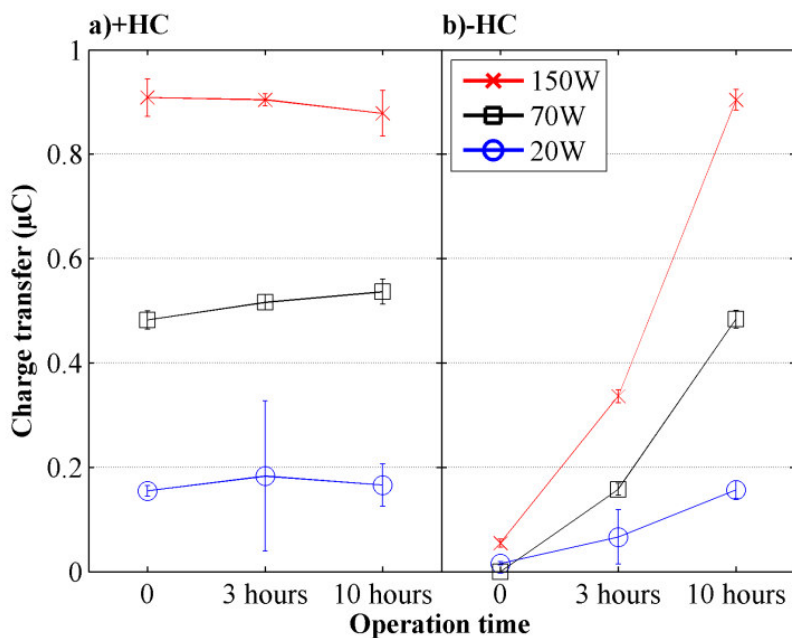


**Figure 3-5.** Charge transfer induced by the high-amplitude component of the discharge current (Discharge current > 35 mA) for the cases of 150W, 70W, 20W – 4 kHz power input at 0.6 SLM CO<sub>2</sub>.

Interestingly, the introduction of a conductive coating does not influence the discharge in the positive HC, while it drastically modified the discharge in the negative HC (**Figure 3-4**). In fact, a shift of the current waveform, i.e. a gradual growth of the amplitude of current peaks in the negative HC, may in general be used as an indication of the appearance of a coating on the dielectric wall. If we consider the discharge configuration of the coated system in the negative HC, we can deduce that it is similar to the M-D+ configuration of the positive HC, as the cathode surface in this case is conductive as well. According to these observations, the conductivity of the cathode surface may be the crucial factor for promoting the discharge current in a CO<sub>2</sub> atmosphere. Unfortunately, in the case of the MD configuration, it is not possible to obtain *Q-U* Lissajous figures to evaluate the influence of the coating on the effective capacitance of the reactor.

## 3-4 Comparison of DD and MD configurations

### 3-4-1 Discharge characterisation in the various configurations

The DD configuration of the reactor is compared with the MD set-up in terms of the electrical properties of the discharge and the CO<sub>2</sub> conversion efficiency. **Figure 3-6** shows the current waveforms of the CO<sub>2</sub> discharge in the different configurations. It can be seen that in the case of the DD configuration (**Figure 3-6**, left) the discharge current is symmetric, with no high current pulses in both HCs, and thus similar to the clean M+D- system during the negative HC of the applied voltage (cf. **Figure 3-1** and **Figure 3-4**, a). To modify the existing DD configuration, a dielectric tube with a pre-deposited conductive coating on the inner surface, resulting from the previous experiments on the MD configuration, is used in the reactor (**Figure 3-6**, right). As a result, the discharge current drastically rises in the negative HC and an asymmetric current waveform is observed. Again, this drastic shift in behaviour is noted only in a CO<sub>2</sub> or O<sub>2</sub> atmosphere, and not in the electropositive gases (N<sub>2</sub>, Ar, CH<sub>4</sub>) that are studied, and to the best of our knowledge, this effect is reported for the first time. Finally, for comparison, also the current waveform of the MD configuration is again plotted (**Figure 3-6**, middle) and it shows high current pulses during the positive HC (cf. **Figure 3-1**, **Figure 3-2**, **Figure 3-4**, a). This effect is tested over a range of the applied voltage frequencies, thus on different transformers, to validate that this phenomenon is not the result of equipment corruption.

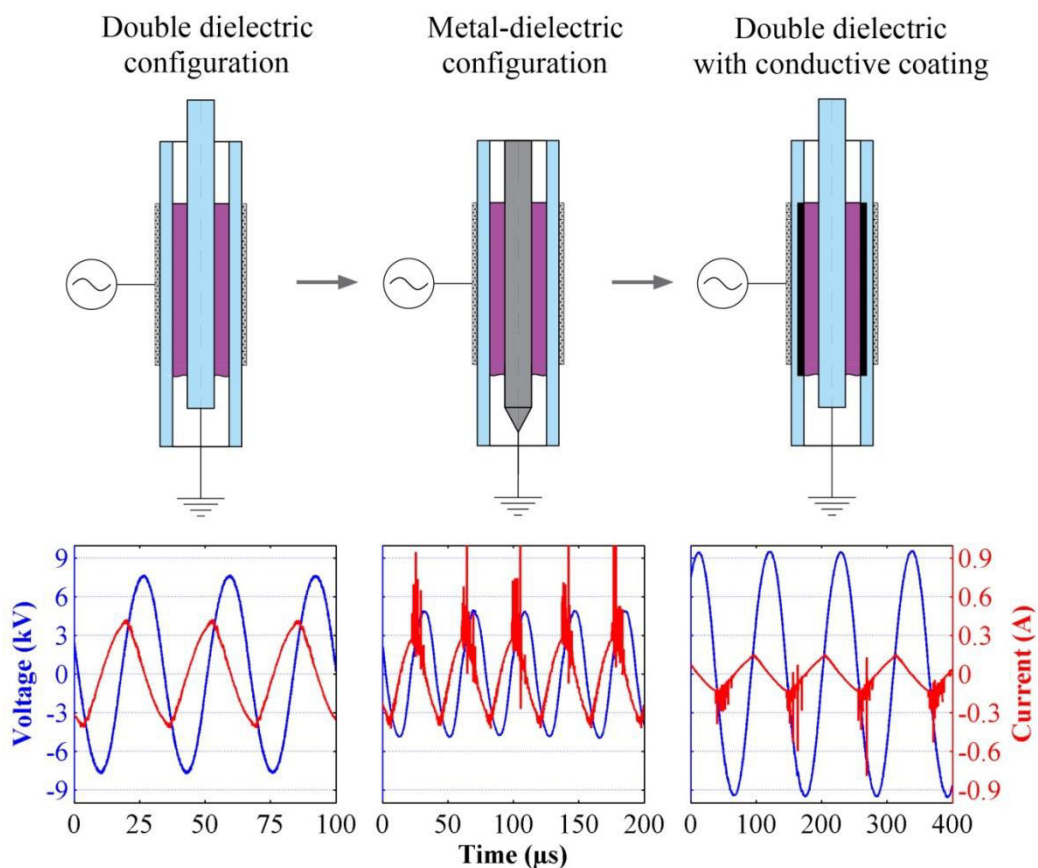


**Figure 3-6.** Comparison of the current waveforms in various reactor configurations (discharge power: 180W; CO<sub>2</sub> feed flow rate: 0.2 SLM; frequency (from left to right): 30 kHz; 25 kHz; 1 kHz; dielectric material: alumina).

To estimate the effect of the conductive coating on the electrical properties of the DD reactor, the relation between the transferred charge and the applied voltage is evaluated. **Figure 3-7** depicts the Lissajous figures of this relation, averaged over 512 cycles. The figure consists of the discharge-off (DA, BC) and the discharge-on (AB, CD) lines. From the slope of these lines, we can estimate the effective capacitance (during the discharge) and the cell capacitance (when only the displacement current is present). Some changes in the Lissajous figure can be observed after the introduction

of a conductive coating, indicating a variation of the sum of the cell and stray capacitances, similar to the observations by Falkenstein *et al.*<sup>[90]</sup>

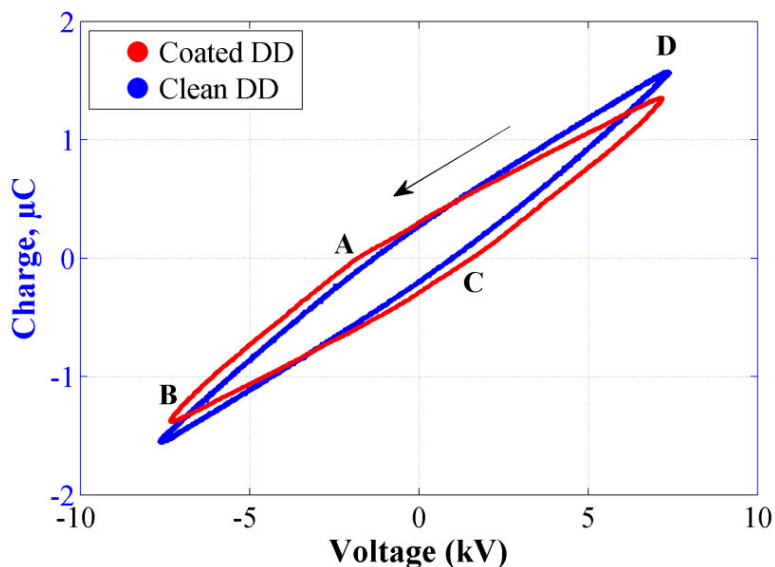


**Figure 3-7.** Lissajous figures of the CO<sub>2</sub> DBD in the DD configurations, with clean and coated dielectric surface (discharge power: 180W; feed flow rate: 0.2 SLM; frequency: 30 kHz; dielectric material: alumina).

By comparing the waveforms in **Figure 3-6**, we can conclude that the conductivity of the cathode surface has a crucial role in the development of the CO<sub>2</sub> discharge current. Indeed, in the clean DD configuration, the discharge zone is composed of only non-conductive surfaces and hence the discharge current is limited in both HCs (**Figure 3-6**, left). In the MD configuration (**Figure 3-6**, middle), the central electrode is a metal body and consequently the high-peak discharge current structure is observed only in the positive HC, when the grounded electrode acts as a cathode. In contrast, in the DD configuration with the conductive coating on the inner surface of the outer dielectric, this pre-deposited conductive film is attached to the power supply in series with the dielectric. Therefore, the coating is a cathode when the applied voltage is negative, enhancing the discharge current pulses in the negative HC (**Figure**

3-6, right). The coating was rather stable, and was preserved even after several hours of operation in CO<sub>2</sub>DBD.

The validation of the Rogowski coil current measurement approach may be done by the comparison of the current signal with the derivative of the capacitor probe charge measurements (cf. **Figure 3-8**).<sup>[111, 112]</sup> It can be seen that the high current peak structure is observed for the negative HC for both measurement systems, while the positive HC is free of the high-amplitude pulses. This indicates that the differences in the positive and negative HCs are related to the discharge current amplitude, and not to the detection limits of the system.

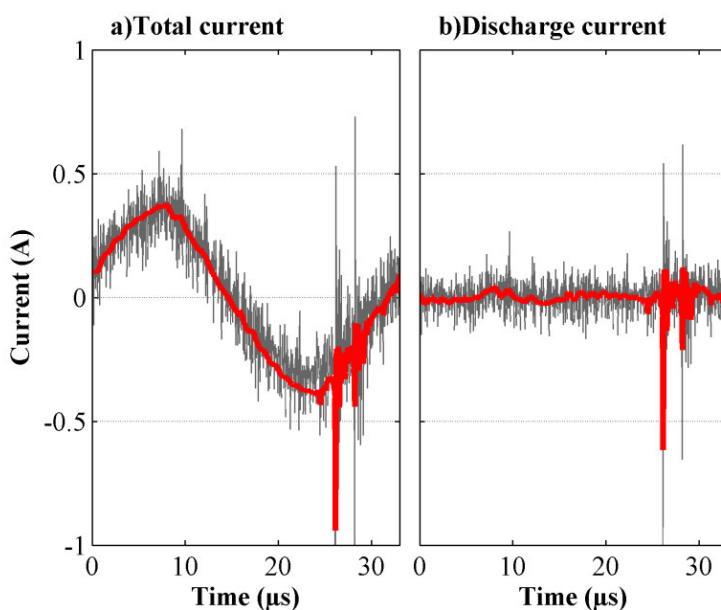


**Figure 3-8.** Comparison of current measurement by means of the Rogowski coil (red) and the derivative of the capacitor probe charge measurements (grey) of the total current (a) and the discharge current (b) achieved after subtraction of the displacement current. CO<sub>2</sub> DBD in the DD configurations, with coated dielectric surface (discharge power: 180W; feed flow rate: 0.2 SLM; frequency: 30 kHz; dielectric material: alumina).

### 3-4-2 CO<sub>2</sub> conversion in the various configurations.

**Figure 3-9** shows the CO<sub>2</sub> conversion as a function of the SEI for the MD and DD reactors, as well as for the DD configuration with a conductive coating on the inner side of the outer dielectric wall. In general, it can be stated that the conversion rises with SEI for all types of reactor configurations. The non-coated DD set-up appears to be the least efficient for the CO<sub>2</sub> decomposition. Upon the introduction of the conductive coating in the DD configuration (so-called coated DD), the conversion drastically rises, but still is somewhat lower than in the MD case. As already mentioned, a conductive coating on the inner side of the outer dielectric has limited or no impact on the conversion in the case of the MD configuration and thus, the data presented here cover both the “clean” and the “coated” MD configuration. The small difference in the capacitance of the clean and coated DD systems (cf. **Figure 3-7**) allows a precise comparison of the process efficiency for those two reactors. However, when comparing the DD and MD configurations, some error would be inevitable due to the larger voltage drop (and thus a power loss) over the two dielectrics in case of the DD setup. This leads to an overestimation of the power input for the DD systems, when comparing to the MD one. This error in power measurement, however, might be avoided if the Lissajous method is utilized to evaluate the energy input of the discharge.

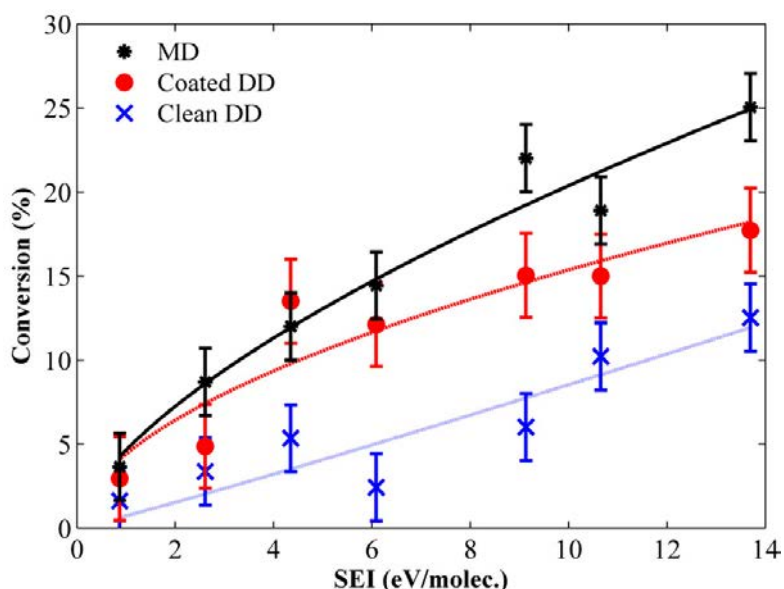


**Figure 3-9.** CO<sub>2</sub> conversion rate for the different DBD configurations, as a function of SEI (frequency: 10-30 kHz; dielectric material: alumina).

These results are consistent with the work of Wang *et al.* who reported that the CO<sub>2</sub> conversion was enhanced by using a custom-made high-permittivity dielectric with a controllable concentration of glass, i.e. controlled surface resistivity.<sup>[35]</sup> The differences in the conversion between the coated DD and the MD configurations may be attributed to the defects of the pre-deposited conductive coating on the dielectric surface. Indeed, visual inspection revealed uncoated areas, which might be explained by the inaccuracy of the coaxial geometry reactor alignment. The possibility of the CO<sub>2</sub> conversion enhancement in the case of the coated DD DBD might also be attributed to the catalytic properties of the film, however due to a relatively limited surface contact with the gas and the short residence time, this effect might be rather limited.

### 3-4-3 OES spectra in the various configurations

Optical emission spectroscopy is a popular technique for non-invasive *in-situ* plasma diagnostics. During the CO<sub>2</sub> decomposition process, the discharge is monitored with a survey spectrometer. The spectrum of the filamentary CO<sub>2</sub> plasma consists of CO<sub>2</sub>/CO<sub>2</sub><sup>+</sup> lines in the range of 300-420 nm (Fox, Duffendack and Barker's System), CO 3<sup>rd</sup> positive band (280-360 nm), CO Angstroms bands in the range between 450 and 700 nm, and a continuum part with a maximum at about 450 nm [46, 101, 113, 114]. No CH or C<sub>2</sub> Swan band lines are observed during the CO<sub>2</sub> experiments. In **Figure 3-10**, the optical emission spectra of the CO<sub>2</sub> discharge in the MD, coated DD and clean DD configurations are presented. The spectra are measured with different integration times (5000, 6000 and 8000 ms, respectively), indicating that the brightness of the discharge (i.e. absolute intensity) in the MD configuration is higher than in the coated DD configuration, and the brightness in the latter is higher than in the clean DD configuration.

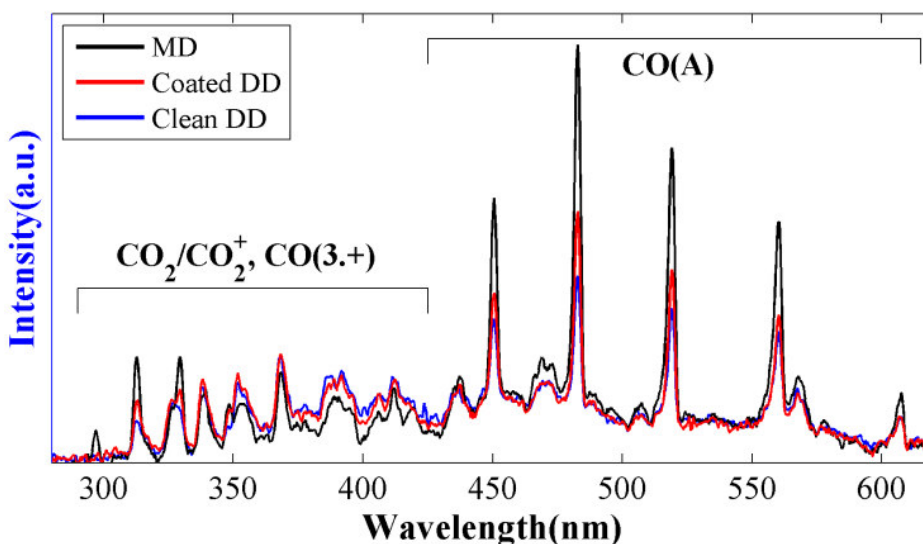


**Figure 3-10.** Emission spectra of the CO<sub>2</sub> DBD in MD, coated DD and clean DD configurations (discharge power: 180W; feed flow rate: 0.2 SLM; frequency: 30 kHz; dielectric material: alumina).

The emission spectra, normalized at the wavelength of 368 nm (as it is the most intensive peak among the CO<sub>2</sub>/CO<sub>2</sub><sup>+</sup> lines), for the 3 configurations in the range of the brightest CO lines (450-570 nm) are shown in **Figure 3-11**.

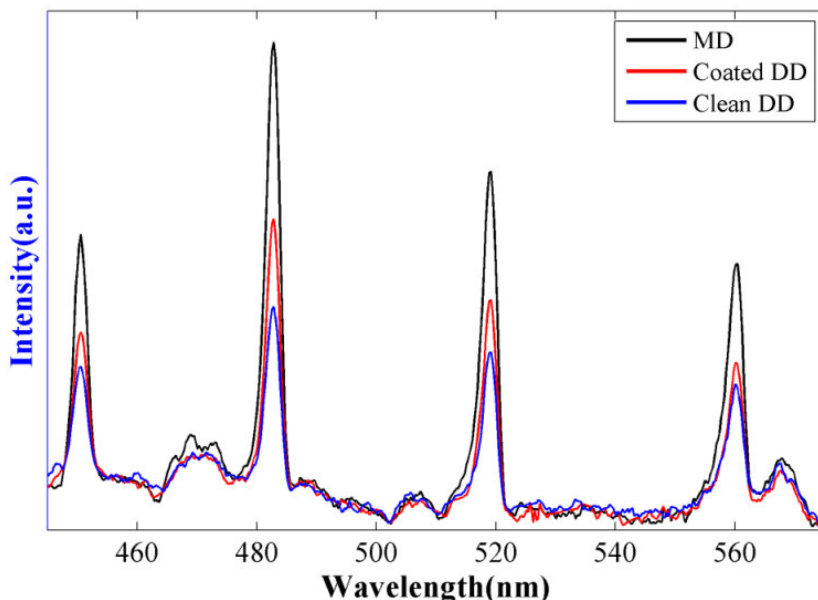


**Figure 3-11.** Emission spectra of the CO<sub>2</sub> DBD, in the three different configurations, normalized at 368 nm (discharge power: 180W; feed flow rate: 0.2 SLM; frequency: 30 kHz; dielectric material: alumina).

The results reveal that the luminosity of the CO<sub>2</sub> discharge in the clean DD configuration is much lower than in the coated DD and especially in the MD set-up. Moreover, the CO lines of the spectrum are relatively more intense in the coated DD and especially the MD reactors, while the intensity of the CO<sub>2</sub>/CO<sub>2</sub><sup>+</sup> lines is virtually the same for all configurations (see **Figure 3-10**). The fact that the CO lines are brighter for the coated DD and MD configurations might be attributed to the intense current pulses observed for these configurations. Thus, the introduction of a conductive coating in the DD configuration enhances the overall brightness of the discharge, as well as the intensity of the lines corresponding to the CO<sub>2</sub> decomposition process. However, the accuracy of the OES analysis is limited due to the alignment issues. Besides, the

increase of the CO lines intensity might be also attributed to the increase of CO concentration in the gas mixture due to the higher conversion.

### 3-5 Discussion

In this study we observed that the CO<sub>2</sub> discharge significantly changes upon modification of the reactor configuration. The introduction of a conductive coating on the dielectric walls of a DBD reactor may change a range of surface properties, including the roughness, the secondary electron emission coefficient, the effective capacitance and the conductivity. Thorough screening of the various factors involved in this process reveals that the conductivity might be the most crucial parameter affecting the discharge properties.<sup>[99]</sup> The effect of the surface conductivity on the discharge properties is somewhat contradictory in the literature, as shown in the Introduction.<sup>[35, 98-100]</sup> Falkenstein *et al.* reported observations similar to the ones presented here, after examining the influence of a conductive water film on a dielectric surface. In this study of a synthetic air DBD, the microdischarge intensity grew in the presence of a water film, making the bulk discharge less uniform.<sup>[90]</sup> It is interesting to note that in our reactor, the simple introduction of a conductive coating on the dielectric surface of the DD DBD results in a notable current waveform modification, as well as in a significant improvement of the CO<sub>2</sub> conversion. A possible reason for this may be found in some changes in the microdischarge formation process.

Fundamental studies on the microdischarge formation report several stages of the process: pre-ionisation, cathode- and anode-oriented streamers and a decay phase.<sup>[29, 79-81, 115]</sup> It is known that charge transfer (i.e. a current pulse) starts after the cathode-oriented streamer reaches the surface of the electrode.<sup>[79]</sup> At this point, electrons are directed towards the anode through a conductive channel, left after the previous phase. In the case of the M-D+ configuration, electrons are supplied from the metal surface. The surface discharge preceding the current transfer is responsible for this process in case of the dielectric cathode, creating a conductive sheet on top of the

barrier.<sup>[90]</sup> Akishev *et al.* introduced the term “local barrier capacitance” for this phenomenon that limits the current passing through the single microdischarge.<sup>[109, 110]</sup> In this work, the dielectric was presented in the form of multiple parallel capacitances, connected by a series of resistances on the surface. The local barrier capacitance may be increased by decreasing the surface resistance in this way, i.e. more electrons might be supplied to the microdischarge channel, forming the current pulse. It seems to be a possible explanation for the discharge current rise when a conductive coating is acting as the cathode surface (**Figure 3-4** **Figure 3-6**). Notably, the conductive surface acting as the anode does not influence the discharge (cf. asymmetric waveform of the clean MD system in **Figure 3-4**, and the coated DD configuration in **Figure 3-6**).

Again, the current waveforms are a superposition of multiple microdischarges over time, thus we cannot spot differences of single microdischarge behaviour in this setup. For this aim, single filament DBD reactors were utilised<sup>[81]</sup>, producing fundamental data on these processes. Nevertheless, we correlate various analysis methods with the bulk discharge current oscillograms. For the clean DD set-up, the discharge current was limited and resembles that of the M+D- configuration. The CO<sub>2</sub> conversion rate and the discharge brightness are correspondingly limited in this case. The introduction of the conductive coating on the dielectric wall enhances the discharge current peaks in the HC corresponding to the time when this surface is acting as a cathode. Consequently, the conversion efficiency and the emission of the CO lines are amplified. In the case of the MD configuration, the conversion rate is the highest and a conductive coating is deposited on the reactor walls. We can therefore assume that microdischarges of higher intensity occur in case of high-peak discharge current structure, leading to the formation of more CO (due to CO<sub>2</sub> decomposition).

According to the current waveforms, the CO<sub>2</sub> discharge is composed of numerous low-amplitude filaments in the clean DD configuration. For the case of the coated DD or MD configurations, sparse high-amplitude current pulses are observed, which could be related to stronger and rare filaments, appearing in the channels of previously extinguished filaments.<sup>[108]</sup> It might be deduced that different plasma

parameters correspond to streamers of those two regimes, such as  $n_e$  should be higher for high-current regimes. From the presented results it might be concluded that high-current pulses, although rather sparse and non-uniformly distributed, are more favourable for CO<sub>2</sub> conversion. The deposited conductive coating is shown to amplify the discharge current, however probably enhancing the backward reaction at the same time. This indicates that a more precise choice of a conductive catalytic coating on the dielectric wall may be beneficial for the process efficiency.

The phenomena of the effect of conductivity on the discharge current may be further studied in a parallel-plate reactor. A controlled conductivity of the dielectric surface may be achieved by thin film deposition techniques. For instance, a thin layer of ITO would possibly allow the utilization of an optically transparent DBD system, resistant to the oxidation of the CO<sub>2</sub> discharge. In this way the measurements of the discharge current might be correlated with the defined conductivity of the surface, speed imaging of the filaments and conversion efficiency. This approach would enable deconvoluted investigation on the role of the surface conductivity in the microdischarge formation process in the electronegative gases (O<sub>2</sub>, CO<sub>2</sub>). Additionally, the analysis of the solid products of the CO<sub>2</sub> discharge would be more straightforward in this type of reactor, as it would be possible to collect the deposited material.

In summary, it is shown that the microdischarge activity of a DD type DBD reactor and the process efficiency in CO<sub>2</sub> splitting can be significantly modified by the introduction of a conductive film on the dielectric surface. In this way, the appearance of a conductive coating can be considered as an activation step for the DD configuration. Indeed, typically high-permittivity dielectric materials are utilized when higher conversions and high-peak discharge currents are observed.<sup>[33-35]</sup> In our work, similar effects are observed upon the introduction of a conductive coating on the surface of conventional dielectric materials (borosilicate glass and alumina). This property might be applied in fundamental studies of DBD systems, where DD reactors are commonly used<sup>[94, 101]</sup>, to simulate processes in the MD configuration.

However, the MD configuration of the DBD reactor seems to be more advantageous for the CO<sub>2</sub> decomposition technology, as the highest CO<sub>2</sub> conversion is achieved in this configuration. Besides, the MD configuration presents a better solution in terms of design based on robust constructional materials.

### 3-6 Conclusion

In this work it is shown that the surface conductivity has a prominent role in the CO<sub>2</sub> discharge in a DBD reactor with various configurations:

- (i) In the clean MD configuration, the CO<sub>2</sub> discharge current is asymmetric, with a high-peak discharge current structure observed during the positive HC (denoted as M-D+);
- (ii) During the CO<sub>2</sub> decomposition process, a conductive coating (which will be described in detail in **Chapter 4**) is found to be covering the reactor walls, and subsequently changing the current waveform into a symmetric waveform with current peaks in both the positive and negative HC;
- (iii) In the clean DD configuration, the discharge current is limited in both HCs, similar to the M+D- phase of the clean MD reactor;
- (iv) In the DD configuration, when using the dielectric tube with pre-deposited conductive coating, i.e., so-called coated DD configuration, the CO<sub>2</sub> conversion, the optical emission signal, and the discharge current in the negative HC are significantly higher than in the clean DD configuration.

All this indicates that the microdischarge activity drastically changes when the conductive surface acts as a cathode. In this way it is possible to control the CO<sub>2</sub> conversion and modify the microdischarge formation process in the DD reactor without using elaborated dielectric materials.

# Chapter 4

## CO and CO<sub>2</sub> DBDs

---

In the previous Chapter the deposition of a conductive coating on the reactor walls is observed during CO<sub>2</sub> DBD operation. This phenomenon can be associated with the high energy input regime, yielding a large CO<sub>2</sub> dissociation rate and thus high concentrations of CO, which is often used as a precursor for carbonaceous material production. In order to evaluate the possibility of solid carbon deposition in CO<sub>2</sub> plasma, CO and CO<sub>2</sub> DBDs are compared at similar energy input, while their solid products are analyzed. GC measurements revealed a mixture of CO<sub>2</sub>, CO, and O<sub>2</sub> in the CO<sub>2</sub> DBD exhaust, while no O<sub>2</sub> is found in the CO plasma. A coating of nanoparticles composed of Fe, O, and C is produced by the CO<sub>2</sub> discharge, whereas a microscopic dendrite-like carbon structure is formed in the CO plasma. Fe<sub>3</sub>O<sub>4</sub> and Fe (metallic iron) crystalline phases are found in the CO<sub>2</sub> sample. The CO deposition is characterized as an amorphous structure, close to polymeric CO (p-CO). Interestingly, p-CO is not formed in the CO<sub>2</sub> plasma, in spite of the significant amounts of CO produced (up to 30% in the reactor exhaust).

---

This chapter has been published as: I. Belov; J. Vanneste; M. Aghaee; S. Paulussen; A. Bogaerts Synthesis of micro- and nanomaterials in CO<sub>2</sub> and CO Dielectric Barrier Discharges. *Plasma Processes and Polymers* 2017 **14** e1600065

## 4-1 Introduction

The dissociation of CO<sub>2</sub> (or CH<sub>4</sub>) in non-thermal plasma (NTP) reactors mainly targets the generation of gaseous products (CO, H<sub>2</sub> or a mixture of both, which is also the main aim of this thesis). Nonetheless, the concept of co-generation of carbonaceous added-value solid products in discharges of greenhouse gases was also explored for thermal plasmas<sup>[70, 116-122]</sup> as well as NTP setups.<sup>[123-127]</sup> In the majority of these studies the deposition of carbon was associated with the decomposition of the initially present or formed methane (or higher hydrocarbons) according to the endothermic reaction (Reaction 4-1)<sup>[128]</sup>:



Carbon reduction in pure CO<sub>2</sub> plasmas presents a more challenging task due to the high dissociation energy of CO (11 eV versus ~5 eV for CH<sub>x</sub>).<sup>[129]</sup> However, the disproportionation reaction (Reaction 4-2) is known to be a more effective path for CO decomposition (activation energy E<sub>a</sub> ~ 6 eV/molecule) and also can be stimulated by plasma exposure due to vibrational and electronic excitation.<sup>[25]</sup>



In this chapter we study the formation of carbonaceous solid products in both pure CO<sub>2</sub> and CO Dielectric Barrier Discharge (DBD) systems. Interestingly, coke deposition is mostly not observed in such DBD reactors when working with CO<sub>2</sub>.<sup>[36, 41, 92, 94, 106, 130-133]</sup> On the other hand, Li *et al.* reported the implementation of a high-permittivity dielectric material ( $\epsilon > 200$ ) in a DBD reactor, which resulted in an enhanced conversion, high-amplitude discharge currents and the formation of presumably carbonaceous deposits.<sup>[34]</sup> Furthermore, Tomai *et al.* utilized a DBD cell operating with super-critical CO<sub>2</sub> to synthesize nanostructured carbon materials.<sup>[96, 97]</sup> Mori *et al.* generated carbon nanotubes and other nanomaterials in a hybrid DBD-Solid Oxide Electrolyser Cell (DBD-SOEC) reactor.<sup>[127]</sup> When oxygen was *in-situ* extracted from the discharge zone, the CO<sub>2</sub> conversion was reaching 100%.

In packed-bed DBD reactors (i.e., DBD systems in which the discharge space is filled with dielectric beads)<sup>[36, 39]</sup> solid products of the CO<sub>2</sub> discharge were observed and associated with the electric field enhancement near the contact points of the dielectric beads.<sup>[134]</sup> In the recent work of Yap *et al.* it was demonstrated that a highly reactive CO<sub>2</sub> plasma can not only form carbonaceous structures, but also etch the material of the glass beads and re-deposit composite structures.<sup>[38]</sup>

In contrast to CO<sub>2</sub>, a rather effective deposition process can be realized in a CO atmosphere via chemical vapor deposition systems<sup>[135-138]</sup> as well as plasma setups.<sup>[139-141]</sup> Furthermore, Mori and colleagues demonstrated the production of various nanomaterials via vacuum glow<sup>[142, 143]</sup> and MW<sup>[144-147]</sup> discharges operating in CO atmosphere with Ar, H<sub>2</sub> and O<sub>2</sub> admixtures. However, rather limited information is available on atmospheric pressure CO discharges. Zheng *et al.* found solid carbonates when using CO as a feed gas in a DBD reactor instead of CO<sub>2</sub>.<sup>[95]</sup> Geiger and Staack presented a study of a CO DBD and characterized the formed deposits as carbon suboxide (C<sub>3</sub>O<sub>2</sub>) polymer.<sup>[148]</sup> Unfortunately the morphology and crystallinity of the achieved solid products were not discussed in both cases.

In the previous chapter the deposition of a slightly conductive coating on the reactor walls was observed in a CO<sub>2</sub> DBD. This phenomenon can be associated with the high energy input regime (up to 80 eV/molecule), issuing a large CO<sub>2</sub> dissociation rate (20-50%) and thus high CO concentrations (10-30 mol. %). At the same time as stated above, CO is often used as a precursor for deposition of carbonaceous products. In this way it is interesting to consider the possibility to generate solid carbon material in a CO<sub>2</sub> DBD, while, as already noted, observations of deposit formation in pure CO<sub>2</sub> discharges are quite rare, and only a few studies on atmospheric pressure CO plasmas are available. For this reason a comprehensive analysis and comparison of CO and CO<sub>2</sub> discharges and their solid products is very interesting from both a material science and a plasma chemistry point of view.

In this Chapter, CO<sub>2</sub> and CO discharges as well as their solid products are compared in a cylindrical DBD reactor. In this way our initial hypothesis of CO formation and

disproportionation in CO<sub>2</sub> plasma can be verified. Hence, the question to be answered is the following: will the CO and CO<sub>2</sub> discharges give rise to similar deposits at similar conditions and if not, what are the main differences between those plasmas?

## 4-2 System description

The DBD reactor in the Metal-Dielectric (MD) configuration (**Figure 2-1, a**) is utilised in this study. To compare the exhaust composition of the CO and CO<sub>2</sub> DBDs, the gaseous products of the reaction are analysed by gas chromatography, equipped with a Thermal Conductivity (TCD). A survey fiber spectrometer with 2.3 nm FWHM resolution is used for monitoring the process, collecting light through a 6 mm collimating lens. The lens is pointed on the discharge gap through an optical window installed downstream the reactor parallel to the electrode axis. The material is collected from the inner surface of the dielectric tube in the form of a powder. Typically the amount of the collected sample is in the order of 0.035-0.5 g after 1-5 hours of discharge operation.

## 4-3 Discharge comparison: electrical signals

The plasma obtained in the DBD is composed of numerous microdischarges (also called filaments) with a typical channel diameter of 0.01-1 mm.<sup>[29]</sup> Each filament might be considered as a single chemical reactor, where reactions are driven by the charged particles accelerated in the electric field.<sup>[28]</sup> The charge transfer of a microdischarge (MD) is limited by a dielectric layer, preventing spark or arc (i.e., constricted high-current, thermal discharges) formation. In this way, the low-current filaments are spread over the barrier surface, maintaining rather low-temperature non-equilibrium conditions in the whole reactor volume. Interestingly, in DBD systems one cannot directly control the discharge current by increasing the applied voltage: the value is determined mainly by the gas composition, gap size and the dielectric material.

Moreover, a higher input power (or applied voltage) will not result in an enhancement of the charge transfer through a single filament, but it will rather increase the number of microdischarges per HC.<sup>[25, 133]</sup>

The electrical signals of the CO<sub>2</sub> and CO discharges obtained at the same power are compared in **Figure 4-1**. The CO<sub>2</sub> plasma gives rise to an asymmetric current waveform with respect to the positive and negative half-cycles (HC) of the applied voltage. High-amplitude (up to 0.5-1 A) sparse current pulses and simultaneous voltage drops (up to 0.5-1 kV) are observed during the positive HC. A more stable filamentary regime with smaller current peaks of about 50 mA (barely visible in **Figure 4-1, a** due to the scale) and no distortion of the applied voltage can be noted in the negative HC. The asymmetry of the CO<sub>2</sub> DBD current waveform is discussed in the previous Chapter. This behaviour is found to be consistent for O<sub>2</sub> and CO<sub>2</sub> gases and is changing with the appearance of a coating inside the dielectric tube. It can be attributed to the electronegativity of the CO<sub>2</sub> molecule and the formation of O<sub>2</sub> (with even more pronounced electronegativity) in the CO<sub>2</sub> discharge.

On the other hand, the discharge current in the CO plasma (cf. **Figure 4-1**) is symmetrical, with 35-50 mA amplitude current bursts measured in both HCs (also barely visible in **Figure 4-1, b**).

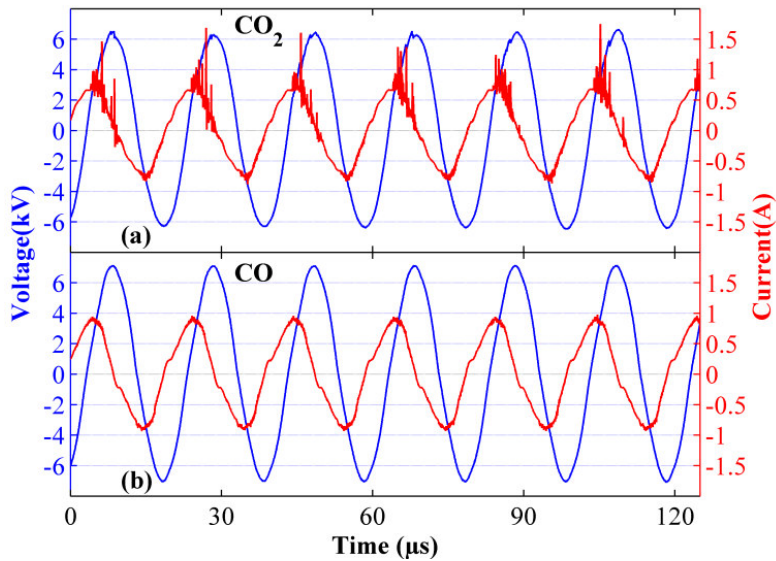


**Figure 4-1.** Electrical signal of the (a) CO<sub>2</sub> and (b) CO DBD (Discharge power: 600 W; gas flow rate: 1 SLM; frequency: 50 kHz).

In our system it is not possible to retrieve precise information regarding a single microdischarge due to the ignition of several filaments at the same time and thus overlapping signals in the current waveform. However, we can conclude that intensive and sparse filaments can be observed in the CO<sub>2</sub> discharge (at least in the positive HC) while more uniformly spread lower energy (i.e. lower current) microdischarges are present in the CO DBD.

#### 4-4 Discharge comparison: gas phase analysis

The efficiency of the CO<sub>2</sub> dissociation and the exhaust composition of the CO<sub>2</sub> discharge are evaluated by means of gas chromatography, which allows separation and quantification of the compounds present in the gas mixture due to differences in column retention times. The concentrations of the products in the exhaust of the DBD reactor are calculated according to Reaction 4-3:

$$\text{Molar concentration } (CO_2 / CO / O_2) (\%) = \frac{[CO_2 / CO / O_2]}{[CO_2 + CO + O_2]} \times 100\% \quad 4-3$$

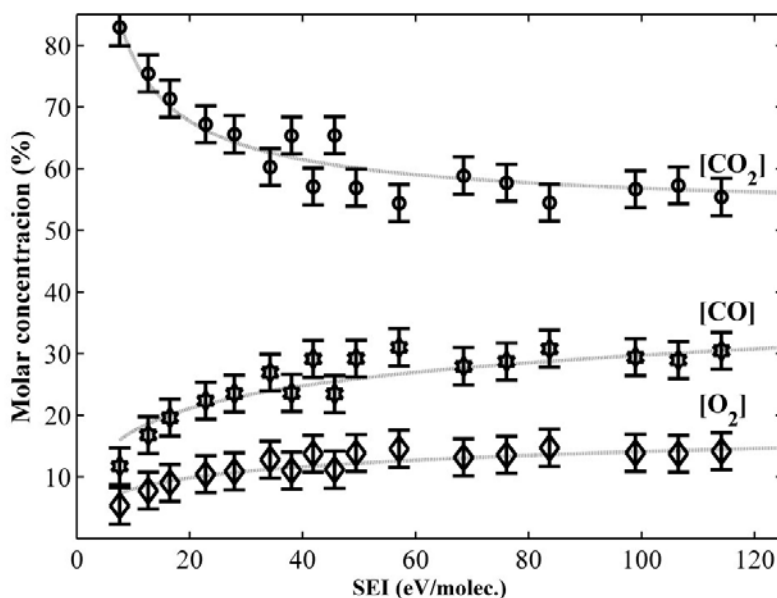


**Figure 4-2.** Molar concentrations of the CO<sub>2</sub> discharge products as a function of the specific energy input (SEI).

The results of the CO<sub>2</sub> dissociation experiments in the DBD reactor are presented in **Figure 4-2**. By varying the specific energy input (SEI) in the range between 5 and 115 eV/molecule, conversion levels between 20 and 50% are obtained. Interestingly, by increasing the SEI above 60 eV/molecule, a plateau is reached with respect to the conversion. The ratio of the product yields ( $[CO]/[O_2] \sim 2.1$ ) is close to the stoichiometric one, indicating the dominance of the overall Reaction 1-1. The data presented in **Figure 4-2** are based on the variation of both flow and power, as the specific energy input is known to be the prevailing parameter in the CO<sub>2</sub> dissociation process.<sup>[41]</sup>

In the case of the CO discharge, only CO and low amounts of CO<sub>2</sub> (order of 1-6 mol. %; cf. **Table 4-1**) are found in the outlet gas of the reactor. The amount of CO<sub>2</sub>

produced is proportional to the specific energy input. Interestingly, no O<sub>2</sub> can be detected in the reactor exhaust by means of gas chromatography.

As already noted, a higher power input increases the number of microdischarges per half-cycle, thus a single molecule will more often be subject to electron impact collisions, resulting in higher CO<sub>2</sub> conversions.<sup>[133]</sup> According to Aerts *et al.*, electron impact excitation followed by dissociation (cf. Reaction 4-4) is dominant for a DBD plasma and is the major reaction in the CO<sub>2</sub> decomposition process.<sup>[48]</sup>

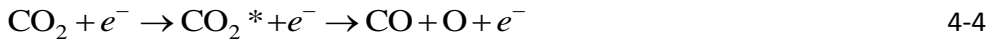


**Table 4-1.** CO<sub>2</sub> production in the CO discharge at 400 W and various feed flow rates (0.1-1 SLM) and corresponding specific energy input (SEI) values and gas residence times.

400 W CO Discharge			
[CO <sub>2</sub> ] [mol.%]	Feed flow rate [SLM CO]	SEI [eV/molec.]	Res. time [s]
0.8	1	6.1	0.5
1.6	0.5	12.1	1.03
2.5	0.25	24.3	2.07
6.2	0.05	121.7	10.2

For the non-equilibrium CO plasma, it was demonstrated that the excited molecule CO(a<sup>3</sup>Π) participates in Reaction 4-5 and it can be produced by vibrational and electronic excitation (cf. Reactions 4-5 and 4-6, respectively).<sup>[149]</sup> This might be the mechanism of CO<sub>2</sub> production in a CO discharge. Thus, the higher CO<sub>2</sub> formation upon increasing SEI (cf. **Table 4-1**) can be purely explained by the higher residence time.



It is important to mention that gas chromatography allows only the evaluation of the overall reaction products, while within the discharge, a more complex mixture of species contributes to the reactions taking place. For instance, it is known that also atomic oxygen and ozone are formed in the CO<sub>2</sub> plasma,<sup>[41]</sup> while other techniques (not available in this study) are needed to detect and quantify them.<sup>[11, 94, 150]</sup>

#### 4-5 Discharge comparison: optical emission spectroscopy

Optical emission spectroscopy is a popular technique for non-invasive *in-situ* plasma diagnostics. One can obtain valuable information on excited atomic and molecular states and determine the rotational, vibrational and electronic excitation temperatures of the plasma.<sup>[151]</sup>

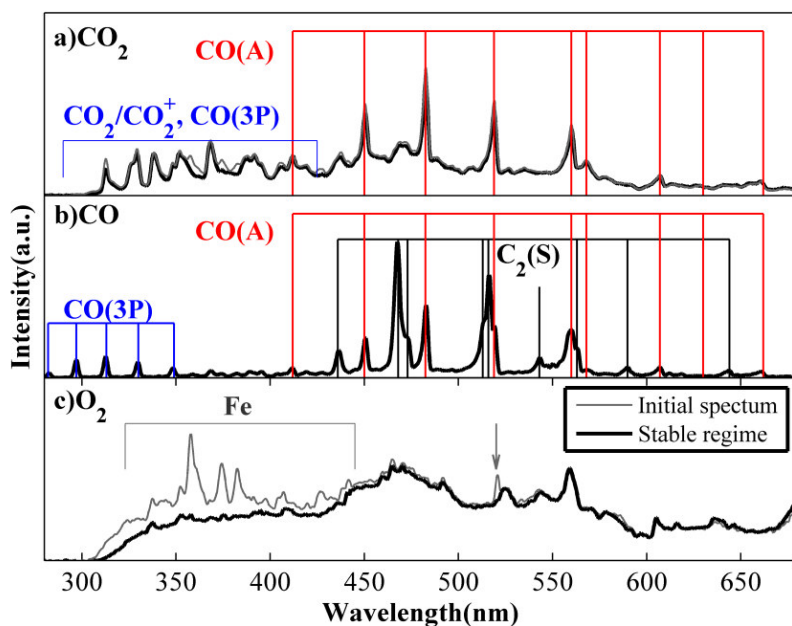


**Figure 4-3.** Measured optical signals of a DBD plasma in (a) CO<sub>2</sub>; (b) CO; and (c) O<sub>2</sub> at 600 W and 1 SLM gas flow rate.

The spectrum of the filamentary CO<sub>2</sub> plasma (cf. **Figure 4-3, a**) consists of the Fox system CO<sub>2</sub>/CO<sub>2</sub><sup>+</sup> lines in the range of 300-420 nm, the CO 3<sup>rd</sup> positive band (CO(3P) at 280-360 nm), CO Angstrom bands (CO(A)) in the range between 450 and 700 nm,

and a continuum part with a maximum at about 450 nm.<sup>[46, 101, 113, 114]</sup> No distinct C<sub>2</sub> lines are observed during the CO<sub>2</sub> experiments even at the highest energy input regimes. Interestingly, atomic Fe lines (320-440 nm) are observed in the first 1-2 hours of the DBD reactor operation. The Fe peaks are hard to spot in a CO<sub>2</sub> discharge due to overlap with the CO<sub>2</sub>/CO lines in the same wavelength region. To better illustrate this effect, the spectrum of an O<sub>2</sub> discharge is shown in **Figure 4-3, c**. The spectrum consists mostly of a continuum part, and thus the iron lines are much more clearly visible. In this case it is also found that the iron lines are the brightest at the initiation of the discharge (“Initial spectrum” in **Figure 4-3, c** and they also disappear after 1-2 hours of operation (“Stable regime”). A similar behaviour is thus found for the CO<sub>2</sub> discharge as well. The Fe species detected by OES obviously originate from the central stainless steel electrode, which is covered with a smooth black coating after discharge operation.

The emission spectrum of the CO DBD is presented in **Figure 4-3, b**. Similar to the results reported by Geiger, it consists of the CO 3<sup>rd</sup> positive (CO(3P); 280-360 nm), CO Angstrom (CO(A); 450 -700 nm) and C<sub>2</sub> Swan bands (C<sub>2</sub>(S); 430-660 nm).<sup>[148]</sup> Moreover, the intensity of the C<sub>2</sub>(S) lines increases upon increasing CO flow rate at constant input power, as demonstrated in **Figure 4-4**. The spectra presented in this picture are given in normalized units, relative to the 482.8 nm line (the brightest CO(A) line). It can be seen that the relative intensity of the C<sub>2</sub> peaks rises drastically with increasing CO feed flow rate.

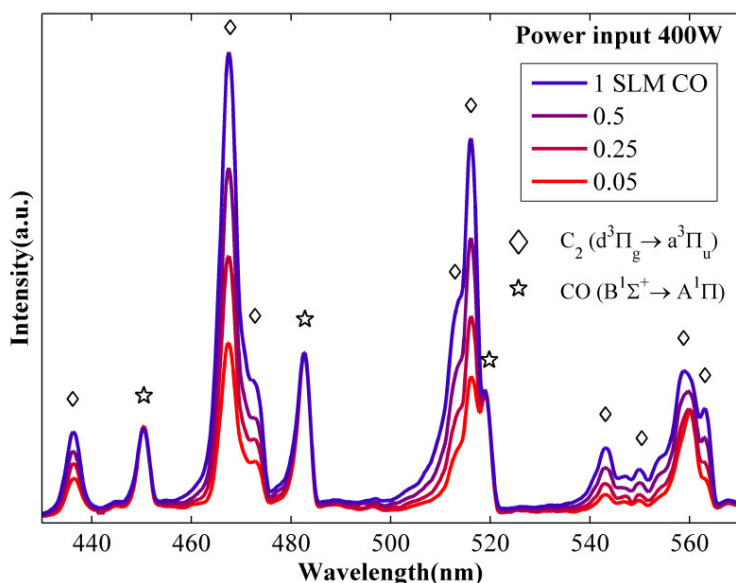


**Figure 4-4.** Emission spectrum of the CO discharge at 400 W and various feed flow rates (normalized at 482.8 nm).

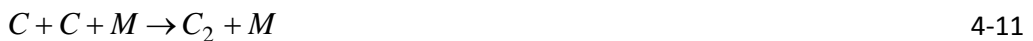
The absence of C<sub>2</sub> lines in the CO<sub>2</sub> discharge spectra is quite typical for non-thermal plasma systems.<sup>[94, 96]</sup> The Swan band is, however, observed in atmospheric CO<sub>2</sub> MW discharges.<sup>[66, 152, 153]</sup> On the other hand, Kameshima *et al.* reported the emission of C<sub>2</sub> lines in a CO<sub>2</sub> DBD system, and correlated this to the removal of carbon deposits of the preceding CO<sub>2</sub>-CH<sub>4</sub> discharge.<sup>[107]</sup> Tomai *et al.* also observed Swan bands in a CO<sub>2</sub> DBD when increasing the pressure above atmospheric pressure up to 2 MPa.<sup>[96]</sup> CO non-equilibrium plasmas, in contrast, do often contain C<sub>2</sub> bands in their emission spectra.<sup>[142, 143, 145, 148, 154]</sup> Interestingly, an admixture of oxygen or hydrogen can cause the suppression of these lines and subsequently also of the carbon deposition, as noted by Mori.<sup>[143]</sup> One might argue that the oxygen-rich atmosphere in the CO<sub>2</sub> plasma is responsible for the depletion of C and C<sub>2</sub>O via the Reactions 4-8, 4-9, 4-10.



As C and C<sub>2</sub>O are the precursors of the C<sub>2</sub>-radical (cf. Reaction 4-11, 4-12, 4-13 below), this might explain the suppression of the Swan bands in the atmospheric pressure CO<sub>2</sub> DBD.

The appearance of atomic iron lines in the CO<sub>2</sub> discharge spectrum might be associated with intensive oxidation and ablation of the stainless steel electrode surface. A somewhat similar behaviour of metal atomic lines is found for aluminium foils exposed to low-pressure oxygen plasmas.<sup>[155, 156]</sup> The extinction of the bands with increasing exposure time can be explained by the formation of a barrier oxide layer on the treated surface and the subsequent suppression of material diffusion to the gas phase.

The higher C<sub>2</sub> Swan relative line intensities for higher CO flow rates shown in **Figure 4-4** are at first glance somewhat contradictory to the data presented in **Table 4-1**. Indeed, in our study we associate the formation of C radicals and CO<sub>2</sub> in a CO plasma with the disproportionation reaction (Reaction 4-2). Thus one might expect that a higher CO<sub>2</sub> production would indicate that similarly more C and thus also more C<sub>2</sub> species are formed, making the C<sub>2</sub>(S) bands more prominent. However, the CO<sub>2</sub> concentration grows upon decreasing CO flow rate, while the C<sub>2</sub>(S) intensity shows the opposite trend. However, according to Caubet, the C<sub>2</sub>-radical creation is governed by Reactions 4-11, 4-12, 4-13 and is shown to be stimulated by a higher CO concentration.<sup>[154]</sup> This behaviour might be applicable to our system as well and explain the enhancement of the C<sub>2</sub>(S) lines upon increasing CO feed flow rate.



## 4-6 Solid products analysis

In this section the properties of the micro- and nanostructures formed in the CO and CO<sub>2</sub> discharges will be analyzed. The comparison of the CO and CO<sub>2</sub> DBD deposits is made for a power of 600 W and 1 SLM gas flow rate (corresponding to a SEI  $\sim 9$  eV/molecule). It is important to mention that the synthesis process is not optimized in any way, although the energy input regime is empirically chosen in order to maximize the growth rate of solid products in the CO<sub>2</sub> discharge. Both discharges also issued deposition  $\sim 1$  cm downstream of the plasma zone.

Deposits are collected in the form of a powder from the inner surface of the dielectric tube (cf. **Figure 4-5**). The 600 W discharge with 1 SLM gas flow generated 15 mg/min of solid products for the CO feed (denoted as "COd") and 0.15 mg/min for the CO<sub>2</sub> DBD ("CO2d"). These numbers are approximations due to the non-optimized collection system and are estimated upon the weight of the gathered material.

The deposition of the CO2d sample can be monitored via the increase of the current peak intensities during the negative HC of the applied voltage, a property that is described in the previous chapter. The coating of the inner surface of the glass tube and the corresponding distortion of the current waveform can be clearly observed after 1 hour of discharge operation at the given conditions. However, the CO2d sample (45 mg) is collected after 5 hours of CO<sub>2</sub> discharge operation, while an amount more than sufficient for analysis of the COd powder (>300 mg) is collected already after 30 minutes of discharge operation. The CO DBD is tested to operate stably after 1 hour of work without discharge extinction.

### 4-6-1 Morphology and elemental composition

The SEM images of the formed structures are presented in **Figure 4-5**. XPS analysis is employed to verify the elemental composition of the deposits. Pointy micrometer-scale structures are formed in the CO plasma. Somewhat similar morphology of carbon structures is attributed as a "dendrite" in the literature.<sup>[157, 158]</sup> Atomic concentrations

of C/O= 73% /27% are obtained by EDS, while C/O= 63% /37% concentrations are measured by XPS. Variations in energy input results in slight morphological variations, as depicted in the SEM image of the 400 W - 0.25 SLM CO discharge deposits (cf. **Figure 4-6**). A somewhat more disordered or irregular structure can be observed when compared to the deposits obtained in the CO discharge at the higher flow rate of 1 SLM; **Figure 4-5**, left). However, the appearance of the deposited material, i.e., the pointy dendrite-like structure, is preserved.

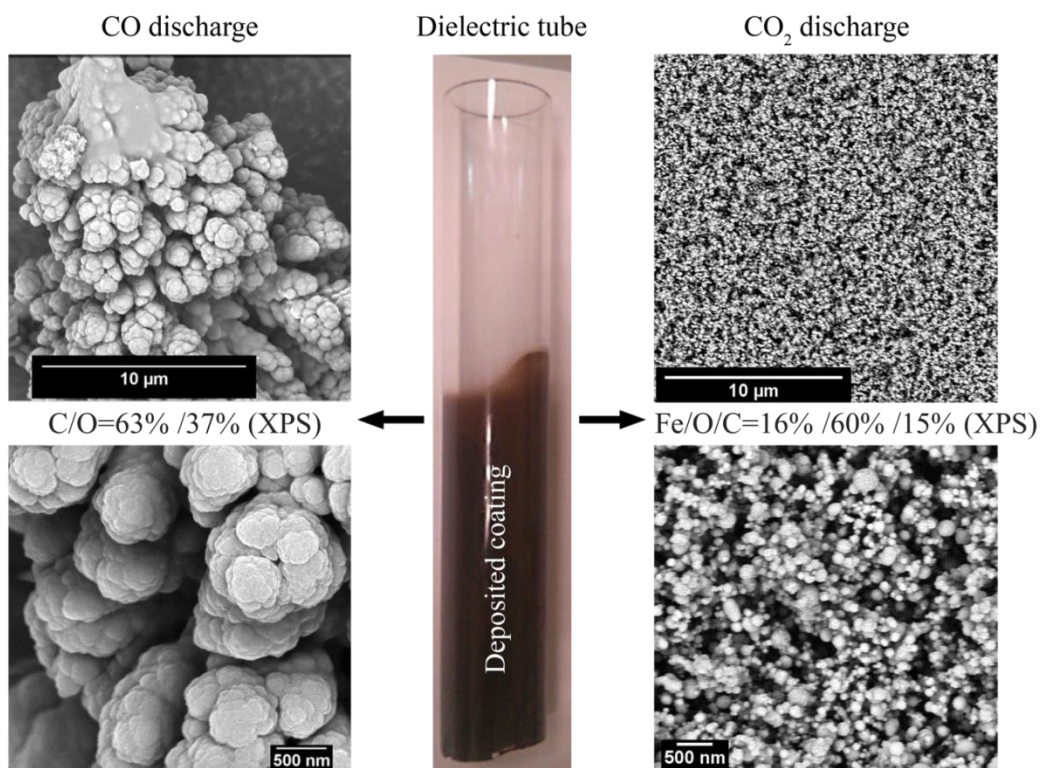


**Figure 4-5.** SEM images of the CO and CO<sub>2</sub> discharge products (denoted as COd and CO2d) at 600 W and 1 SLM (9.1 eV/molecule).

The CO<sub>2</sub> discharge deposits a coating composed of spherical nanoparticles, 10-300 nm in diameter (see **Figure 4-5**, right). A substantial degree of particle agglomeration can be observed on the STEM image in **Figure 4-7**. EDS analysis reveals

the presence of iron, oxygen, carbon with atomic concentrations of Fe /O /C = 13% /50% /30% and traces of the stainless steel alloying elements (Cr, Mo, Ni, Si) with overall atomic concentration of 7%. Interestingly, the XPS measurements shows a somewhat different composition, i.e. Fe/O/C= 16% /60% /15% with 9% concentration of trace elements. This can be explained by difference in the probing depth of the two techniques.

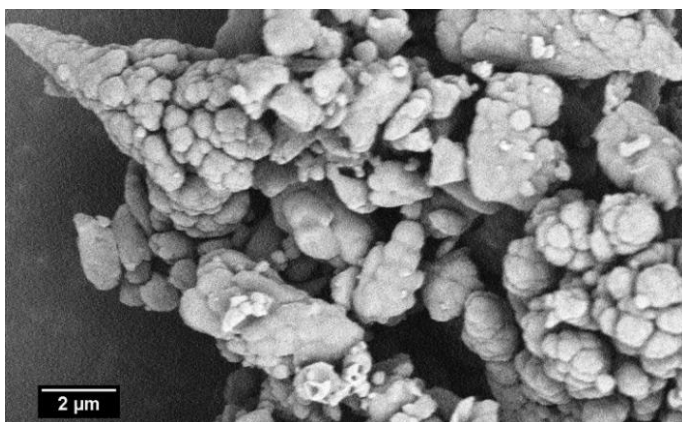


**Figure 4-6.** SEM image of the CO discharge product (COd) at 400 W and 0.25 SLM (24.3 eV/molecule).

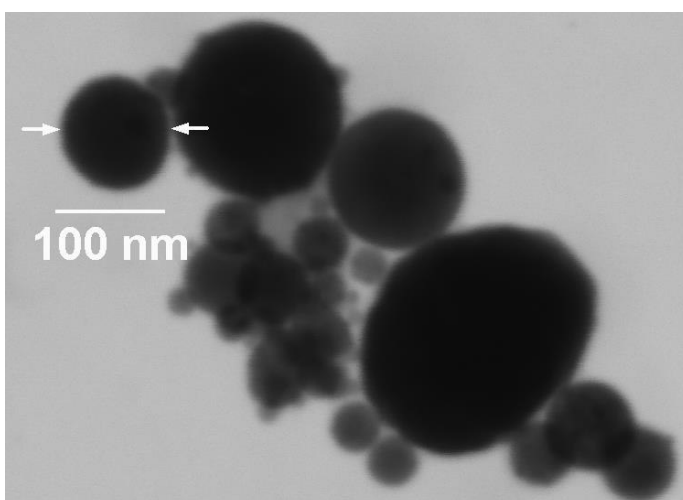


**Figure 4-7.** STEM image of nanoparticles agglomerate formed in the CO<sub>2</sub> discharge at 600 W and 1 SLM (9.1 eV/molecule).

## 4-6-2 Structural characterization

Thorough characterization is a necessary step for identification of the material properties and at the same time it provides information regarding the possible synthesis mechanisms of the solid products. FTIR, Raman Spectroscopy and XRD analysis are applied to characterize the achieved structures.

### (a) FTIR

FTIR diagnostics allows determining the nature of the chemical bonds present in the studied material. The transmittance spectrum of the COd sample (cf. **Figure 4-8**, **Figure 4-9**) shows prominent carbon-oxygen ( $1720\text{ cm}^{-1}$  and  $1220\text{ cm}^{-1}$  for the double and single bonds, respectively) and carbon-carbon ( $1625\text{ cm}^{-1}$ ) peaks. The peaks around  $1420\text{ cm}^{-1}$  and  $1040\text{ cm}^{-1}$  might be attributed to carbon-carbon and carbon-oxygen bonds characteristic for aromatic and ether structures.<sup>[148]</sup> Also due to the random polymeric structure of the COd sample, the presence of the conjugated bonds C=C and C-C bonds might be expected, however on the FTIR spectra only C=C bonds are observed.

The variation of the CO gas flow rate (and thus SEI) results in the shifts of the C=O (red shift) and C-O (blue shift) peaks, as illustrated in **Figure 4-9**. For instance, the C=O peak at 0.05 SLM is located at  $1720\text{ cm}^{-1}$ , while at 1 SLM it appears as a double peak at  $1785\text{ cm}^{-1}$  and  $1730\text{ cm}^{-1}$ .

The Fe-O ( $580\text{ cm}^{-1}$ ) peak dominates the FTIR spectrum of the CO<sub>2</sub>d sample (cf. **Figure 4-8**).<sup>[159]</sup> In addition, smaller peaks at  $1630\text{ cm}^{-1}$  and a broad one at  $1350\text{ cm}^{-1}$  can be attributed to C=C and C-O bonds, respectively.

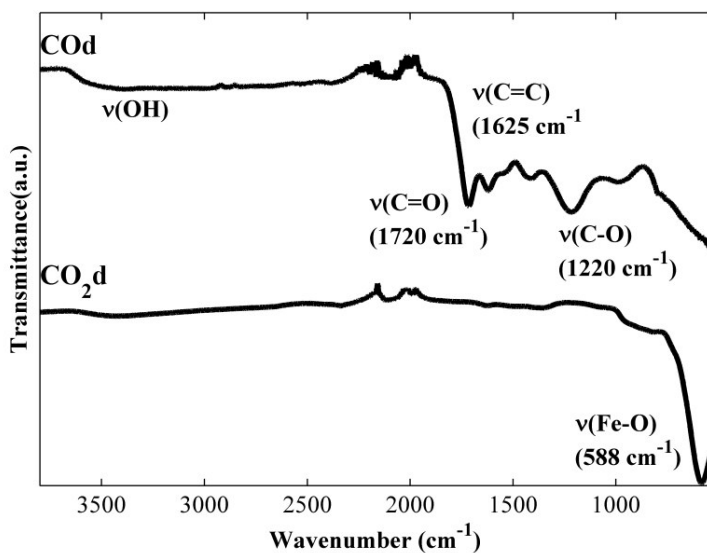


**Figure 4-8.** FTIR spectra of the CO<sub>d</sub> and CO<sub>2</sub>d samples, formed at 600 W and 1 SLM (9.1 eV/molecule).

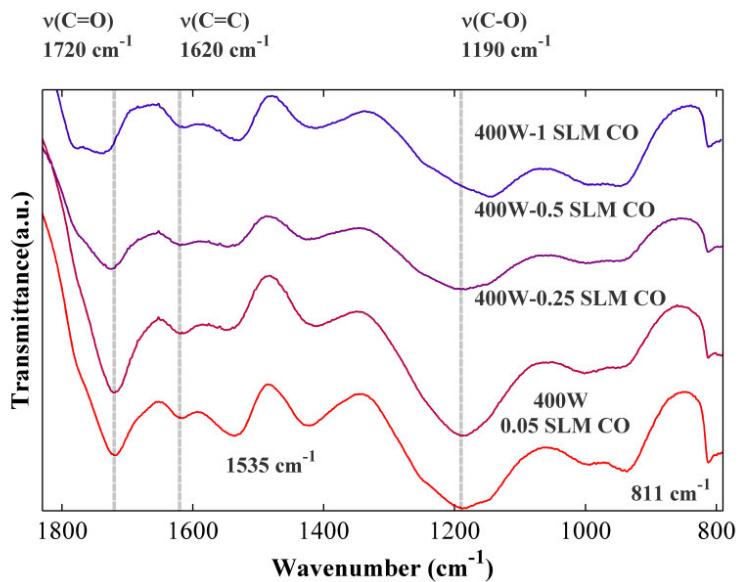


**Figure 4-9.** FTIR spectra of the CO<sub>d</sub> sample, formed at 400 W and various gas flow rates.

The presence of various carbon-oxide and carbon-carbon bonds can be related to the random polymeric network generated in the CO discharge. The product of the plasma<sup>[148]</sup> and pressure-induced<sup>[160]</sup> solidification of CO is referred as polymerized CO (p-CO). In these papers p-CO is compared to a carbon suboxide polymer (C<sub>3</sub>O<sub>2</sub>) via observing one or more of the fundamental C<sub>3</sub>O<sub>2</sub> absorption peaks (near 1511 cm<sup>-1</sup>, 1365 cm<sup>-1</sup>, 806 cm<sup>-1</sup>) in the FTIR spectra. In the same way, we can highlight the 1535 cm<sup>-1</sup> and 811 cm<sup>-1</sup> peaks in **Figure 4-9**, indicating the similarity of COd to a C<sub>3</sub>O<sub>2</sub> polymer.

A similar blue shift of the C=O peak as illustrated in **Figure 4-9** upon different gas flow rates is also observed for pressure-induced p-CO, when the solid deposits are exposed to a 100°C atmosphere.<sup>[161]</sup> In this article the peak shift is attributed to degradation of the polymer structure and increased disorder. Moreover, a further temperature increase up to 200 °C resulted in disappearance of the C=O peak, which is explained by a loss of oxygen and the formation of a purely graphitic structure. Somewhat similar can be observed here as well, as the SEI increase will inevitably result in a gas temperature rise (was not monitored in the current experiment). In our study, a variation of the SEI in the range between 6 and 120 eV/molecule does not drastically distort the FTIR spectrum of the COd sample (in contrast to observations in literature<sup>[161]</sup>) even at the highest energy input used, however the discussed modification of the COd structure can still be noticed on **Figure 4-9**. This suggests that our experiments does not yield a significant degradation of the polymer structure upon increasing SEI. Moreover, very similar spectra are found in the work of Lipp et al. and Geiger et al.<sup>[148, 160]</sup> Interestingly, the CO polymer structure presented by Lipp was prepared by pressure-induced polymerization, while Geiger utilized a DBD plasma system with a SEI of 0.1-1.5 eV/molecule. The modifications of the FTIR spectra with the SEI increase might indicate that there is an opportunity to control the properties of the produced polymeric structure but also potentially induce variation of the C/O ratio in the deposits. However, the *ex-situ* analysis of the COd properties is rather limited due to the fact that the polymer is unstable in the air.<sup>[161]</sup> To compliment this study, an

experiment involving *in-situ* surface diagnostic (for instance, *in-situ* FTIR) can provide an information regarding the polymer properties before the atmospheric exposure.

We can conclude that in the broad SEI range investigated, the CO discharge yields the deposition of a polymer-like (p-CO) structure, composed of conjugated C=O, C=C and C-O groups. For the CO<sub>2</sub>d sample, on the other hand, FTIR does not provide much information due to the largely inorganic structure.

## (b) Raman spectroscopy

Raman spectroscopy is used to differentiate between different phases of the deposited materials. The Raman spectrum of the COd sample (cf. **Figure 4-10, a**) contains a pronounced G-band ( $1560\text{ cm}^{-1}$ ) which is characteristic for graphitic carbon structures.<sup>[162]</sup> The D-band ( $1360\text{ cm}^{-1}$ ) corresponds to disordered structures and is not so intensive ( $I_D/I_G \sim 0.3$ ), while largely overlapping with the  $1425\text{ cm}^{-1}$  peak. This is a somewhat contradictory interpretation in literature, where it can be attributed both to the amorphous and crystalline structure.<sup>[163]</sup>

The presence of the similar G and D bands in the spectrum of the CO<sub>2</sub>d sample (cf. **Figure 4-10, b**) confirms the presence of the C=C and C-O carbon bonds, which are only partially visible in the FTIR spectrum. The large peak at  $690\text{ cm}^{-1}$  can be attributed to the Fe<sub>3</sub>O<sub>4</sub> structure.<sup>[164]</sup>

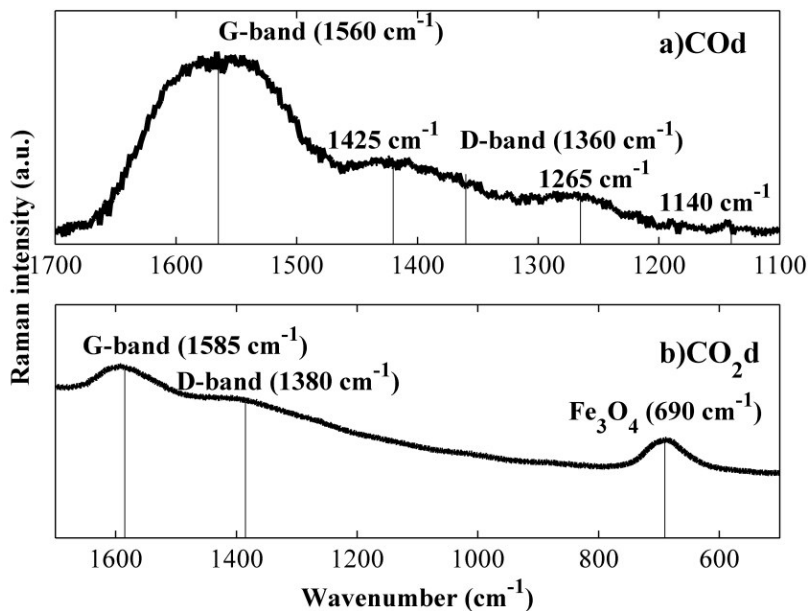


**Figure 4-10.** Raman spectra of the COd and CO<sub>2</sub>d samples, formed at 600 W and 1 SLM (9.1 eV/molecule).

**(c) XRD**

By means of X-ray Diffraction the inner surface of solid materials can be probed and a distinction can be made between amorphous and crystalline phases. The assumption that the COd sample would be amorphous is supported by largely-continuum spectra demonstrated on **Figure 4-11**. However, small peaks that can be attributed to graphitic planes (001) and (002) are spotted around 19° and 28°, respectively.

The XRD spectrum of the CO<sub>2</sub>d sample is composed of multiple magnetite (Fe<sub>3</sub>O<sub>4</sub> iron oxide) peaks, while smaller Fe (metallic iron) lines can be found as well. The measurements confirm the assignment of Fe-O and Fe<sub>3</sub>O<sub>4</sub> peaks, which are observed in the FTIR and Raman spectra, respectively.

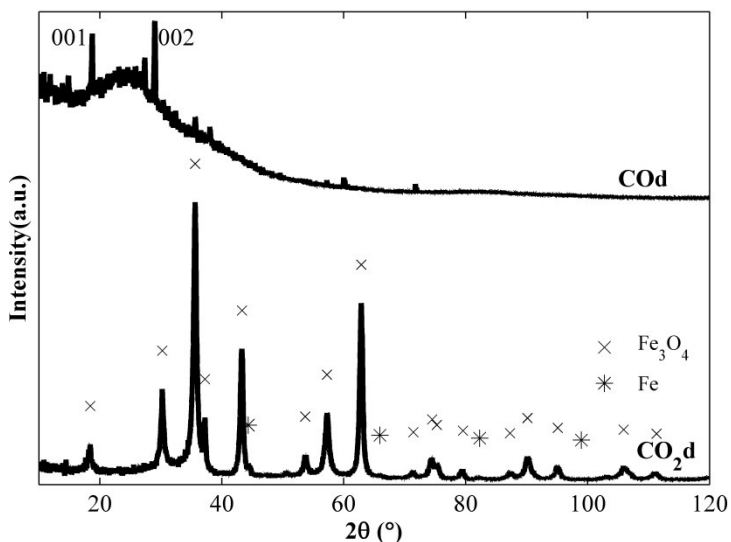


**Figure 4-11.** XRD spectra of the COd and CO<sub>2</sub>d samples, formed at 6000 W and 1 SLM (9.1 eV/molecule).

**Table 4-2** summarizes the properties of the COd and CO<sub>2</sub>d samples, as well as the discharge properties, i.e., emission characteristics and gas composition in the CO and CO<sub>2</sub> plasma, at 600 W input power and 1 SLM gas flow rate. In the next section, we will try to link both, with the aim to explain the underlying mechanisms of the synthesis of both types of materials.

**Table 4-2.** Summary of the properties of the COd and CO<sub>2</sub>d samples obtained in the CO and CO<sub>2</sub> DBD plasmas, respectively, as well as the optical emission characteristics and gas composition in both plasmas, measured with GC, at 600 W input power and 1 SLM gas flow rate, corresponding to a SEI of 9.1 eV/molecule.

Material characterization	COd	CO <sub>2</sub> d
Production rate [mg/min]	ca. 15	ca. 0.15
EDX, atomic conc. %	C/O 73% / 27%	Fe/O/C 13%/50%/30%
XPS, atomic conc. %	C/O 63% / 37%	Fe/O/C/ 16%/60%/15%
FTIR	C=C,C=O,C-O	Fe-O, C=C, C-O
XRD	Amorphous phase, 001,002	Fe <sub>3</sub> O <sub>4</sub> , Fe
Raman	I <sub>D</sub> /I <sub>G</sub> ~0.3	Fe <sub>3</sub> O <sub>4</sub> , G-,D- bands
<b>Discharge properties</b>	<b>CO</b>	<b>CO<sub>2</sub></b>
OES	C <sub>2</sub> (Swan), CO(A), CO(3B), CO <sub>2</sub> (Fox)	CO(A), CO <sub>2</sub> (Fox), CO(3B), Fe lines
GC	CO(98.8%), CO <sub>2</sub> (1.2%)	CO <sub>2</sub> (79.8%), CO(13.8%), O <sub>2</sub> (6.4%)

## 4-7 Discussion

### 4-7-1 CO discharge and COd sample

The CO DBD exhibits a very pronounced growth of solid deposits, in contrast to the CO<sub>2</sub> discharge. CO polymerization in a pressure-induced process is considered to be governed by the disproportionation reaction (Reaction 4-2 above).<sup>[160, 161]</sup> The same rationale can also be used for the CO discharge in the present study: a) the activation energy of Reaction 4-2 is significantly lower than the C-O bond energy (5.5 eV vs 11 eV, respectively); b) no O<sub>2</sub> is found in the exhaust, which would have been the case if there

would be significant CO dissociation in the plasma; c) the FTIR spectrum of the COd sample is very similar to that of p-CO as obtained by Lipp;<sup>[160, 161]</sup> d) the polymeric and mostly amorphous nature of the COd sample is confirmed in our study by different characterization techniques, including FTIR, XRD and Raman Spectroscopy. The CO disproportionation reaction might be followed by the Reactions 4-11, 4-12, 4-13, accompanied by the formation of C<sub>2</sub>O radicals and the further long polymer network growth.

To gain a better understanding of the ongoing processes, we reflect on the effect of specific energy input (SEI) variation on the properties of the discharge and the formed material. First, the larger amount of CO<sub>2</sub> produced in the CO plasma at higher SEI reflects the growing importance of the disproportionation reaction, because it is considered as the main source of the produced CO<sub>2</sub> (Reaction 4-2). Second, the drop of the C<sub>2</sub> Swan emission band relative intensity upon lower flow rate and thus higher SEI (cf. **Figure 4-4**) might indicate that less C<sub>2</sub> radicals are formed. Third, the SEM images and FTIR spectra (cf. **Figure 4-5**, **Figure 4-6**, **Figure 4-9**) demonstrate only a slight modification of the chemical structure and morphology upon increasing SEI, and thus no significant degradation of the polymer structure. Thus the higher energy input might be used to maximize the deposit formation in CO discharges without complete graphitization of the solid products (judging upon the FTIR measurements presented in **Figure 4-9**). This observation is supported by the fact that the solid products obtained in the work of Geiger and Staack, synthesized with a CO plasma at 40-60 times lower power input (10 W vs 400-600 W at similar gas flow rates) resulted in rather similar FTIR spectra. Interestingly, the reported growth rates and the formed CO<sub>2</sub> concentrations are one-two orders of magnitude lower as well (cf. **Table 4-3**). Some difference in elemental composition of the solid deposits can be noticed in **Table 4-3**, which might be attributed to the high sensitivity of the p-CO to atmospheric exposure, giving rise to some chemical structure modification over time.<sup>[165]</sup> Besides, different measurement techniques are applied, and hydrogen cannot be measured with XPS, which is used in our study.

Mori demonstrated that oxygen or hydrogen admixtures (0.1-1%) to a CO discharge result in solid deposits with a strongly different morphology and crystallinity and can even suppress the formation of the deposits.<sup>[142-144, 146]</sup> In our work it is shown that a higher energy input results in a higher concentration of CO<sub>2</sub> in the reactor outlet gas (up to 6.2%, cf. **Table 4-3**), which may also act as amorphous phase etchant.<sup>[166]</sup> This might limit the production rate and explain the slight distortion in the structure morphology resulting from a higher SEI in CO discharge (cf. **Figure 4-5** and **Figure 4-6**). However, a detailed study of the effect of energy input on crystallinity or C:O ratio is beyond the scope of this Chapter and might be studied along with the influence of admixtures on the atmospheric pressure CO DBD and its solid products. It is also interesting to note the similarity of the structure achieved in the CO DBD to a C<sub>3</sub>O<sub>2</sub> polymer, known to have various applications in the chemical industry.<sup>[167]</sup>

**Table 4-3.** Difference between the solid materials deposited in our CO DBD and the materials produced in the CO DBD by Geiger and Staack<sup>[148]</sup>

Parameter	This work	Ref. <sup>[148]</sup>
Input power [W]	600	10
CO flow rate [SLM]	1	0.1-1
SEI [eV/molec.]	9.1	1.5-0.1
CO <sub>2</sub> produced [mol. %]	1.2%	<0.1%
Growth rate [mg/min]	ca. 15	0.16-0.20
Elemental composition,	C/O	C/H/O
atomic conc. %	63%/ 37% (XPS)	36%/ 31%/ 33% (pyrolysis)

#### 4-7-2 CO<sub>2</sub> discharge and CO<sub>2</sub>d sample

As noted before, the deposition of solid products in the CO<sub>2</sub> DBD is limited and very few analyses are available in literature. The suppression of the formation of solid

carbon structures might be explained in different ways: a) Reactions 4-8, 4-9 in the oxygen-rich plasma efficiently quench C and C<sub>2</sub>O, which are precursors for the formation of solid carbon C<sub>s</sub> and polymerized CO; b) the excited CO<sub>2</sub> molecules and their dissociation products can actively gasify and thus etch the deposited carbon according to Reaction 4-10. The latter property of CO<sub>2</sub> plasmas was demonstrated for catalyst de-coking<sup>[107]</sup> and carbon nanotube purification and functionalization.<sup>[166, 168]</sup> In contrast to the CO discharge, the CO<sub>2</sub> plasma yields a two orders of magnitude lower deposition rate, indicating indeed that the occurring processes are different.

It is interesting to note that in our study the deposited coating of the CO<sub>2</sub> discharge contains both carbonaceous and inorganic compounds. The latter (together with the presence of the Fe lines in the optical emission spectrum, cf. **Figure 4-3, a** and **c**) gives direct evidence for the fact that etching takes place on the metal electrode surface, producing nanopowders. Gushin also demonstrated the formation of nanopowders of various materials in an atmospheric pressure CO<sub>2</sub> plasma, albeit for a microwave (MW) plasma torch<sup>[169]</sup>. The formation of a product somewhat similar to the CO<sub>2</sub>d sample is obtained when an iron electrode is used. However, in contrast to our study, no carbon content is found. Moreover, the crystalline phases are determined to be Fe<sub>2</sub>O<sub>3</sub> and FeO, while Fe<sub>3</sub>O<sub>4</sub> and Fe are detected in our case. **Table 4-4** summarizes the different plasma conditions and sample characteristics for our study, compared to the work of Gushin<sup>[169]</sup>, as well as compared to the work of Borra et al.<sup>[170]</sup> where also nanopowders (or nanoparticles) were produced, albeit for a N<sub>2</sub> DBD.

**Table 4-4.** Comparison between the production of the CO<sub>2</sub>d sample in this work and the reported NP production by Gushin<sup>[169]</sup> and Borra et al.<sup>[170]</sup>

Parameter	This work	Gushin <sup>[169]</sup>	Borra et al. <sup>[170]</sup>
Type of plasma	DBD	MW	DBD
Input power [W]	600	400	1-10
Flow rate [SLM]	1, CO <sub>2</sub>	5, CO <sub>2</sub>	1-10, N <sub>2</sub>
SEI [eV/molec.]	9.1	1.2	0.02..0.15
CO <sub>2</sub> conversion [%]	19.2	ca. 5	-
Production rate [mg/min]	0.15 (collected powder)	0.025 (measured electrode erosion)	10-300*10 <sup>-6</sup>
Elemental composition, atomic conc. %	Fe/O/C 13%/50%/30% (EDS)	Fe/O 57%/43% (EDS)	Metallic NPs
Crystalline phases	Fe <sub>3</sub> O <sub>4</sub> , Fe	Fe <sub>2</sub> O <sub>3</sub> , FeO	-
Particle size [nm]	10..300	50..60	1..10

The production of nanoparticles due to etching of the electrode is a known property of non-thermal plasmas.<sup>[170-172]</sup> Interestingly, the characteristic size of the metallic NPs, produced in a N<sub>2</sub> DBD is somewhat smaller (1...10 nm)<sup>[170]</sup> than of the NPs obtained in our study (see **Table 4-4**). It is known that the size of the produced NPs is controlled by the energy delivered to the electrode surface via a single microdischarge<sup>[170, 171]</sup>. Thus, the increase in particle size might be explained by the higher energy of the microdischarges occurring in oxygen-containing atmospheres<sup>[108, 173, 174]</sup>. In the work of Borra *et al.*<sup>[170]</sup>, the energy per filament was calculated to be 10-100 μJ for 50 mA current pulses in N<sub>2</sub> atmosphere. We can roughly estimate that the energy per microdischarge would be 200-500 μJ for the 100-1000 mA current pulses in our CO<sub>2</sub> discharge. This also explains why the input power variation has no or limited

effect on the CO<sub>2</sub>d sample properties: an increase of the applied voltage (and thus input power) results in a larger number of microdischarges, rather than in modification of their properties. Thus, a higher input power essentially increases the production rate of the solid product.

### 4-7-3 Can we produce carbon materials by means of atmospheric pressure CO<sub>2</sub> plasma?

The aim of this chapter is to answer the question whether CO and CO<sub>2</sub> discharges give rise to similar deposits at similar conditions. It is clear from the above that the answer is no. At high specific energy input (SEI), e.g., 120 eV/molecule, the CO discharge yields about 6.2 mol.% CO<sub>2</sub> in the reactor exhaust. In spite of this limited CO<sub>2</sub> production, these conditions are accompanied by a significant drop of the C<sub>2</sub> Swan intensity (cf. **Figure 4-4**) and a modification of the chemical structure (cf. **Figure 4-9**) of the polymeric solid product. At similar SEI values, the CO<sub>2</sub> DBD outlet contains 55% CO<sub>2</sub>, 30% CO and 15% O<sub>2</sub> (see **Table 4-1**). The CO<sub>2</sub> and O<sub>2</sub> molecules are known to be not only etchant agents in plasma,<sup>[166, 168, 175, 176]</sup> but they can also quench the C<sub>2</sub>O and C radicals (cf. Reactions 4-8, 4-9, 4-10) which are responsible for the formation of the carbon structure. This fact might be correlated with the absence of C<sub>2</sub> Swan bands in the optical emission spectrum of the CO<sub>2</sub> plasma. In general, this explains why the CO<sub>2</sub> discharge yields a much lower solid product formation, and with a different chemical structure than in the CO plasma, in spite of the fact that still a considerable amount of CO is formed.

Thus, it seems that in order to utilize the transformation CO<sub>2</sub> → CO → C(s) in a DBD, we have to extract the oxygen during the conversion process. For instance, the use of oxygen deficient ferrites in thermo-catalytic reactions allows the reduction of CO<sub>2</sub> to carbon.<sup>[177, 178]</sup> In this process the oxygen produced from CO<sub>2</sub> gets incorporated into the surface of the active ferrite. However, it was reported that excessive amounts of CO<sub>2</sub> might prevent carbon formation.<sup>[179]</sup> A similar concept of oxygen extraction was

reported already by Mori et al. for a CO<sub>2</sub> plasma, providing an interesting route to produce carbon structures in a CO<sub>2</sub> plasma, via the *in-situ* extraction of the oxygen.<sup>[127]</sup> This paper confirms the fact that oxygen is one of the inhibitors of carbon deposition in a CO<sub>2</sub> plasma. In addition, the formation of carbon deposits is often observed in plasma systems operating in CO<sub>2</sub>-CH<sub>4</sub> mixtures.<sup>[102, 124, 129, 180]</sup> The lower amount of carbonaceous product gasification (and thus etching) via oxygen species in a CO<sub>2</sub>-CH<sub>4</sub> atmosphere might be explained by trapping of the formed O<sub>2</sub> by the CH<sub>x</sub> radicals, as demonstrated by Aerts *et al.*<sup>[181]</sup> A similar effect can be expected by admixing H<sub>2</sub> in CO<sub>2</sub> discharges, as was also reported by Aerts *et al.*<sup>[181]</sup>

## 4-8 Conclusions

The question to be answered in this Chapter is whether CO and CO<sub>2</sub> discharges give rise to similar deposits at similar conditions and if not, what are the main differences between those plasmas (see Introduction). To answer this question, we analyse and compare CO and CO<sub>2</sub> DBD plasmas and their solid products. It is clear that substantial differences in the plasma composition result in the formation of deposits that are remarkably different. The CO DBD yields a two orders of magnitude higher deposition rate than the CO<sub>2</sub> discharge, indicating that the underlying processes are indeed different. The deposition in the CO plasma seems to be driven by the disproportionation reaction (i.e.,  $\text{CO} + \text{CO} \rightarrow \text{C} + \text{CO}_2$ ), as a significant amount of CO<sub>2</sub> (up to 6.2 mol. %), proportional to the specific energy input, is found in the reactor exhaust. The solid product is characterized as an amorphous carbonaceous (C/O=63%/37%) structure and identified as polymeric CO. The p-CO structure might potentially be close to a C<sub>3</sub>O<sub>2</sub> polymer, a valuable chemical product. The CO<sub>2</sub> discharge, on the other hand, does not produce this carbonaceous structure, in spite of the fact that considerable amounts of CO are produced. Indeed, the outlet mixture of the CO<sub>2</sub> discharge contains besides CO<sub>2</sub> also CO and O<sub>2</sub>. The Fe lines present in the OES spectrum, however, indicate that significant oxidation and etching takes place on the

surface of the metal electrode, which results in the formation of nanoparticles (Fe/O/C=16% /60% /15%, Fe<sub>3</sub>O<sub>4</sub>) in the microdischarges and as deposits on the reactor walls. At the same time, the formation of the amorphous carbonaceous structure close to polymeric CO is suppressed, due to etching by the CO<sub>2</sub> and O<sub>2</sub> molecules, and because the latter also quench the C and C<sub>2</sub>O radicals, which are the precursors for this carbonaceous structure. Thus, we believe that in order to produce such a carbonaceous structure from a DBD in CO<sub>2</sub> (i.e., through the transformation CO<sub>2</sub> → CO → C(s)), the O<sub>2</sub> produced by CO<sub>2</sub> splitting should be extracted during the conversion process.

# Chapter 5

## Pressure as a control handle for atmospheric plasma processes

---

In plasma-based ozone generation and some other plasmachemical processes the pressure is often raised above the atmospheric level to improve the energy efficiency of the reaction. In order to explore the influence of a pressure increase for stimulating CO<sub>2</sub> dissociation, a DBD operating in CO<sub>2</sub> is studied at elevated pressure (1-3.5 bar). Furthermore, a DBD operating in O<sub>2</sub> above atmospheric pressure is also presented to better illustrate the effect of metal electrode evaporation in oxygen-containing DBDs. It is demonstrated that these operational conditions significantly influence both the discharge dynamics and the process efficiencies of O<sub>2</sub> and CO<sub>2</sub> discharges. For the case of the O<sub>2</sub> DBD, the pressure rise results in the amplification of the discharge current, the appearance of emission lines of the metal electrode material (Fe, Cr, Ni) in the optical emission spectrum and the formation of a granular film of the erosion products (10-300 nm iron oxide nanoparticles) on the reactor walls. Somewhat similar behaviour is observed also for the CO<sub>2</sub> DBD. The discharge current, the relative intensity of the CO Angstrom band measured by Optical Emission Spectroscopy (OES) and the CO<sub>2</sub> conversion could be stimulated to some extent by the rise in pressure. The optimal conditions for the O<sub>2</sub> DBD (2 bar) and the CO<sub>2</sub> DBD (1.5 bar) are demonstrated. It could be concluded that the pressure increase stimulates the formation of more intensive but fewer microdischarges. In this way, the operating pressure can represent an additional tool to manipulate the properties of the microdischarges in a DBD, and as a result also the discharge performance.

---

This chapter has been published online as: I. Belov; S. Paulussen; A. Bogaerts, Pressure as an additional control handle for non-thermal atmospheric plasma processes. *Plasma Processes and Polymers* 2017 **14** e1700046

## 5-1 Introduction

Plasma reactors are used for a wide range of processes including gas conversion, material synthesis and surface treatment. The promising technological and economical aspects of non-thermal atmospheric pressure technology in these areas have recently gained a lot of interest<sup>[14, 22, 25, 182, 183]</sup>. However, the control and tuning of Atmospheric Pressure Plasma (APP) systems is not trivial. The plasma chemistry is often governed by plasma parameters which cannot be directly determined by the external settings. For instance, in the specific case of DBD reactors, the plasma is composed of numerous filaments which are known to define the plasma chemistry.<sup>[28]</sup> The number of these filaments and their properties can, however, not be controlled externally, for instance by the applied voltage.<sup>[29]</sup> Usually the power input, gas mixture, flow rate, reactor geometry and excitation type are the parameters used for APP process tuning.<sup>[15, 41]</sup> The power input is considered the main variable that determines the efficiency of the gas conversion.<sup>[15, 41]</sup> In the case of material synthesis applications of APPs, it was reported that the gas flow often influences the production rate<sup>[170, 184, 185]</sup> and even the morphology of the synthesized product.<sup>[186-188]</sup> Yet, a better understanding of the underlying principles and dependences is necessary to design an efficient and optimized process.

In this Chapter, the effect of pressure, and more in particular overpressure, on the material synthesis process in an O<sub>2</sub> DBD, and on the conversion reactions in a CO<sub>2</sub> DBD, is being studied. Typically, discharge gaps between 0.5 and 3 mm and flow rates in the range of 0.1 to 10 Standard Liter per Minute (SLM) are applied in laboratory scale APP reactors. Besides, analysis systems such as Gas Chromatographs (GC), Scanning Mobility Particle Sizers (SMPS), Condensation Particle Counters (CPS) or collection filters are often installed in-line with the discharge. Simple engineering estimations suggest that the pressure drop can reach 0.1 to 4 bar for systems operated at flow rates between 0.1 and 10 SLM. Yet, this phenomenon is not addressed in literature and this type of conditions is referred to as “atmospheric”. Often gas flow

levels are identified as controlling parameters, but perhaps the increasing pressure drop at increasing gas flows is the actual underlying reason for the differences that can be observed. In this work, we want to assess the impact of increasing pressure on the outcome of APP processes.

The effect of pressure variations between 1 and 3 bar on process efficiency was mainly studied for the ozone production<sup>[74, 189-192]</sup> – the most industrialized application of DBD reactors.<sup>[20]</sup> In recent works, Yuan *et al.* and Seok *et al.* demonstrated the existence of an optimal pressure for the ozone synthesis at 1.4 bar for air-fed<sup>[74]</sup> and 1.5-2 bar for oxygen-fed<sup>[192]</sup> systems. Furthermore, studies on nanosecond pulsed Surface Dielectric Barrier Discharge (SDBD) development at pressures between 1 and 6 bar in air give evidence for changing discharge dynamics with increasing pressure.<sup>[193, 194]</sup> It was also demonstrated that overpressure can influence plasma-assisted ignition systems<sup>[195]</sup> as well as the vibrational distribution function in pure N<sub>2</sub> discharges.<sup>[196]</sup>

As shown above, a pressure increase can be used to improve the efficiency of a number of plasmachemical processes. It is interesting to explore whether the pressure can also stimulate the CO<sub>2</sub> conversion in a DBD. In this Chapter, the influence of the operating pressure will be investigated for DBD systems operating in CO<sub>2</sub> and O<sub>2</sub> at pressures between 1 and 3.5 bar. Here the O<sub>2</sub> DBD it is also studied to better illustrate the effect of a metal electrode evaporation, which is demonstrated in the previous chapter. Thus the DBD operating with pure O<sub>2</sub> will be used to deposit iron oxide nanoparticles on the reactor walls through etching of the central electrode, while the deposition rate of the nanopowder is measured. In case of the CO<sub>2</sub> DBD, the efficiency of CO<sub>2</sub> dissociation is evaluated upon pressure rise. In both cases the effect of the pressure increase on the discharge behavior and on their performance indicators is evaluated.

## 5-2 System description

The experimental setup of the Dielectric Barrier Discharge configuration under investigation is schematically shown in **Figure 2-2**. The key point of the given design is the opportunity to control the pressure and to collect the produced nanopowder on the membrane filter placed downstream the reactor in case of the O<sub>2</sub> DBD.

### 5-2-1 Deposition experiment

In the previous Chapter we demonstrated that the DBD operating in oxygen-containing plasmas gives rise to strong erosion of the metal electrode surface and redeposition of the etched material in the form of a granular metal oxide nanoparticle film on the reactor walls.<sup>[197]</sup> In the current Chapter, we study the effect of the operating pressure on the deposit production. The material is collected from the inner surface of the dielectric tube (where it is mostly deposited) in the form of a nanopowder and weighted. The production rate is evaluated via dividing this value by the reaction time (120 minutes). An O<sub>2</sub> flow rate of 1 SLM and a discharge power of 650W (corresponding to 9.89 eV/molec. specific energy input) are applied in this set of experiments.

### 5-2-2 Conversion experiment

The CO<sub>2</sub> conversion obtained at pressures between 1 and 2.5 bar is measured while keeping the power input constant, to demonstrate the influence of the operating pressure on the process efficiency. A CO<sub>2</sub> flow rate of 0.5 SLM and a discharge power of 650W (corresponding to 19.78 eV/molec. specific energy input) are applied in this set of experiments.

## 5-3 Results

### 5-3-1 O<sub>2</sub> DBD and its production rate of nanopowder

The effect of pressure elevation on the oxygen discharge can be associated with a modification of the current waveform, as demonstrated in **Figure 5-1**. An increase of the discharge current in the positive half-cycle (HC) can be clearly distinguished. An asymmetric current waveform of the O<sub>2</sub> DBD with respect to the positive and negative HCs of the applied voltage (described in our previous works<sup>[173, 197]</sup>) can be observed in the whole pressure range investigated (1 - 3.5 bar).

The dynamics of the discharge current in the positive half-cycle of the O<sub>2</sub> DBD upon increasing pressure is presented in **Figure 5-1**. Here we introduce the *Average Current Maximum* (ACM) value. This is the mean amplitude of the current pulse that is calculated via subtracting the sinusoidal component from the measured current waveform of 10 subsequent cycles, while the error bars here indicate the deviation of the maximum current peak amplitude. In this way, one can derive the rise of the ACM associated with the pressure increase. Interestingly, the maximum of this value is observed at around 2 bar. A further pressure increase results in the drop of the ACM value. The broad error bars in **Figure 5-2** (especially at p~2 bar) indicate the increase of the presence of the high amplitude pulses (cf. also **Figure 5-1**) in the discharge current. In addition to that, visual inspection of the O<sub>2</sub> DBD (cf. **Figure 5-3**) suggests that more sparse and bright filaments are observed in the O<sub>2</sub> DBD at higher pressure. An O<sub>2</sub> flow rate of 1 SLM and a discharge power of 650W (corresponding to 9.89 eV/molec. specific energy input) are applied in this set of experiments.

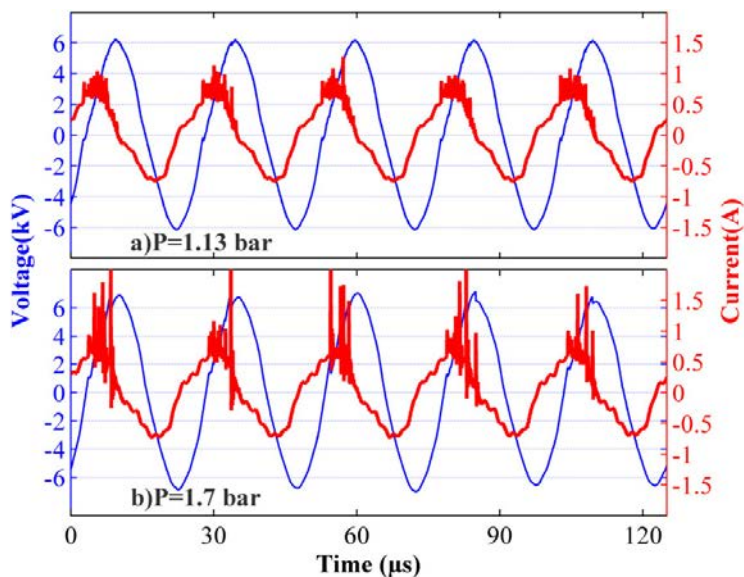


**Figure 5-1.** Electrical signal of the O<sub>2</sub> DBD at (a) 1.13 and (b) 1.7 bar pressure; Discharge power: 650 W; gas flow rate: 1 SLM

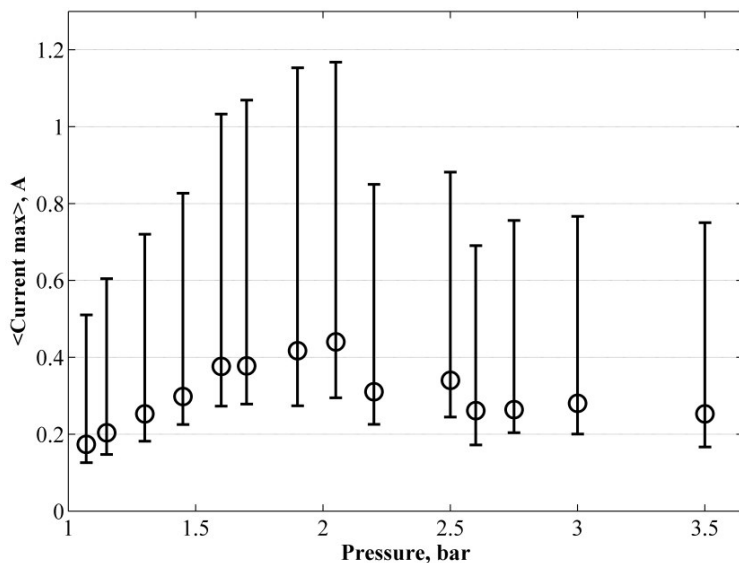


**Figure 5-2.** Discharge current, represented by the average current pulse (ACM), in the positive HC of the O<sub>2</sub> DBD upon increasing pressure.

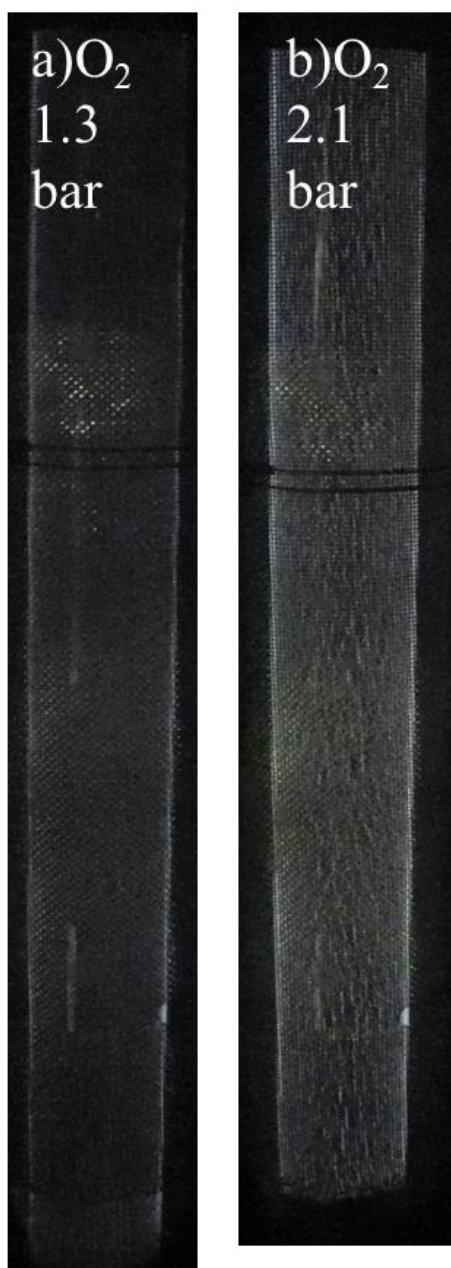


**Figure 5-3.** Images of 1 SLM O<sub>2</sub> DBD (exposure time 1/25 sec.) at a) p=1.3 bar, b) p=2.1 bar.

Another effect of the pressure elevation can be noted via Optical Emission Spectroscopy (OES). The O<sub>2</sub> DBD emission spectrum normalized at 459.2 nm (maximum of the continuum component in the range 300-650 nm) is presented in **Figure 5-4**. The emission lines of the central stainless steel electrode material (Fe, Cr, Ni in the range 340-440 nm) are not observed below  $p=1.45$  bar, but they are becoming brighter with a further pressure increase above 1.45 bar. That effect is also demonstrated in **Figure 5-5**, where the relative intensity of the 358.1 nm line (the brightest Fe line in the measured spectrum) grows with increasing pressure.

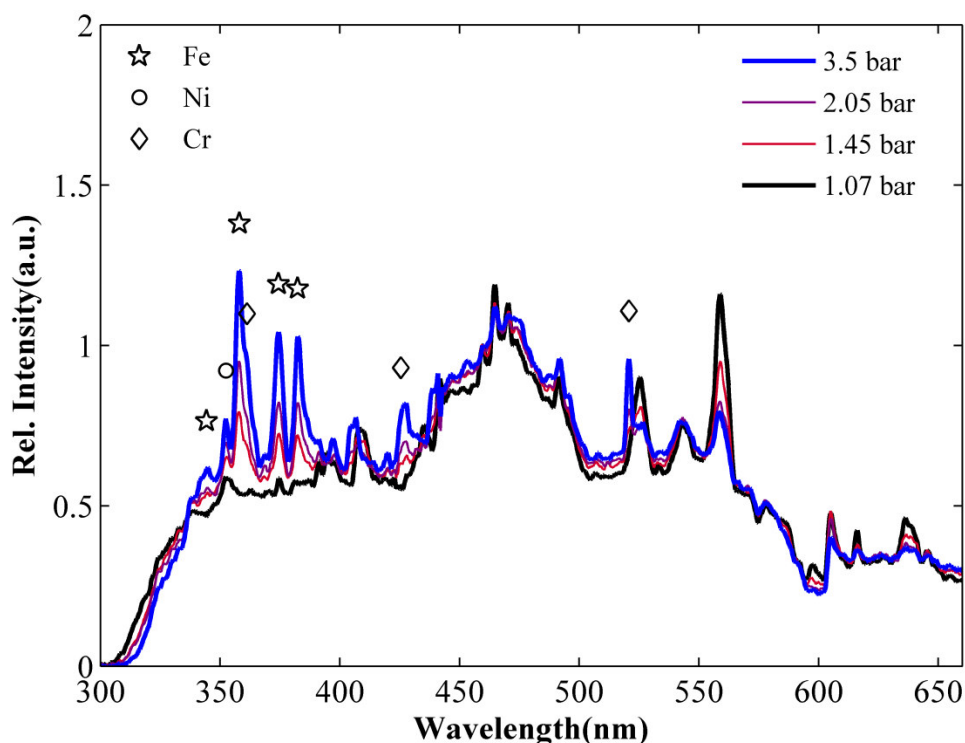


**Figure 5-4.** Optical signals of the O<sub>2</sub> DBD at various pressures normalized at 459.2 nm.

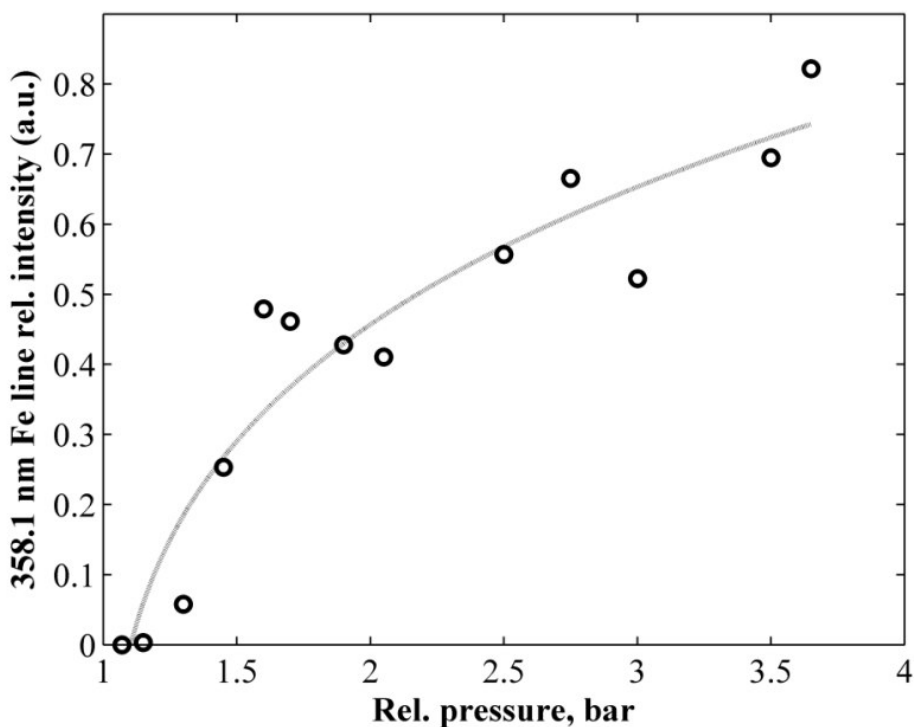


**Figure 5-5.** OES intensity of the 358.1 nm Fe line obtained in O<sub>2</sub> DBDs upon increasing pressure.

In **Chapter 4** it is reported that nanoparticles composed of Fe, O and C (with the trace presence of the other stainless steel alloy compounds) are formed in the O<sub>2</sub> and CO<sub>2</sub> DBDs, and that they are deposited on the reactor walls.<sup>[197]</sup> Here, we extend the analysis by the collection of powders through a membrane filter installed downstream of the reactor, in order to qualitatively evaluate the presence of particles guided by the gas flow in the exhaust. In **Figure 5-6** it is demonstrated that the amount of nanopowder collected from the reactor walls highly depends on the operating pressure. Interestingly, at near-atmospheric conditions ( $p=1.13$  and 1.3 bar) almost no particles are found on the reactor walls nor on the filter. The highest powder production rate is observed at a pressure of 1.9 bar, followed by a drop upon higher pressures. **Figure 5-6** also illustrates the qualitative correlation between the powder collected from the reactor walls and the deposits on the membrane filters. The higher

production rate corresponds to the thicker (i.e. darker) layer on the filter, while no deposition in the discharge zone results in clean (i.e. white) filter.

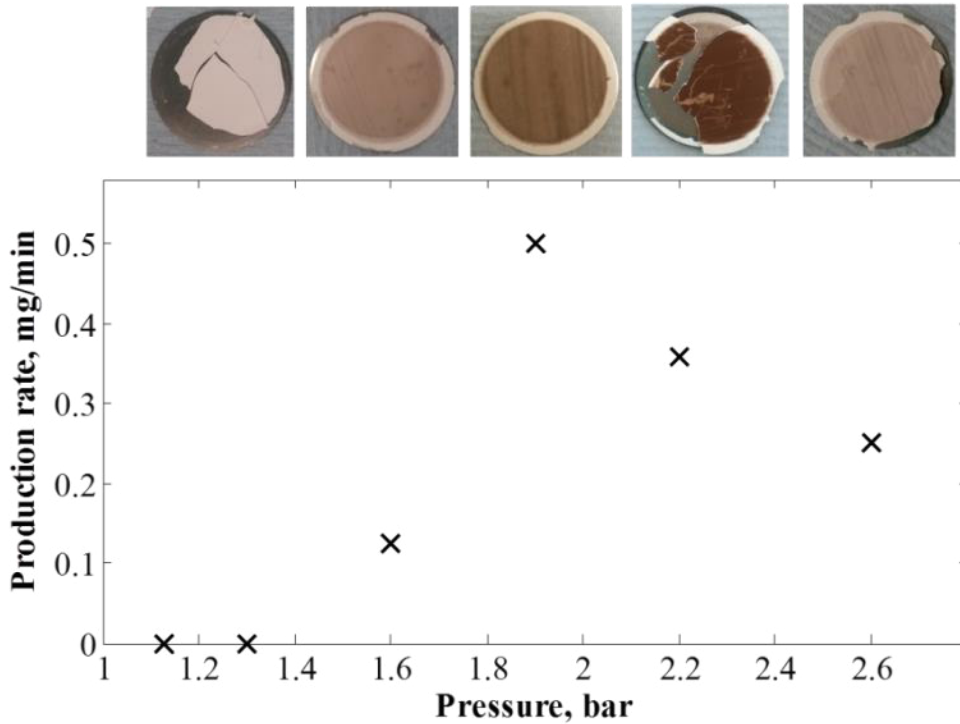


**Figure 5-6.** Production rate of nanopowder deposits on the reactor walls in the O<sub>2</sub> DBD, and pictures of the 0.22 μm membrane filters installed downstream the reactor after 2 hours of operation, at the corresponding pressure regimes.

A comparison between the ACM and the production rate of the coating is presented in **Figure 5-7**. Both parameters behave in a rather similar way upon increasing pressure with a maximum value being reached around 2 bar, followed by a decrease at higher pressures.

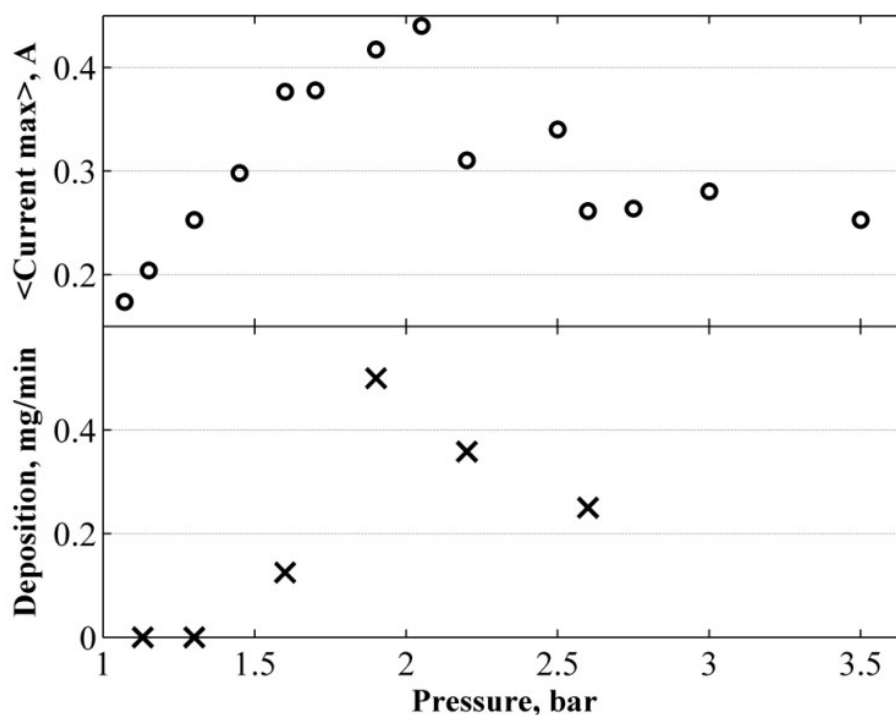


**Figure 5-7.** Average current pulse in the positive HC of the O<sub>2</sub> DBD (top) and production rate of the collected powder (bottom) as a function of pressure.

### 5-3-2 CO<sub>2</sub> DBD and its conversion

An increase of the operating pressure also gives rise to modification of a CO<sub>2</sub> DBD. Spectra of the CO<sub>2</sub> DBD, normalized at 337.1 nm (the brightest CO<sub>2</sub> line that has no large overlap with the CO lines), are shown in **Figure 5-8**. The emission spectrum of the filamentary CO<sub>2</sub> plasma consists of the highly overlapped Fox system CO<sub>2</sub>/CO<sub>2</sub><sup>+</sup> lines (CO<sub>2</sub>(Fox) in the figure) in the range of 300-420 nm, the CO 3<sup>rd</sup> positive band (280-360 nm), CO Angstrom bands (CO(A) in the figure) in the range between 450 and 700 nm, and a continuum part with a maximum at about 450 nm.<sup>[46, 101, 113, 114]</sup> Similarly to the O<sub>2</sub> DBD, the electrode material lines can be observed. Remarkably, an increasing pressure results in a rise of the relative intensity of the CO(A) lines, as can be seen in **Figure 5-8**.

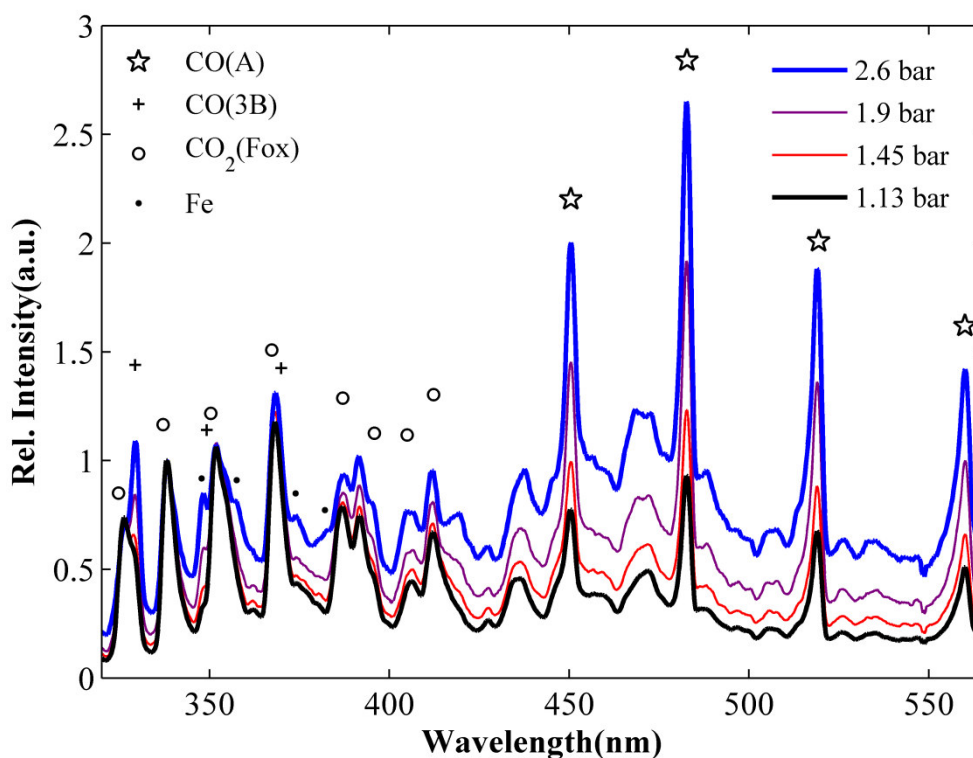


**Figure 5-8.** Measured optical signals (normalized at 337.1 nm) of the CO<sub>2</sub> DBD at various pressures.

Upon pressure rise, an analogous behavior of the increasing discharge current in the positive HC is observed and the current waveform transforms accordingly, similar to that of the O<sub>2</sub> DBD (cf. **Figure 5-1**). The ACM values of the CO<sub>2</sub> DBD also rise with increasing pressure, analogous to the O<sub>2</sub> DBD (compare **Figure 5-7** and **Figure 5-9**). However, further increasing the pressure above 2 bar results again in a drop of the mean current pulse amplitude. Visual inspection of the CO<sub>2</sub> discharges also suggests brighter and sparser filaments formed at higher pressures (cf. **Figure 5-10**). Interestingly, the CO<sub>2</sub> conversion peaks at a pressure of 1.5 bar, while a further increase of the pressure results in a drop of the conversion. As the discharge power is kept constant, the operation at 1.5 bar results in a higher energy efficiency of the process (4.8% at 1.5 bar vs 3.5% at atmospheric pressure, when compared to the standard enthalpy of the CO<sub>2</sub> decomposition Reaction, cf. 1-1).

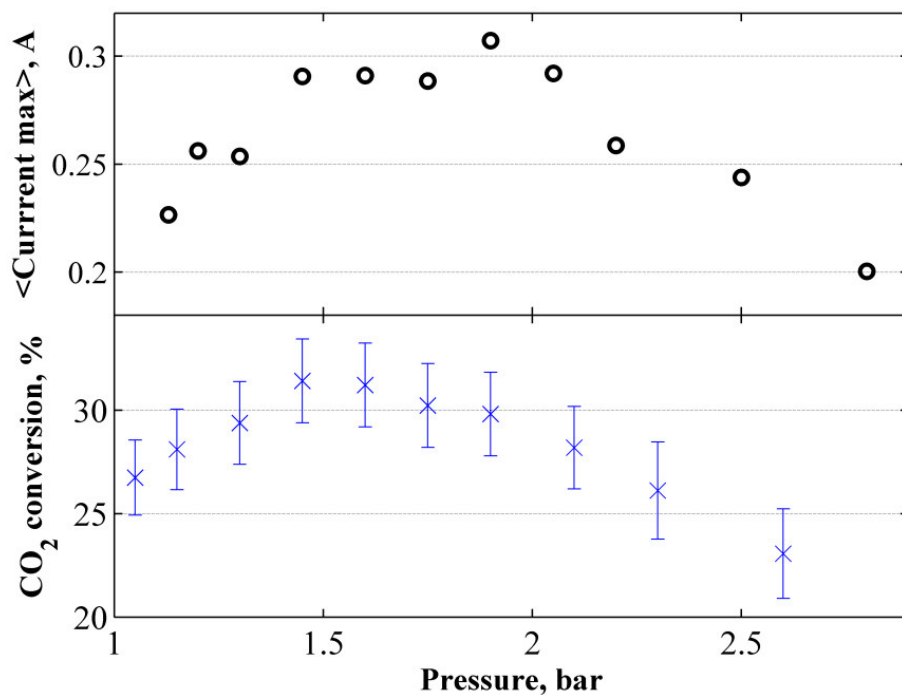


**Figure 5-9.** Average current pulse amplitude of the CO<sub>2</sub> DBD in the positive HC (top) and CO<sub>2</sub> conversion (bottom), as a function of pressure. Discharge power: 650 W; CO<sub>2</sub> flow rate: 0.5 SLM.

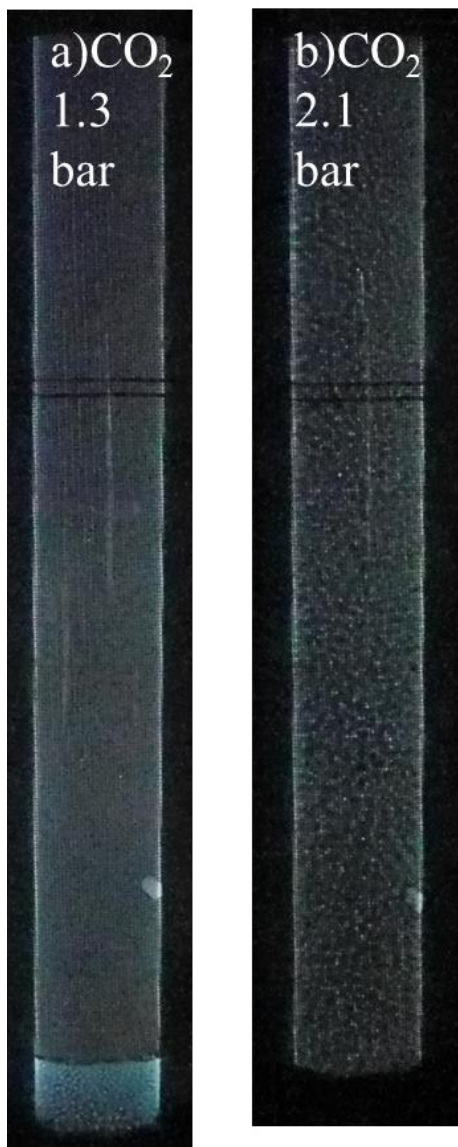


**Figure 5-10.** Images of 0.5 SLM CO<sub>2</sub> DBD (exposure time 1/25 sec.) at a) p=1.3 bar, b) p=2.1 bar.

## 5-4 Discussion

### 5-4-1 How can pressure stimulate the single microdischarge current in the O<sub>2</sub> and CO<sub>2</sub> DBDs?

Based on the results shown in the previous section, we can assume that a pressure increase induces a higher current through a single microdischarge ( $I_{MD}$ ), while the number of the microdischarges decreases at the same time. This statement can be supported by the following observations:

- i) The relative intensity of the metal electrode material lines (such as Fe, Cr and Ni) and CO(A) bands in the optical emission spectra of the O<sub>2</sub> and CO<sub>2</sub> DBDs, respectively, rises almost linearly with increasing pressure (cf. **Figure 5-4**, **Figure 5-8**);
- ii) Visual inspection of the O<sub>2</sub> and CO<sub>2</sub> DBDs suggests that sparser and brighter filaments are formed at higher pressure (cf. **Figure 5-3** and **Figure 5-10**);
- iii) The ACM value rises with increasing pressure, having a maximum around a pressure of 2 bar (cf. **Figure 5-2**, **Figure 5-9**(top)), which can be correlated with the decrease of the number of the microdischarges;

The process variations might be explained by the high electronegativity of O<sub>2</sub> and of the products of CO<sub>2</sub> dissociation, and by the decrease of the mean free path at elevated pressures. Because of the latter, the mean electron energy drops, while the number of collisions rises. Such conditions favor electron attachment processes (with low energy thresholds), while ionization reactions (with high energy threshold) become less frequent. This will in turn lead to volume depletion of the electrons and consequently to less frequent ignition of microdischarges. Thus, charge transfer would be realized through fewer channels, thereby increasing the current passing through a single microdischarge. This hypothesis is backed up by Audier *et al.*, who observed sparser and brighter filaments, tending to ignite repeatedly at the same locations (thus utilizing the strong channels of the extinguished filaments), when the oxygen content was increased in an N<sub>2</sub>-O<sub>2</sub> surface DBD.<sup>[108]</sup> Similarly Höft *et al.* associated higher

discharge current maxima, a larger microdischarge radius and longer ignition delays with higher O<sub>2</sub> concentrations in a single-filament DBD configuration.<sup>[174, 198]</sup>

The decrease of the ACM value towards higher pressure regimes ( $p > 2$  bar) might be attributed to the decrease of the overall number of the microdischarges. Indeed, due to the large discharge area, several filaments might be ignited at the same time, causing overlap in the current measurements. In this way, the ACM presents the integrated value of the microdischarge current and the number of microdischarges occurring simultaneously. Accordingly, initially (at  $p < 2$  bar) the increase of the current is accompanied with a minor drop in the number of microdischarges. A further pressure rise (at  $p > 2$  bar) will significantly decrease the number of filaments, while the current through a single microdischarge will presumably keep increasing. In this way, the increase of the ACM is followed by a drop after  $p \sim 2$  bar (cf. **Figure 5-2**, **Figure 5-7**, **Figure 5-9**). However, as it is stated before, precise information about the properties of the microdischarges cannot be obtained in our system, thus further investigation of the pressure influence on O<sub>2</sub> or CO<sub>2</sub> discharges should be carried out with a single filament DBD set-up.

#### 5-4-2 How can pressure stimulate deposition of nanopowder in the O<sub>2</sub> DBD?

The oxidation of the metal electrode in oxygen-containing DBDs was already reported elsewhere.<sup>[34, 173, 192, 197]</sup> Our initial observation regarding the nanoparticle production in O<sub>2</sub> and CO<sub>2</sub> DBD systems is that deposition rates increase at higher flow rates and in higher power regimes. For instance, we observed full coverage of the dielectric tube with powder deposits after 2-5 hours at a discharge power of 600W and with a 1 SLM CO<sub>2</sub> flow rate, while it took more than 10 hours to obtain the same effect at a CO<sub>2</sub> flow rate of 0.1 SLM.<sup>[173]</sup> However, as the pressure drop might be significantly different when varying the flow rate from 0.1 SLM to 1 SLM, the operating pressure (rather than flow rate) might be the parameter determining that process.

Based on the observations reported above, we depict our understanding of the deposition process in **Figure 5-11**. First, the microdischarges evaporate metal from the electrode surface due to the localization of the current transfer (and thus heat transfer) through a narrow ( $d \sim 100\text{-}1000 \mu\text{m}$ ) filament channel.<sup>[170]</sup> In this way the metal vapor is transferred to the gas phase, and thus Fe, Cr and Ni lines can be observed in the optical emission spectra. Nucleation, aggregation, agglomeration and subsequently an increase in particle size occurs in the microdischarges. As a result, nanoparticles ranging in size between 10 and 300 nm are deposited on the surface of the dielectric tube facing the discharge.<sup>[197]</sup> The deposition on the reactor walls might be attributed to thermophoretic forces ( $F_{th}$ ).<sup>[199]</sup> Due to thermophoresis, transfer of nanoparticles to the cooler regions can be induced and is guided by the temperature gradient inside the discharge gap,  $F_{th} \sim -\nabla T_{gas}$ .<sup>[200]</sup> In the set-ups shown in **Figure 2-2**, the dielectric tube is externally cooled ( $T_{cool} \sim 20^\circ\text{C}$ ), while the gas temperature in the DBD can be  $100\text{-}300^\circ\text{C}$  higher (not measured in our study, but taken from the literature).<sup>[133, 201]</sup> This temperature gradient could lead to the condensation of nanoparticles on the reactor walls and the formation of a granular film layer with a thickness of about  $10 \mu\text{m}$ .

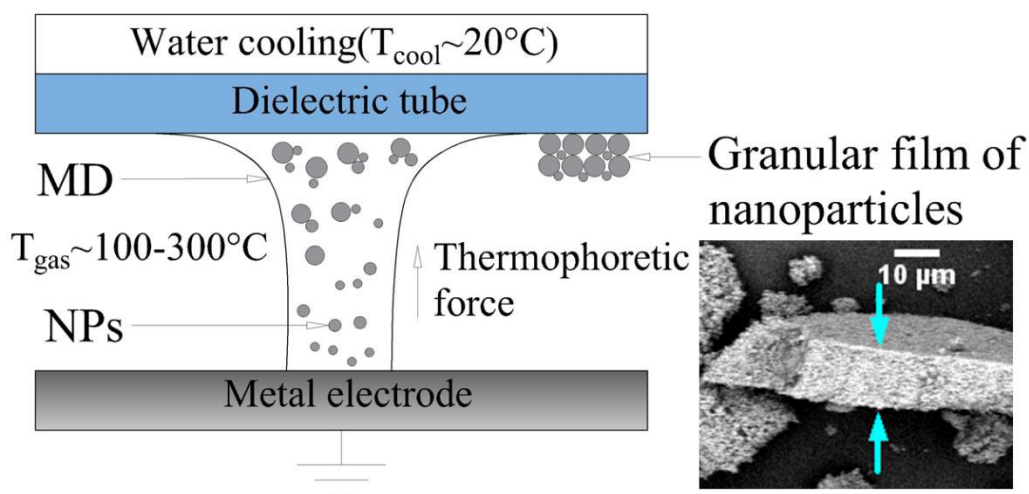


**Figure 5-11.** Scheme of the nanoparticle production process in an  $\text{O}_2/\text{CO}_2$  DBD, and SEM image showing the cross section of the granular deposit.

As can be seen in **Figure 5-6**, solid deposits are not found at pressures close to atmospheric ( $p=1.13$  bar,  $p=1.3$  bar). Comparing **Figure 5-4**, **Figure 5-5** and **Figure 5-6** one might conclude that evaporation only starts when the ACM reaches a value of approximately 0.25 A (at  $p>1.45$  bar). Indeed, at near-atmospheric conditions ( $p=1.13\dots 1.3$  bar) the particles are neither collected on the reactor walls nor on the downstream filter, while the emission lines of the electrode material (Fe, Cr, Ni) are not observed in the emission spectrum. It can be argued that with the modulation of pressure (and thus the microdischarge properties) one can control the power density delivered to the metal surface. As stated before, the change of the gas mixture and the operating pressure can influence the parameters of microdischarges, such as current pulse amplitude, duration and diameter.<sup>[174, 198]</sup> A threshold value of the power density delivered to the metal surface via charge transfer, needed for the electrode vaporization, might be assumed, that can be reached by increasing the microdischarge current via pressure elevation. For further insight in the process, we would require precise information regarding the single microdischarge, such as the discharge current amplitude, filament radius and pulse duration. Those parameters define the heat

transfer to the electrode surface, thus determining whether or not surface vaporization can occur.<sup>[202]</sup> These data might be collected in a single filament DBD reactor configuration<sup>[81, 174, 198]</sup> and can enable more accurate tuning of the process.

In a number of works, an eroded material from the electrodes in an APP system is deposited as a nanomaterial product, but most often only the influence of the flow rate is demonstrated.<sup>[170, 184-188]</sup> As stated before, 0.5-1.5 mm gaps or even capillary-sized tubes are commonly used in the discharge design, while the analysis systems are often installed downstream the reactor. Thus, flow variations in such conditions can result in a pressure drop that might also influence the discharge properties. The flow rate indeed plays a substantial role in the development of the material synthesis process, but the findings presented in this Chapter allow us to suggest that the pressure should also be considered as a control parameter. In this way, pressure regulation will present an additional tuning handle for developing an APP process.

### 5-4-3 How can a pressure increase stimulate CO<sub>2</sub> conversion?

The explanation for the facilitation of CO<sub>2</sub> conversion at increasing pressure is similar to the reasoning behind the increased powder deposition in O<sub>2</sub> discharges in similar regimes. The higher discharge current can be associated with a higher electron concentration ( $n_e \sim I_{MD}$ ), and thus with more frequent electron impact reactions, resulting in higher CO<sub>2</sub> decomposition rates. The observations that a higher discharge current is beneficial for the CO<sub>2</sub> conversion in a DBD were reported before.<sup>[31-35, 203]</sup> However, the maxima of the CO<sub>2</sub> dissociation rate and the mean discharge current values occur at different pressures, as observed in **Figure 5-9**. A higher pressure results in a rise of the microdischarge current, but also in a decrease of the number of microdischarges. Thus, the contact time of the CO<sub>2</sub> gas with the filaments will also drop, negatively affecting the conversion.<sup>[41]</sup> Another reason of the observed decrease of the dissociation rate might be that the CO<sub>2</sub> recombination becomes more prominent with increasing pressure.<sup>[204]</sup>

## 5-5 Conclusion

In this Chapter it is demonstrated that variations in the operating pressure between 1 and 3 bar have a prominent influence on the microdischarge behavior in O<sub>2</sub> and CO<sub>2</sub> Dielectric Barrier Discharges and consequently also on the efficiencies of these systems used for various processes. A change in the current waveforms, more specifically an amplification of the discharge current in the positive HC, is noted for both the O<sub>2</sub> and CO<sub>2</sub> DBDs. Furthermore, emission lines of the metal electrode material (Fe, Cr, Ni) appears in the spectrum of the O<sub>2</sub> DBD above p=1.45 bar and they become brighter with further pressure increase. Moreover, solid products in the O<sub>2</sub> DBD (i.e., a granular film of the iron oxide nanoparticles) are found only when the pressure is higher than 1.45 bar, while the growth rate has a maximum at p=1.9 bar.

For the CO<sub>2</sub> DBD, it is observed that the relative intensity of the CO(A) band in the emission spectrum is proportional to the pressure. The CO<sub>2</sub> conversion reaches a maximum value in the CO<sub>2</sub> discharge at p=1.5 bar. It is argued that the pressure increase again induces a rise of the discharge current through a single microdischarge and a simultaneous decrease in the number of filaments, thus defining the maximum efficiency of the APP processes.

We can conclude that pressure regulation in APPs might be seen as an additional control handle for the process. Not only it allows to tune the discharge current of the single microdischarge (and possibly the underlying plasma chemistry) but it also triggers additional effects, such as metal evaporation in the O<sub>2</sub> or CO<sub>2</sub> DBDs and the CO<sub>2</sub> conversion. These findings are of interest for material synthesis applications and plasma-based CO<sub>2</sub> conversion.

## Chapter 6

# Carbon Dioxide Dissociation in a Microwave Plasma Reactor

---

Microwave (MW) plasma systems represent a promising solution for efficient CO<sub>2</sub> dissociation. MW discharges are also very versatile and can be sustained at various pressure and gas flow regimes. To identify the most favorable conditions for the further scale-up of the CO<sub>2</sub> decomposition reaction, a MW plasma reactor operating in pure CO<sub>2</sub> in a wide pressure range (200 mbar - 1 bar) is studied. Three different gas flow configurations are explored: a direct, reverse and a vortex regime. It is demonstrated that the CO<sub>2</sub> conversion and energy efficiency drop almost linearly with increasing pressure, regardless of the gas flow regime. Thermalisation of the plasma, which can be observed via the rise in exhaust temperature, limits the performance of the MW discharge reactor in terms of conversion and energy efficiency at higher pressures. The results obtained here, as well as in the literature, suggest that MW plasma reactors operating at atmospheric pressure are probably the most viable for up-scaling, in spite of their somewhat limited performance in terms of conversion and energy efficiency, as no vacuum equipment is needed. From another point of view, the vortex configuration is the most promising, as it allows operation in a wider range of process parameters (flow, pressure, specific power input), and gives the best results at atmospheric pressure, which is most interesting for real applications.

---

This chapter is submitted as: I. Belov; S. Paulussen; A. Bogaerts, Carbon Dioxide Dissociation in the Microwave Plasma Reactor operating in a wide pressure range and different gas inlet configurations, Journal of CO<sub>2</sub> utilization

## 6-1 Introduction

Besides DBDs, MW discharges are also intensively studied for CO<sub>2</sub> conversion and are considered to be one of the most promising plasma systems for CO<sub>2</sub> decomposition due to their capability to utilize the highly efficient vibrational excitation kinetics of the non-equilibrium discharge.<sup>[14, 53, 204, 205]</sup> In this way, it is possible to realize CO<sub>2</sub> dissociation with a higher energy efficiency than in the conventional thermal process.<sup>[5, 25]</sup> From a technological point of view, MW plasma systems represent an electrodeless solution with a high electric energy utilization efficiency and a fast switching on time.<sup>[54]</sup> Another advantage of CO<sub>2</sub> decomposition in a MW discharge reactor relates to the possibility to utilize electricity produced from renewable sources, thus balancing the power grid.<sup>[4]</sup>

Chapter 1 contains a historical overview on the development of CO<sub>2</sub> decomposition in MW plasma. Besides that, a lot of novel approaches to improve the performance of CO<sub>2</sub> decomposition in MW plasma systems were recently presented. Chen *et al.* reported a twofold increase of the conversion and energy efficiency when a NiO catalyst on a TiO<sub>2</sub> support was installed downstream of a surface-wave MW CO<sub>2</sub> discharge<sup>[56, 58, 59]</sup>, reaching a conversion and energy efficiency of both 42%. Uhm *et al.* reported a high CO<sub>2</sub> conversion (45%, but with an energy efficiency of only 8%) for an atmospheric pressure MW plasma torch with a post-discharge coal powder gasification system.<sup>[60]</sup> Mitsingas *et al.* presented a highly efficient CO<sub>2</sub> dissociation process in a compact atmospheric pressure MW plasma reactor<sup>[67]</sup>, achieving 50-80% energy efficiency, but at low conversion (9-3%). The introduction of gas admixtures to a CO<sub>2</sub> MW discharge could be used to achieve some degree of control over the plasma parameters and to utilize more efficient pathways for CO<sub>2</sub> decomposition. The influence of Ar<sup>[62, 63]</sup>, N<sub>2</sub><sup>[64]</sup>, H<sub>2</sub><sup>[51, 65]</sup> and H<sub>2</sub>O<sup>[56, 58, 59, 61]</sup> gas admixtures on CO<sub>2</sub> dissociation in a MW plasma was demonstrated experimentally and by modeling. Such research is also important for the future up-scaling of the process, as gas impurities are inevitable on an industrial scale.

Another ongoing research direction related to efficient CO<sub>2</sub> decomposition in a MW plasma is targeting *in-situ* diagnostics to allow a better understanding of the discharge mechanisms and process control<sup>[17, 62, 63, 114, 206]</sup>. Likewise, modeling has also proven to give valuable insight in the underlying mechanisms of CO<sub>2</sub> dissociation in a MW plasma, including the role of vibrational kinetics, and identifying the limitations in the conversion and energy efficiency in a wide range of conditions.<sup>[53, 64, 204, 205]</sup>

Despite all the recent attention to this technology, studies of the MW plasma operating in CO<sub>2</sub> in a broad range of process parameters and gas flow configurations are still rare. Usually only a very limited parameter range is presented. Moreover, given the development stage of the technology, it is still unclear which discharge conditions are the most beneficial for scale-up. In this Chapter, we utilize the opportunity to generate a stable MW discharge in pure CO<sub>2</sub> over a wide pressure range and with different gas inlet regimes to study the CO<sub>2</sub> conversion reaction in this broad range of conditions. Thus, the aim of this Chapter is to demonstrate the influence of pressure, gas flow configuration and post-discharge cooling on the CO<sub>2</sub> decomposition process in a MW discharge reactor. This work will be useful for further up-scaling of MW plasma systems, which will be necessary to bring plasma-based CO<sub>2</sub> conversion into real application.

## 6-2 System description

The way the gas is supplied to the reactor has a significant influence on the MW discharge operation.<sup>[54]</sup> In this Chapter three configurations of the gas inlet system are presented (**Figure 6-1**).

In the first configuration, the CO<sub>2</sub> flow is introduced from the top of the discharge zone through a gas shower (**Figure 6-1, a**). This configuration will be further referred to as "*direct flow configuration*". The temperature of the afterglow is monitored via a thermocouple installed downstream of the reactor.

In the second case, the gas flow direction is opposite: CO<sub>2</sub> is filling the vacuum chamber first and then entering the discharge tube from the bottom (**Figure 6-1**, “*reverse configuration*”). After passing the plasma zone, the hot gas is directed through a water-cooled gas shower at the top. The gas inlet device depicted in **Figure 6-1, b** has an adjustable position (cf. **Figure 2-3**), i.e. it can be fixed along the vertical axis. For the reverse configuration, the gas inlet device is placed in the proximity of the plasma zone to stabilize the discharge, but it is not connected to the gas feed.

In the third case (**Figure 6-1**, “*vortex configuration*”), CO<sub>2</sub> is supplied to the discharge zone through a tangential gas inlet at the bottom (also depicted in **Figure 2-3**). This stainless steel swirl gas inlet has four 3 mm holes in the tangential direction in order to create a vortex flow pattern. The processed gas is also directed through the water-cooled gas shower at the top. The afterglow temperature is measured with a thermocouple installed after the gas shower, similar to the case of the “reverse” set-up.

It is important to notice that here we use the input power in equation 2-4, and not the plasma power as is often done in the literature <sup>[17, 56, 65, 206]</sup>. In some systems, like DBDs, the plasma power can be only half of the input power, but in the MW system, the difference is usually quite small (can be estimated to be around 10% <sup>[54]</sup>). Still, there are some losses due to the reflectance of the incident MW (that is minimized but still present) and unwanted absorbance on the discharge parts. Note that if we would use the plasma power in our calculation, the reported energy efficiencies (due to the lower energy input used in calculation) would be ca. 5-10% higher.

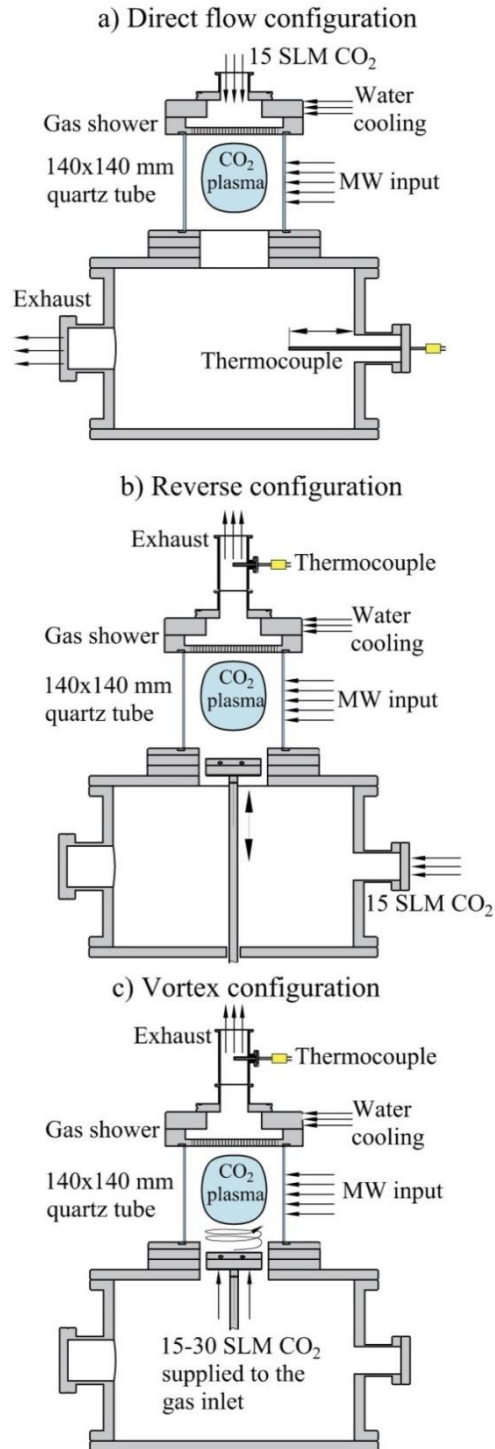


**Figure 6-1.** Various gas input configurations of the MW plasma reactor.

## 6-3 Results and discussion

### 6-3-1 Effect of the pressure

The CO<sub>2</sub> conversion and energy efficiency of the process are plotted as a function of gas pressure in **Figure 6-2**, for the three different gas inlet configurations of the MW plasma reactor. Both the MW power (4.75 kW) and gas flow rate (15 SLM CO<sub>2</sub>) are kept constant, and thus the energy input, SEI, is also fixed (i.e., 4.8 eV/molec). All these configurations exhibit a drop of the conversion and energy efficiency upon increasing pressure, consistent with model calculations.<sup>[204]</sup> However, remarkable differences in maximum conversion for the various gas inlet regimes are observed. Indeed, the direct configuration yields a conversion of 3.5% at 200 mbar, while values of 38.2% and 23.8% are measured for the reverse and vortex systems at the given conditions, respectively. The energy efficiency exactly follows the trend of the conversion, because the SEI is kept constant.

Furthermore, as the drop in conversion and energy efficiency is more pronounced for the reverse configuration than for the vortex setup, it is interesting to note that the reverse configuration is more efficient at 200 mbar (with conversion of 38.2% and energy efficiency of 23.1%, vs 23.8% and 14.2% for the vortex regime), while the latter exhibits a higher conversion and energy efficiency at 1 bar (i.e., conversion of 11.3% and energy efficiency of 6.9%, vs 6.2% and 3.7% for the reverse configuration).

The drop in conversion and energy efficiency upon increasing pressure in the MW discharge is somewhat expected. First of all, it is known that at atmospheric pressure the rotational and vibrational temperatures of the MW plasma are in thermal equilibrium<sup>[66]</sup>. This leads to a high gas temperature. At the same time, the most efficient mechanism of CO<sub>2</sub> decomposition, i.e., through vibrational excitation of the asymmetric mode of CO<sub>2</sub><sup>[25]</sup>, becomes less dominant with higher temperature and pressure<sup>[204]</sup>. The latter is explained by the depletion of the high vibrationally-excited

CO<sub>2</sub> molecules through vibrational-translational relaxation, stimulated by both pressure and temperature. In addition, the drop in conversion and energy efficiency in a MW plasma reactor at higher pressure can also be attributed to the CO recombination Reactions 6-1 and 6-2:



It was demonstrated by Berthelot *et al.* that the reaction rates of Reactions 6-1 and 6-2 increase with temperature and pressure, thus indeed limiting the CO<sub>2</sub> conversion<sup>[204]</sup>.

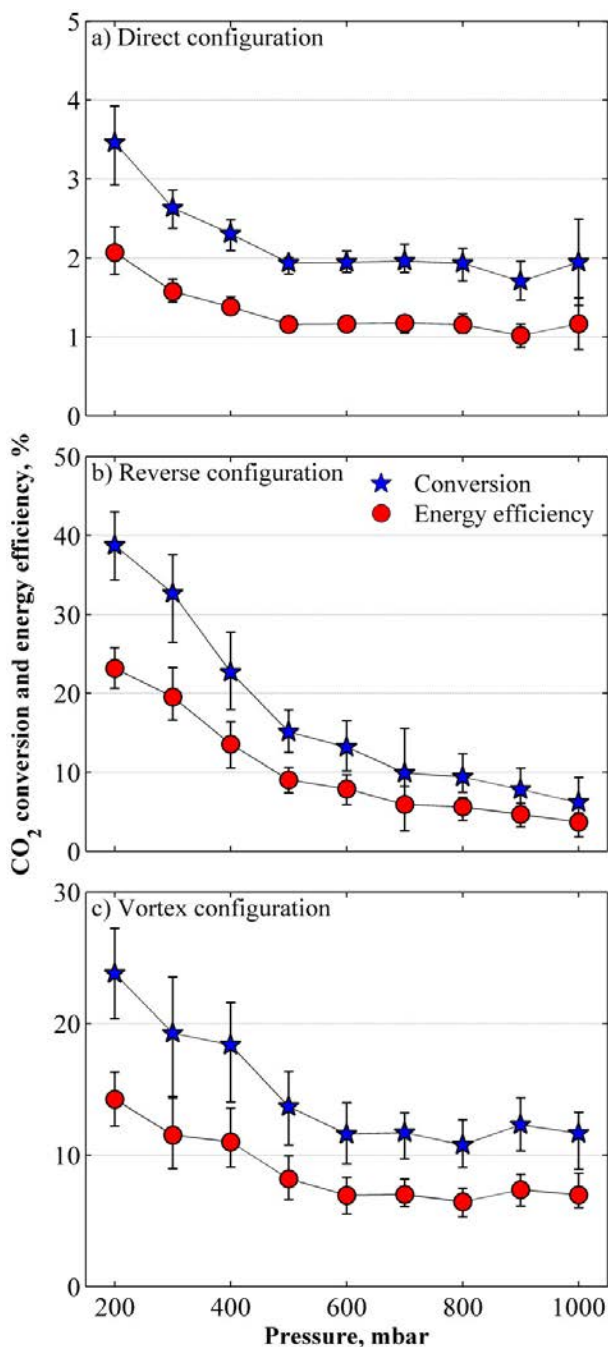


**Figure 6-2.** CO<sub>2</sub> conversion and energy efficiency obtained in the MW plasma at 4.75 kW input power and 15 SLM CO<sub>2</sub> flow rate (corresponding to an SEI of 4.8 eV/molec), for the three different gas inlet configurations, upon increasing the pressure.

### 6-3-2 Effect of the flow rate in the vortex configuration

The aim of this work is to target the operation of a stable MW discharge in a wide (200-1000 mbar) pressure range and a wide range of gas flow rates. For the direct and reverse configuration, however, a stable discharge in this entire pressure range can only be achieved in a narrow window of process parameters (15 SLM CO<sub>2</sub> – 4.75 kW). For instance, it is not possible to sustain a reliable discharge at pressures above 500 mbar when applying a CO<sub>2</sub> flow rate higher than 15 SLM in the direct and reverse configuration. In contrast, the vortex gas inlet regime allowed various flow rates (between 15 and 30 SLM CO<sub>2</sub>) to be tested (cf. **Figure 6-3**). A vortex gas flow regime has been utilized before in MW plasma systems to avoid overheating of the reactor walls<sup>[17, 54]</sup> and allows to operate the MW plasma in a wider regime of conditions. Interestingly, it can be deduced from **Figure 6-3** that the MW plasma in vortex configuration yields a very similar conversion in the entire range of gas flow rate investigated, i.e., from 15 SLM to 30 SLM. This is quite remarkable, because a drop in conversion upon increasing flow rate is usually observed at constant power in most plasma experiments<sup>[5, 15, 41, 71]</sup>, although the non-linear influence of flow rate on the CO<sub>2</sub> conversion was also reported for MW plasmas in CO<sub>2</sub>+H<sub>2</sub> gas mixtures<sup>[65]</sup>, a CO<sub>2</sub> RF discharge<sup>[27]</sup> and gliding arc plasmatron reactors<sup>[70, 72]</sup>. This effect might be attributed to the complex interplay between the vortex gas pattern, the non-uniform absorption of MW power and the chemistry of CO<sub>2</sub> decomposition.

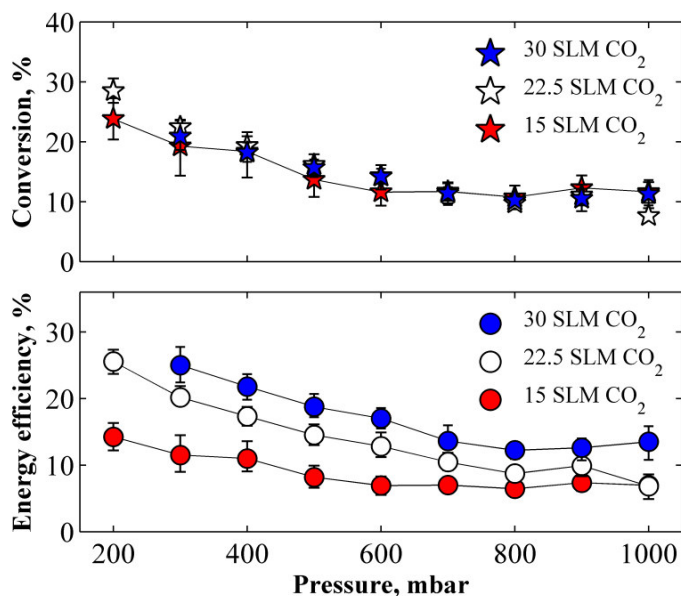


**Figure 6-3.** CO<sub>2</sub> conversion and energy efficiency in the MW plasma in the vortex configuration as a function of pressure, at a MW power of 4.75 kW and three different flow rates (15, 22.5 and 30 SLM).

As the conversion appears to be independent of the gas flow rate, the energy efficiency obviously rises substantially upon higher flow rates (as can be explained from Equation 2-5), reaching values of 11.5%, 20.1% and 25%, for 15, 22.5 and 30 SLM CO<sub>2</sub>, respectively, at 300 mbar. A further increase of the flow rate is not feasible due to pumping limitations. For the same reason, the lowest pressure feasible at 30 SLM CO<sub>2</sub> flow rate is only 300 mbar.

### 6-3-3 CO<sub>2</sub> conversion in the MW discharge at 200 mbar

It is interesting to note that the largest difference in CO<sub>2</sub> conversion and energy efficiency for the various gas inlet configurations of the MW discharge is observed at 200 mbar (cf. **Figure 6-2**). To further investigate this effect, the reverse and vortex configurations are compared, while varying the flow rate and power input (**Figure 6-4**). We perform this comparison at 200 mbar, where a stable discharge could be sustained in a wide range of process parameters for both gas inlet regimes. For the reverse

configuration, a higher power or a lower flow rate result in a proportional rise of the conversion, which is like expected. The effect is opposite for the energy efficiency, which is also like expected, (based on Equations 2-4 and 2-5 in **Chapter 2**), although the flow rate of 15 SLM still gives a slightly higher energy efficiency than the flow rate of 20 SLM. Thus, a flow rate of 15 SLM CO<sub>2</sub> and 3.75kW input power yields the highest energy efficiency of around 25%. On the other hand, in the vortex configuration, the flow rates of 15 and 20 SLM CO<sub>2</sub> yield rather similar conversion. As a result, the regime with 20 SLM is more efficient than 15 SLM, with the highest energy efficiency of 26% at 2.75 kW MW power input. This behavior is consistent to our previous observation of the vortex configuration in the 200-1000 mbar pressure range (cf. **Figure 6-3**). The conversion at 20 SLM is quite similar in both the vortex and reverse configuration, but the latter configuration yields a much higher conversion at 15 SLM, as is also obvious from **Figure 6-2** above.

Remarkably, when a CO<sub>2</sub> flow rate of 5 SLM is applied at high power (>3.75 kW), the conversion appears to be much higher in the vortex gas inlet configuration. At 4.75 and 5.75 kW power input, conversions of 69% and 75% (with energy efficiencies of 14% and 12%, respectively) are measured for the vortex configuration, vs. 50% and 53% (corresponding to energy efficiencies of 9.8% and 8.7%) for the reverse configuration, respectively. Moreover, the 5 SLM vortex flow regime is more efficient than the reverse flow regime for the entire power input range, with maximum energy efficiency of 14% at 2.75 kW MW power, corresponding to 41% conversion, while the reverse configuration yields 12% energy efficiency with a conversion of 34% for the 5 SLM – 2,75 kW discharge.

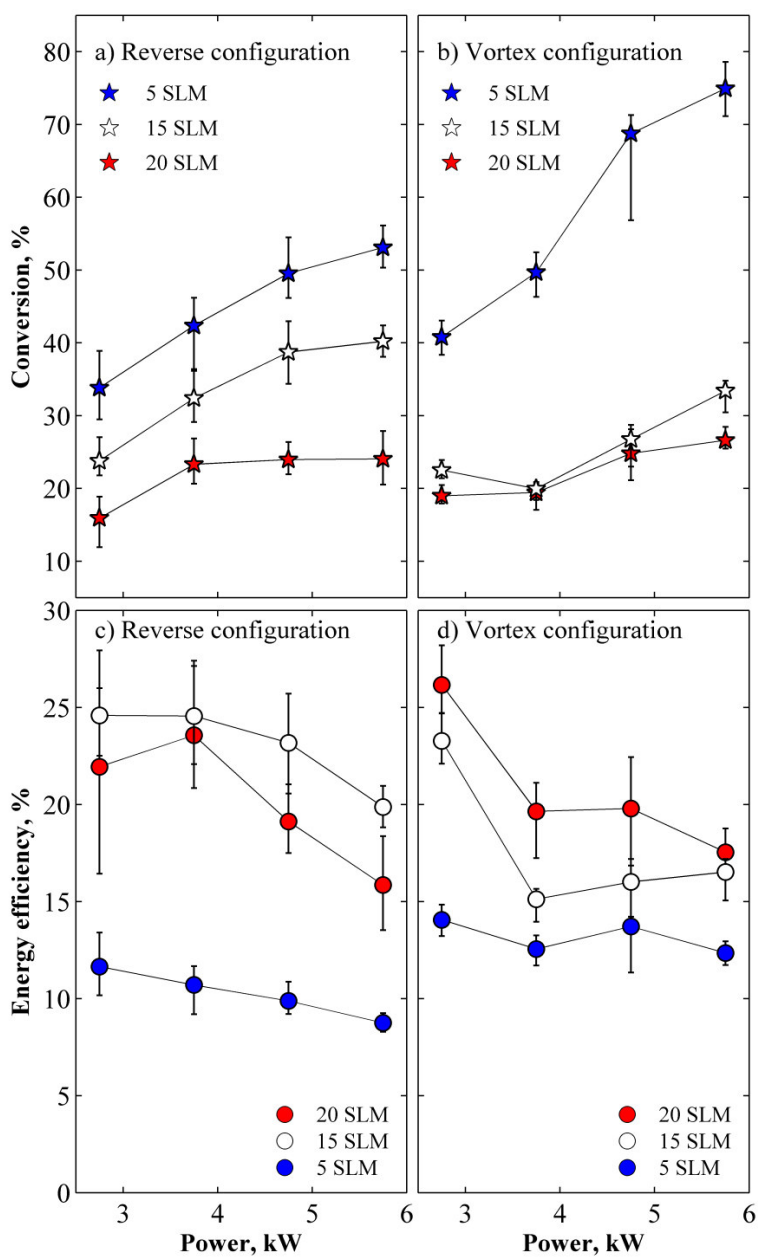


**Figure 6-4.** CO<sub>2</sub> conversion and energy efficiency in the MW plasma in reverse (a,c) and vortex configurations (b,d), as a function of input power, at 200 mbar and three different gas flow rates.

### 6-3-4 Post-discharge temperature measurement

It is known that the downstream processes significantly influence the overall efficiency of the CO<sub>2</sub> conversion process and that they are governed by the pressure and temperature dependent CO recombination reactions (cf. Reactions 6-1, 6-2)<sup>[204]</sup>. Hence, a pressure increase and a post-discharge cooling will have a prominent influence on the MW discharge reactor exhaust properties and thus on the efficiency of CO<sub>2</sub> conversion. To investigate these effects, the temperature downstream of the MW discharge reactor in all three gas flow configurations is measured (cf. **Figure 6-1**) upon increasing the pressure. For the direct gas inlet configuration, the thermocouple is placed at different radial positions inside the vacuum chamber and 20 cm below the MW plasma reactor itself (cf. **Figure 6-1**), and the data obtained (**Figure 6-5**) illustrate that the exhaust temperature decreases when moving away from the chamber axis and when the pressure increases. Although the temperature is measured 20 cm below the MW plasma reactor, still values as high as 1000 K are obtained at 200 mbar, at 4 cm from the axis. The indication “discharge zone” in **Figure 6-5** represents the area close to the reactor axis (~3 cm) where the thermocouple induces an additional discharge. Therefore, the temperature cannot be measured in this area. It is important to realize that, because the thermocouple is positioned 20 cm below the MW plasma reactor itself, the values presented in **Figure 6-5** will be affected by the heat exchange processes in this area. Inside the plasma reactor (and also directly in the afterglow), the gas temperature will even be much higher, certainly at higher pressure, as revealed among others by computer modeling.<sup>[204]</sup> The influence of the heat exchange processes on the exhaust temperature of the direct configuration will be discussed below.

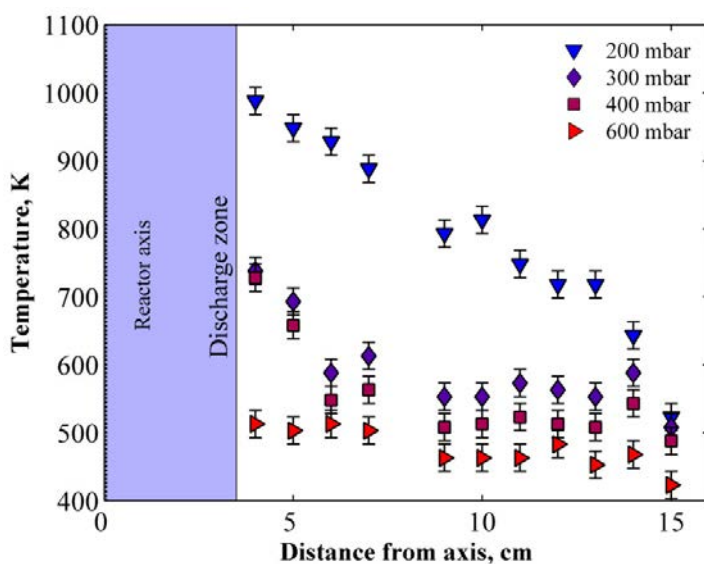


**Figure 6-5.** Temperature distribution as a function of distance from the central axis, measured in the vacuum chamber, at a position 20 cm downstream of the MW discharge reactor (see **Figure 6-1**), for the direct gas inlet configuration, at a power of 4.75 kW and a flow rate of 15 SLM CO<sub>2</sub>.

The pressure dependence of the exhaust temperature for the direct, reverse and vortex configurations is presented in **Figure 6-6**. For the reverse and vortex configuration the temperature is probed ~5 cm after the cooling stage (cf. **Figure 6-1**). The exhaust is substantially cooler in these cases at lower pressures, compared to the direct flow configuration that is operating without any quenching. At 200 mbar, values almost twice as high are achieved for the direct configuration compared to the reverse and vortex regimes (988 K vs 563 and 535 K, respectively). However, the temperature downstream of the reverse and vortex set-up increases with pressure. At 1 bar, temperatures of 788 K, 673 K and 473 K are measured for the vortex, reverse and direct configurations, respectively.

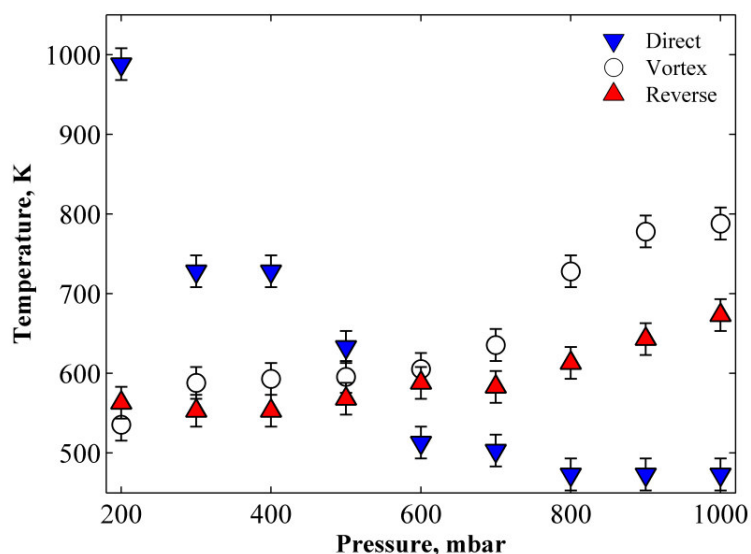


**Figure 6-6.** Exhaust temperature measurements for the direct, reverse and vortex gas inlet configurations of the MW plasma reactor, as a function of pressure, at a MW power of 4.75 kW and gas flow of 15 SLM CO<sub>2</sub>.

In case of the vortex configuration, we also investigated the effect of the flow rate (**Figure 6-7**). This is not possible in case of the direct and reverse configurations, where a stable plasma is only reached in a limited range of conditions, as mentioned above. Interestingly, increasing the flow rate has limited influence on the exhaust temperature of the vortex regime at lower pressures (up to 700 mbar), while the difference becomes more prominent closer to atmospheric conditions. The exhaust temperature of the MW discharge with 15, 22.5 and 30 SLM CO<sub>2</sub> supplied to the MW plasma reactor through the vortex gas inlet at 1 bar equals 788 K, 743 K and 683 K, respectively. The reason for this behavior might be attributed to the fact that the specific power input is decreasing with rising gas flow rate.

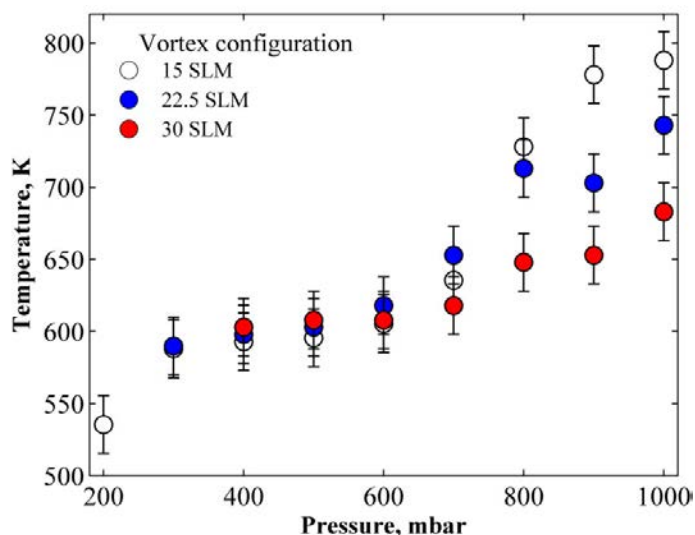


**Figure 6-7.** Post-discharge temperature measurements for the vortex gas inlet configurations of the MW plasma reactor, as a function of pressure and gas flow rate, at a MW power of 4.75 kW.

The afterglow temperature measurements allow us to obtain a better understanding of the poor performance of the MW discharge operating in the direct gas flow configuration, even at low pressure (cf. **Figure 6-6**). Indeed, in this case, temperatures up to 1000 K are measured downstream of the reactor. In reality, the values in the discharge afterglow will be even higher, because the thermocouple could only be placed at a certain distance from the reactor axis (i.e., above 4 cm) and quite far away from the plasma reactor (i.e., 20 cm) (cf. **Figure 6-5** and **Figure 6-1**). It is thus clear that inside the plasma reactor, the temperatures will be much higher, as also revealed from model calculations.<sup>[204]</sup>

In case of the reverse and vortex flow configurations, the temperature inside the plasma will also be high, but the cooling step installed downstream the reactor in these two configurations allows a decrease of the exhaust temperatures down to ~550 K at 200 mbar. The higher conversion achieved in these regimes compared to the direct configuration (cf. **Figure 6-6**) might thus be attributed to the lower temperature in the afterglow. It was demonstrated by Berthelot *et al.* that even at 200 mbar the

reaction rate of CO recombination (Reaction 6-1) increases when the temperature rises from 300 K to 1000 K <sup>[204]</sup>. In this way, we can argue that the excessive exhaust temperatures of the direct configuration of the MW discharge reactor highly limit the performance of this system for CO<sub>2</sub> conversion, while the introduction of a quenching step downstream in case of the vortex and reverse gas flow inlet configurations allows to obtain substantially higher conversions and energy efficiencies. However, in **Figure 6-6** it can be noted that rather high temperatures (up to 700-800 K) are still achieved downstream the reverse and vortex configurations at higher pressures. This may indicate that the cooling rate is not sufficient in these cases and thus that the CO<sub>2</sub> conversion and energy efficiency in these systems can be further enhanced by improving the exhaust cooling system. Some possibilities to achieve this would be the introduction of another cooling stage or increasing the contact time of the exhaust gas in the quenching step. Besides that, to have a better understanding of the MW discharge thermalisation with rising pressure, it would be useful to apply optical emission spectroscopy (OES) inside the plasma reactor. By means of OES it is possible to estimate the vibrational and rotational temperatures of the plasma and thus to analyze how close they are to thermal equilibrium.<sup>[66]</sup>

It is also interesting to observe the influence of rising pressure on the exhaust temperature of the MW discharge in the direct flow configuration. In general, the gas temperature of a MW plasma is expected to increase upon increasing pressure.<sup>[66, 204]</sup> This is indeed observed when studying the exhaust temperature of the MW discharge in the reverse and vortex gas flow configurations (cf. **Figure 6-6**). At first glance it may seem that the opposite is the case for the direct gas inlet configuration. However, we need to keep in mind that the values presented in **Figure 6-5** and **Figure 6-6** for the direct flow set-up are measured only at a distance of 20 cm from the MW plasma and at least 4 cm from the central axis. Hence, this is quite far in the afterglow, or even beyond the afterglow of the plasma. It should be noted that these values are highly affected by heat exchange processes occurring in the chamber downstream of the reactor. Indeed, we might expect that the flow expansion in the vacuum chamber will

induce convective heat transfer, thus decreasing the exhaust temperature at that point. This process will be highly dependent on the chamber pressure and turbulence formed after the gas expansion. This can probably explain the downward trend of the post-discharge temperature upon increasing pressure, observed in **Figure 6-5** and **Figure 6-6**. The presented analysis might be also complimented by the OES measurements which would allow estimation of the rotational and vibrational temperature of the temperatures and thus deeper study the thermalisation of the plasma.<sup>[66]</sup>

### 6-3-5 Analysis and comparison with literature results

A summary of our CO<sub>2</sub> conversion experiments for the various conditions investigated in the three different configurations of the MW discharge reactor is presented in **Figure 6-8** and in **Table 6-1**. As stated before, the conversion and energy efficiency almost linearly drop upon increasing the pressure, regardless of the gas inlet configuration, although the drop is more pronounced for the reverse configuration. At an SEI of 4.8 eV/molec, which is realized at a MW power of 4.75 kW and a flow rate of 15 SLM, the direct configuration yields the lowest conversion and energy efficiency in the whole pressure range studied. This can be explained by the lack of downstream cooling. Indeed, as we can see in **Figure 6-1, a**, the heated exhaust mixture of the CO<sub>2</sub> discharge products expands into the vacuum chamber after passing through the discharge zone. In contrast to that, the reverse and vortex gas inlet configurations (**Figure 6-1, b** and **c**) have a quenching stage downstream of the plasma zone. The importance of post-discharge quenching was underlined in a number of papers<sup>[17, 25]</sup> and it was already stated, based on model predictions, that the CO recombination reactions (Reactions 6-1 and 6-2) are more prominent at higher temperature.<sup>[204]</sup>

In our study a conversion of 39% with a corresponding energy efficiency of 23% is achieved in the reverse flow configuration at 200 mbar and a CO<sub>2</sub> flow rate of 15 SLM. A somewhat higher energy efficiency, i.e., 25%, is obtained in the vortex flow configuration when 30 SLM CO<sub>2</sub> is supplied at 300 mbar, corresponding to a conversion

of 20%. Interestingly, the same flow configuration also demonstrated the best performance at atmospheric pressure: energy efficiencies of 14% and 12% are achieved, with a corresponding conversion of about 12%, at 30 and 15 SLM CO<sub>2</sub> flow rate in the vortex configuration at 1 bar, while an energy efficiency of only 3.7%, with a conversion of 6.2%, is obtained in the reverse configuration. Besides that, the 5 SLM CO<sub>2</sub> vortex regime at 200 mbar and MW power of 5.75 kW demonstrates the opportunity to obtain a very high conversion of up to 75% with an energy efficiency of 12.3%. Note that these energy efficiencies are calculated based on the input power. When using the plasma power, as often done in literature, they would be 5-10% higher due to the corresponding decrease of the absorbed power used in the calculation of SEI.

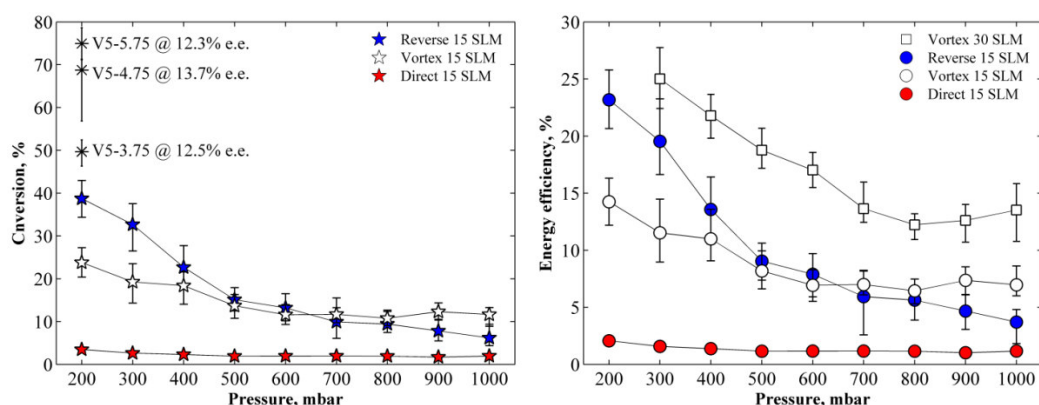


**Figure 6-8.** CO<sub>2</sub> conversion and energy efficiency in the MW plasma at 4.75 kW – 15 SLM (4.8 eV/molec) for the three different gas inlet configurations, upon increasing pressure. For the vortex configuration, the energy efficiency is also plotted at 30 SLM, while the values for the conversion are the same as at 15 SLM. Besides that, the conversion is presented for 5 SLM vortex gas flow at 200 mbar upon increasing power. In this case the regime is designated as “V5-X@ Y% e.e..” where X is power input in kW and Y is the corresponding energy efficiency. For the other configurations, no results are presented at other flow rates, because no stable plasma could be sustained in this wide pressure range.

To benchmark our results, we compare them with the data reported in literature for the CO<sub>2</sub> decomposition in MW discharges at various condition, see **Table 6-1**.

Operation at lower pressures makes it possible to fully exploit the non-equilibrium character of the MW plasma, with the potential to reach higher conversion and energy efficiencies.<sup>[25]</sup> It is demonstrated in this Chapter, but also by modeling<sup>[204]</sup> and in a number of experiments from literature<sup>[17, 206]</sup> that the pressure range between 150 and 300 mbar yields the higher conversion and energy efficiency, as it allows to utilize the most favorable CO<sub>2</sub> dissociation kinetics through the CO<sub>2</sub> vibrational levels.<sup>[204]</sup> Indeed, the highest energy efficiencies ever reported (~90%) for CO<sub>2</sub> MW plasma systems were obtained at these conditions, although this was also in combination with supersonic gas flow.<sup>[55]</sup> An advantage of operation at these moderate pressures is that only relatively cheap fore-vacuum pumps (cf. for instance the vacuum scheme in **Figure 2-4**) are required. However, the operational cost of such technology is still high, mostly due to the vacuum system energy consumption, and it may hinder the scale-up of the process.

Therefore, in a number of papers, operation at atmospheric pressure is targeted<sup>[60, 66, 67, 207]</sup>. Although it is known that the MW plasma is (nearly) in thermal equilibrium in this case, the atmospheric pressure systems have the undeniable advantage of vacuum-free operation. The data reported in literature for CO<sub>2</sub> conversion in MW plasmas at atmospheric pressure appear to be quite promising, with rather high energy efficiencies or conversions (although the combination of both is still limited). An interesting idea was elaborated in a series of articles by Hong *et al.*<sup>[60, 207]</sup>, where the CO<sub>2</sub> activated in a MW plasma was utilized as an oxidant for Zn or coal powders that were introduced downstream of the MW plasma, and reacted as “M” in Reaction 6-3:



It is worth noticing that this process is not catalytic, as the interaction with material consumes oxygen and thus changes the stoichiometry of the reactants. As

presented in **Table 6-1**, this approach allows to achieve a conversion of 30-45%, with a corresponding energy efficiency of 14-8%, depending on the conditions.

Remarkably, Mitsingas *et al.* reached an energy efficiency of 50-80% in an atmospheric pressure MW plasma reactor, but the conversion was only around 9-3%.<sup>[67]</sup> The high energy efficiency obtained in the compact discharge formed between an 8 mm inner diameter nozzle and a 2.4 mm tungsten electrode can be attributed to the high plasma density, which is known to be beneficial for the CO<sub>2</sub> conversion, due to efficient population of the CO<sub>2</sub> vibrational levels.<sup>[204]</sup>

An important remark regarding MW reactors operating at atmospheric pressure is that the ignition of the MW discharge at these conditions requires the implementation of electric field concentrators<sup>[67]</sup> or large argon admixtures.<sup>[66]</sup> In our case the discharge is ignited at lower pressure (~100 mbar) without such ignition assistants also due to rather high MW power input applied in this study. Besides that, the data in literature, as well as presented in our work, indicate that there is a trade-off between the energy efficiency and conversion. Hence, at rather low conversion, the cost of product purification and separation would be a big issue for process up-scaling, even if the energy efficiency of the plasma process itself is rather high. Novel ways to improve the overall efficiency of the technology should be considered.

The introduction of a catalytic step might be interesting, to utilize the relatively hot exhaust mixture that was previously activated in the MW plasma (cf. **Figure 6-5** and **Figure 6-6** above). Post-discharge treatment of the CO<sub>2</sub> MW plasma reactor exhaust via a catalytic step was demonstrated by Chen *et al.*<sup>[56, 58, 59]</sup> and allowed a twofold increase of the conversion and energy efficiency (i.e., from 20% to 42% conversion and energy efficiency). Remarkably, the catalyst was pre-treated via a MW argon plasma in the same vacuum chamber prior to the CO<sub>2</sub> decomposition reaction. Interestingly, Spencer *et al.*, also implemented a catalyst downstream of an atmospheric pressure MW reactor, but this resulted in a drop of the conversion and energy efficiency<sup>[66]</sup>. This underlines that also unwanted reverse reactions can be catalyzed in the post-discharge step of MW plasma systems.

The introduction of hydrogen-containing admixtures, like  $\text{H}_2$ <sup>[51, 65]</sup> or  $\text{H}_2\text{O}$ <sup>[56, 58]</sup>, affects the plasma parameters, such as gas and electron temperature, and it allows the generation of syngas as a product. The advantage of this approach is that water is easily available, while  $\text{H}_2$  can be generated via another technology that consumes renewable electrical energy, i.e., electrolysis. Another suitable hydrogen-source gas could be  $\text{CH}_4$ , thus allowing the use of biogas as feed gas, but the number of papers on the combined  $\text{CO}_2/\text{CH}_4$  conversion in a MW plasma is very limited.<sup>[5]</sup>

The results in the literature are somewhat better than the ones presented here. First, we repeat here that the energy efficiencies reported in this work are obtained based on the input power input, and when we would calculate them from the plasma power, as often done in literature, they would be ca. 5-10% higher. Furthermore, the somewhat lower performance in our setup can also be attributed to the fact that a MW plasma reactor should be designed for utilization at a certain pressure and gas flow regime. In our study, the aim is not to obtain the highest possible conversion and energy efficiency, but to target a stable discharge operation in a wide pressure range and with several gas inlet configurations, to obtain more insight in the underlying mechanisms in this wider range of operating conditions, and this is realized by means of the rather large volume MW plasma system. However, it is known that high-density plasmas (and thus low-dimensional devices) are beneficial for  $\text{CO}_2$  conversion.<sup>[204]</sup> Nevertheless, such systems would not allow the versatility of our reactor. For instance, puncturing of the quartz tube is often observed in a MW discharge operating at high power per unit wall area without vortex flow gas feed<sup>[54]</sup>. In this way, it would not be possible to test the direct and reverse flow regimes that are demonstrated in our study in the whole pressure range of 200 mbar - 1 bar. Therefore, the operational regime (low or atmospheric pressure) and gas flow configuration (forward or vortex flow) should be chosen during the design stage in order to assemble an efficient system. This is, however, not the primary aim of the current work.

It is important to notice that the measurements of the CO<sub>2</sub> conversion in our case (and in most of the presented literature) have an *ex-situ* character, i.e. the gas is sampled at the reactor exhaust. It was demonstrated above that downstream processes are crucial for the process efficiency, as the CO recombination reactions can dominate in the hot afterglow of the CO<sub>2</sub> MW plasma. Therefore, *in-situ* diagnostics <sup>[62, 206]</sup> are required to better understand and control the operation of the discharge systems. Besides that, efforts to decrease the gas temperatures and thus the recombination reaction rates, while increasing the power density of the plasma, should have a positive impact on the energy efficiency of the process <sup>[208]</sup>. In practice, this can be realized by discharge pulsing <sup>[16]</sup>, *in-situ* extraction of oxygen <sup>[127, 209]</sup> and decreasing the reactor dimensions <sup>[67]</sup>, although the latter will not be beneficial in terms of throughput or upscaling.

**Table 6-1.** Summary of CO<sub>2</sub> conversion performance in different MW plasma reactors and for various discharge configurations and conditions.

Pressure, mbar	Conversion, %	Energy efficiency, %	SEI, eV/molec.	Specifications	Reference
200	74.9	12.3	17.5	V5-5.75 <sup>1</sup>	This work
200	38.7	23.1	4.8	R15-4.75 <sup>2</sup>	This work
300	20.9	25	2.4	V30-4.75 <sup>3</sup>	This work
1000	11.6	13.5	2.4	V30-4.75 <sup>3</sup>	This work
90	20	35	1.9	Forward flow	[62]
20	65	8	22.9	Pure CO <sub>2</sub> forward flow	[65]
20	~85	6	5.8	H <sub>2</sub> /CO <sub>2</sub> =3 forward flow	[65]
40	20	20	2.9	Only MW	[56]
40	42	42	2.9	MW+catalyst	[56]
200	~10	~90	0.3	Supersonic flow	[25]
127	~ 15	~ 50	~ 1	Vortex flow	[206]
212	~ 8	~ 40	~ 0.5	Vortex flow	[206]
200	83	24	10.3	Supersonic flow	[17]
200	47	35	3.9	Vortex flow	[17]
200	11	51	0.6	Vortex flow	[17]
1000	9	50	0.5	2 mm nozzle	[67]
1000	3	82	0.1	2 mm nozzle	[67]
1000	~45	~ 8	4.5	MW+ coal oxidation	[60]
1000	~32	~14	4	MW+ coal oxidation	[60]
1000	10	20	1.4	CO <sub>2</sub> + Ar	[66]

<sup>1</sup>- Vortex configuration with supplied 5 SLM CO<sub>2</sub> flow rate and 5.75kW power input

<sup>2</sup>- Reverse configuration with supplied 15 SLM CO<sub>2</sub> flow rate and 4.75kW power input

<sup>3</sup>- Vortex configuration with supplied 30 SLM CO<sub>2</sub> feed flow and 4.75kW power input

## 6-4 Conclusion

The CO<sub>2</sub> conversion in a MW discharge reactor in a wide pressure range (200 - 1000 mbar) is studied, while three different gas flow configurations are explored, i.e., direct, reverse and vortex flow regimes. In the direct gas flow configuration, the exhaust of the plasma reactor expands into the vacuum chamber without additional cooling. Afterglow temperatures up to 1000 K are measured at quite some distance from the outlet, so the exhaust temperature is probably still higher, and this can explain the very low conversion and energy efficiency (~3.5% and 2% at 200 mbar, and even lower values at higher pressures) that are obtained, due to the lack of quenching of the exhaust, allowing the backward reaction (i.e., recombination of CO into CO<sub>2</sub>) to occur at rather high rates. In the reverse flow configuration, the exhaust passes through a cooling stage during which quenching can occur. This regime results in the highest conversion (~38% at 200 mbar) obtained in this study (with a corresponding energy efficiency of ~23%), but the values drop significantly upon rising pressure. Finally, a vortex flow configuration is applied, which utilizes the same cooling and quenching approach as the reverse flow configuration, but in addition also a swirl flow pattern. This configuration allows to operate the MW plasma in a wider range of conditions (flow rate and power) in the entire pressure range. Therefore, the highest energy efficiencies (~25% at 300 mbar and ~13% at 1 bar, for a corresponding conversion of 21% and 12%) are achieved in this regime. An almost linear drop of the conversion and energy efficiency is observed upon increasing pressure for all gas flow configurations, although it is somewhat less pronounced for the vortex flow configuration. This drop can be attributed to thermalisation of the plasma at increasing pressure, leading in turn to (i) less efficient CO<sub>2</sub> dissociation by the vibrational kinetics (due to more prominent relaxation of the vibrational levels), and (ii) fast recombination of CO into CO<sub>2</sub>. Analysis of the exhaust temperature reveals that the post-discharge cooling is crucial for the system performance in terms of conversion and energy efficiency, and should be further optimized. MW plasma systems operating at atmospheric pressure

are probably the most interesting to be scaled-up, in spite of their lower conversion and energy efficiency, due to the vacuum-free operation conditions. From another point of view, the vortex configuration is the most promising, as it allows operation in a wider range of process parameters (flow, pressure, specific power input), and gives the best results at atmospheric pressure, which is most interesting for real applications. To further increase the conversion and energy efficiency of such systems, post-discharge treatment via catalytic or oxidative reactions can be implemented downstream, as demonstrated already in literature.

## Chapter 7

# Conclusion and outlook

---

## 7-1 Properties of microdischarges and CO<sub>2</sub> conversion

The largest portion of this thesis is dedicated to the research on the microdischarge properties of a DBD, identifying novel ways to control them, in order to improve the overall efficiency of CO<sub>2</sub> decomposition in a DBD reactor. Overall, it can be noted that a higher microdischarge current is beneficial for CO<sub>2</sub> splitting. First, in **Chapter 3** it is demonstrated that the high-current microdischarge regime and consequently the higher CO<sub>2</sub> conversion in the double dielectric DBD are induced by utilizing a conductive coating on one of the barrier layers. Second, as shown in **Chapter 5**, the microdischarge current increases with pressure and simultaneously an improved energy efficiency of the reaction is observed. Process intensification within a single microdischarge due to the increased power and electron density is most likely to be responsible for the observed conversion enhancement. That can also be related to the evaporation of the central metal electrode in CO<sub>2</sub>/O<sub>2</sub> DBDs described in **Chapter 4**: high-current microdischarges are observed only in these electronegative gasses (and not in N<sub>2</sub>, CO or Ar) and they induce electrode erosion presumably due to the higher energy density of these microdischarges.

It is known that in DBD systems it is not possible to directly control the properties of the microdischarges, as the applied voltage rise results in an increase of the microdischarge number.<sup>[29]</sup> In this way, even if we know that the higher current microdischarges are beneficial for the CO<sub>2</sub> conversion, it is not possible to induce this regime by means of a rise in the specific energy input. The properties of the microdischarges are related to the dynamics of their formation and thus they might be steered by controlling the breakdown and propagation phenomena. In **Chapter 3** it is demonstrated that the current of a single microdischarge depends on the conductivity of the electrode of negative polarity. The effect of fewer and stronger microdischarge formation upon pressure rise in CO<sub>2</sub>/O<sub>2</sub> DBDs demonstrated in **Chapter 5** can be attributed to the constrained breakdown in these gasses.

It would be interesting to continue further research on the properties of CO<sub>2</sub> microdischarges in a single-filament arrangement of a DBD reactor.<sup>[81, 104, 174, 198]</sup> Experiments in a single-filament DBD would allow precise measurements of the microdischarge properties (dimensions, current, dynamics of formation) that are not possible in our set-up. In the cited literature mostly N<sub>2</sub>-based gas mixtures are studied in double-dielectric configuration of a single-filament DBD.<sup>[174, 198]</sup> However, as presented in this thesis, pure CO<sub>2</sub> or O<sub>2</sub> DBDs in metal-dielectric arrangement have a lot of interesting aspects of their operation.

The evaporation of the metal electrode, as illustrated in **Chapters 4 and 5**, can potentially be utilised to introduce catalytic material into the gas phase.<sup>[131]</sup> In this way, several technological drawbacks of a conventional way of catalyst incorporation into a DBD reactor (need of a packing material and associated with it increased maintenance costs) can be potentially eliminated. For instance, a Ni wire or mesh can be used as an electrode in a CO<sub>2</sub> DBD. In addition to that, the process can be monitored by optical emission spectroscopy and this would be interesting both for plasma and catalyst studies. The process of evaporation can be stimulated by pressure increase, which is also beneficial for CO<sub>2</sub> conversion, as demonstrated in **Chapter 5**.

## 7-2 CO<sub>2</sub> conversion in MW plasma

In **Chapter 6** a versatile MW plasma system is utilised and allows to study CO<sub>2</sub> decomposition in a wide range of pressure (200 mbar- 1 bar) and gas flow regimes (direct, reverse and vortex). Operation at 200 mbar yields the highest conversion for all three gas flow configurations like expected.<sup>[25]</sup> A pressure increase results in a gradual decrease of the reaction energy efficiency. It is demonstrated that the post-discharge conditions significantly influence the CO<sub>2</sub> conversion. In the regime without downstream cooling the CO<sub>2</sub> conversion is not higher than 3.5%, while in the arrangement with an additional afterglow quenching values up to 38% are measured at the same power input of 4.8 eV/molec and at 200 mbar.

It is interesting to correlate the performance of the MW and DBD plasma reactors for CO<sub>2</sub> decomposition. In **Figure 7-1** the comparison of CO<sub>2</sub> conversion and energy efficiency in a MW plasma reactor at 200 mbar and in DBD at atmospheric pressure is presented. This figure serves to illustrate the mismatch between the most efficient plasmachemical system for CO<sub>2</sub> conversion (MW discharge at ~200 mbar) and the most scalable one (DBD at 1 bar). It can be seen that substantially higher energy efficiencies can be obtained in a MW system at lower SEI of ~1 eV/molec, while the difference tends to decrease in the higher SEI region. Moreover, somewhat better energy efficiencies might be expected for the optimised MW system, because in our case the set-up is tuned for a wide pressure range operation.

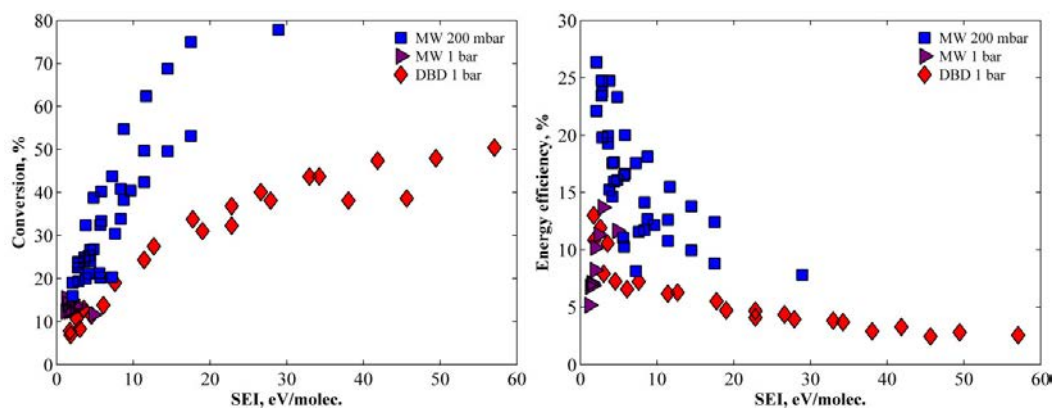


**Figure 7-1.** Comparison of CO<sub>2</sub> conversion and energy efficiency in a MW plasma reactor at 200 mbar and 1 bar (values for both reverse and vortex gas flow configuration) and in DBD at atmospheric pressure.

### 7-3 How can we further improve the CO<sub>2</sub> decomposition process?

Besides varying among different discharge types, several general approaches exist that can improve the energy efficiency of the plasma-based CO<sub>2</sub> decomposition: an increase of the power density (while keeping the gas temperature as low as possible) to enhance the role of vibrational levels in CO<sub>2</sub> conversion, deactivation of the reverse

reaction (i.e., CO recombination into CO<sub>2</sub>, cf. Reactions 6-1 and 6-2) and coupling of the plasma system with a catalytic step.<sup>[208, 210]</sup>

Miniaturisation of the plasma system through utilisation of sub-mm discharge dimensions would allow to increase the electron and power density<sup>[73]</sup>, however it might not be beneficial in terms of throughput or upscaling.

The CO recombination reaction can substantially influence the energy efficiency of the CO<sub>2</sub> decomposition process and can be stimulated by temperature and pressure<sup>[204]</sup> and oxygen content.<sup>[95]</sup> Therefore, a special hybrid reactor which combines a DBD set-up with a Solid Oxide Electrolyser Cell (DBD-SOEC) was used by Mori *et al.* for the CO<sub>2</sub> splitting reaction. 100% conversion was obtained when oxygen was in-situ depleted from the discharge.<sup>[209]</sup> Moreover, such system allowed direct synthesis of carbon nanotubes<sup>[211]</sup>, which is generally not observed in plasma reactors operating in pure CO<sub>2</sub>. The energy efficiency of the CO<sub>2</sub> decomposition process in the combined set-up was however rather low (ca. 0.1%), probably at least partly due to the low gas flow rate applied in the study (0.18-0.45 SCCM of CO<sub>2</sub>).

Plasma-catalysis is a very broad and complicated subject due to many known unknowns, but also due to numerous unknown unknowns of the mutual interactions of these matters.<sup>[210]</sup> Several successful examples of the integration of a catalytic step downstream the MW<sup>[56-59]</sup> or on the packing material in the DBD reactor<sup>[42, 95]</sup> were recently demonstrated. Zhang *et al.* demonstrated that a DBD packed with a mixture of BaTiO<sub>3</sub> and Ni/SiO<sub>2</sub> catalyst yielded a higher conversion (~23% at energy efficiency of 2.3%) than the same reactor packed only with BaTiO<sub>3</sub> beads (~19% at energy efficiency of 1.7%).<sup>[212]</sup> Interestingly, the reported plasma-catalytic process was rather heat-sensitive, as the CO<sub>2</sub> conversion dropped from 23% to 10% when the reactor temperature was controllably increased from 380K to 410K in a system containing Ni/SiO<sub>2</sub>. At the same time, this effect was negligible in a DBD packed only with BaTiO<sub>3</sub> beads. It was argued that the reverse Reactions 7-1, 7-2, 7-3 (where CO<sub>ad</sub> and O<sub>ad</sub> are the adsorbed species on the catalyst surface) are stimulated by a temperature increase, thus decreasing the CO<sub>2</sub> conversion.



This assumption is backed-up by the study of Spencer where a Rh/TiO<sub>2</sub> catalyst integrated in the post-discharge atmospheric-pressure MW plasma (with a gas temperature estimated to be around 6000K) has a negative impact on the CO<sub>2</sub> conversion (40% and ~6% energy efficiency without catalyst and 20% and ~3% energy efficiency with catalyst downstream). On the other hand, Chen *et al.* reported a twofold increase of the conversion and energy efficiency when a NiO catalyst on a TiO<sub>2</sub> support was installed downstream of a low-pressure surface-wave MW CO<sub>2</sub> discharge<sup>[56-59]</sup> (where the post-discharge temperature was ~470 K), reaching a conversion and energy efficiency of both 42%. In **Chapter 6** it was shown that the downstream temperature is highly influenced by the MW discharge operational pressure and gas flow regime, thus these parameters would affect the catalytic reactions as well. In this way, the analysis of the CO<sub>2</sub> MW process presented in **Chapter 6** might be useful for designing an efficient plasma-catalyst process.

In the same time the “real life” CO<sub>2</sub> streams containing various admixtures (mostly N<sub>2</sub>, but also H<sub>2</sub>O, O<sub>2</sub>, H<sub>2</sub>S, SO<sub>x</sub> depending on the source of the stream)<sup>[213]</sup> from industrial producers should be tested in plasma-chemical reactors. Not only the nitrogen content can significantly steer the process efficiency<sup>[64, 214]</sup>, but also the sulfur-based compounds can induce deposition of the solid product on the reactor walls, undermining the system performance.<sup>[215]</sup>

## Summary

The general acceptance of global warming stimulates the scientific community to work on novel and efficient technologies for CO<sub>2</sub> utilization. Conversion of CO<sub>2</sub> by means of non-thermal plasmas is one of the most promising current developments on this topic. Plasmachemical processes are very versatile, utilize electrical energy and reactor designs based on abundant construction materials. However, the energy efficiencies achieved in those systems so far, limit up to now the potential scale-up of a plasma-based CO<sub>2</sub> conversion technology. Besides that, control over the plasma process is not trivial, as the plasma chemistry is often governed by plasma parameters which cannot be directly determined by external settings.

In this thesis we explore novel mechanisms to control and improve CO<sub>2</sub> decomposition in Dielectric Barrier Discharge (DBD) and Microwave (MW) plasma systems. In case of a DBD it is accomplished by finding ways to tune the properties of transient microdischarges (also referred as filaments) that make up this type of plasma and define the overall efficiency of the process. It is demonstrated that a higher microdischarge current is beneficial for CO<sub>2</sub> conversion in a DBD. This effect can be induced by having a conductive surface on one of the DBD electrodes or via increasing the pressure. Interestingly, upon increase of the microdischarge current a process of metal electrode evaporation can also be triggered. This erosion process results in the re-deposition on the reactor walls, which significantly modifies the electrical properties of the CO<sub>2</sub> DBD and can potentially be used to introduce catalyst material into gas-phase.

In contrary to DBD reactors, operating at atmospheric pressure, MW discharges have the highest energy efficiency of CO<sub>2</sub> decomposition at lower pressure (~200 mbar). In this thesis it is demonstrated that a pressure increase induces a drop of energy efficiency of the MW reactor due to thermalisation of the MW plasma at near-atmospheric conditions. The properties of the MW discharge can be tuned, however, by adjusting the gas flow regime. It is demonstrated that the vortex gas flow allows the

most stable discharge operation and the highest achieved energy efficiency at atmospheric pressure. The obtained information can be useful for further MW plasma reactor scale-up.

## Samenvatting

De algemene erkenning van de opwarming van de aarde ten gevolge van toenemende CO<sub>2</sub>-uitstoot vormt een belangrijke stimulans voor de wetenschappelijke wereld om op zoek te gaan naar nieuwe en efficiënte technologieën voor hergebruik van CO<sub>2</sub>.

Omzetting van CO<sub>2</sub> naar andere bruikbare chemicaliën door middel van koude plasmatechnologie is één van de meeste veelbelovende ontwikkelingen in dit domein. Plasmachemie is een veelzijdige technologie die gebruik maakt van elektrische energie en werkt met reactoren die gebouwd kunnen worden met overvloedig beschikbare materialen. Tot nu toe is de energie-efficiëntie die met dergelijke processen bekomen wordt echter laag, wat opschaling en implementatie van plasma-gebaseerde CO<sub>2</sub> conversie limiteert. Daarnaast is ook de controle en aansturing van plasma processen niet triviaal aangezien de plasma-parameters die het proces grotendeels bepalen niet rechtstreeks extern ingesteld kunnen worden.

In deze thesis worden nieuwe mechanismen onderzocht om de controle en daardoor ook de efficiëntie van CO<sub>2</sub>-splitsing in een Diëlektrische Barrière Ontlading (DBD) en een Microgolf (MW) Plasma te verhogen.

In het geval van een DBD-plasma werd een manier gevonden om de eigenschappen van micro-ontladingen te beïnvloeden. Micro-ontladingen, ook filamenten genoemd, zijn kortdurende ontladingen waaruit dit type van plasma bestaat en die de eigenschappen van het plasma bepalen. Een verhoging van de stroom in de micro-ontladingen blijkt de CO<sub>2</sub>-omzetting in een DBD te bevorderen en dit effect kan bekomen worden wanneer één van de DBD elektrodes bedekt is met een geleidende laag of door verhoging van de procesdruk. Naast een verhoogde CO<sub>2</sub>-conversie geeft een verhoging van de stroom in de micro-ontladingen ook aanleiding tot verdamping

van de metalen elektrodes van een DBD-systeem. Dit proces van erosie van de elektrodes geeft aanleiding tot het afzetten van metaal elders in de reactor, waar de geleidende eigenschappen van het afgezette materiaal de elektrische eigenschappen van de DBD significant beïnvloeden. Dit fenomeen kan ook aangewend worden om katalytische materialen in de reactor te introduceren.

In vergelijking met DBD reactoren, waarin bij atmosferedruk gewerkt wordt, vertonen microgolf plasma's de hoogste energie-efficiëntie voor CO<sub>2</sub> decompositie, echter bij een lagere druk, ongeveer 200 mbar. In deze thesis wordt aangetoond dat een verhoging van de procesdruk in een microgolf plasma aanleiding geeft tot een sterke daling van de energie-efficiëntie ten gevolge van thermalisatie in condities die atmosferedruk benaderen. De eigenschappen van een MW-ontlading kunnen verder gecontroleerd worden door aanpassing aan het gasstroom regime dat wordt toegepast. In dit werk werd aangetoond dat de hoogste energie-efficiëntie bij atmosferedruk wordt bekomen in een microgolf ontlading waarin een vortex gasstroom wordt toegepast.

Met de bekomen nieuwe inzichten kan verdere optimalisatie van zowel DBD als MW plasma systemen aanleiding geven tot een meer efficiënte decompositie van CO<sub>2</sub>.

## List of Peer-Reviewed Publications

**I.Belov;** S. Paulussen; A. Bogaerts; Appearance of a conductive carbonaceous coating in a CO<sub>2</sub> Dielectric Barrier Discharge and its influence on the electrical properties and the conversion efficiency, Plasma Sources Sci. Technol. 2016 **25** 015023

**I.Belov;** J. Vanneste; M. Aghaee; S. Paulussen; A. Bogaerts Synthesis of micro- and nanomaterials in CO<sub>2</sub> and CO Dielectric Barrier Discharges. Plasma Processes and Polymers 2017 **14** e1600065

**I.Belov;** S. Paulussen; A. Bogaerts; Pressure as an additional control handle for non-thermal atmospheric plasma processes. Plasma Processes and Polymers 2017 **14** e1700046 (published online)

**I.Belov;** S. Paulussen; A. Bogaerts, Carbon Dioxide Dissociation in the Microwave Plasma Reactor operating in the wide pressure range and different gas inlet configurations, Journal of CO<sub>2</sub> utilization (To be submitted)

## List of Conference Contributions

I.Belov; S. Paulussen; A. Bogaerts; "Influence of reactor wall surface conductivity on the CO<sub>2</sub> discharge behavior in a dielectric barrier discharge reactor", **Oral presentation**, 22nd International Symposium on Plasma Chemistry (ISPC-22), Antwerpen, Belgium, July 5-10 2015.

I.Belov; S. Paulussen; A. Bogaerts; "Influence of reactor wall surface conductivity on the CO<sub>2</sub> discharge behaviour in a dielectric barrier discharge reactor", **Oral presentation**, Gaseous Electronic Conference -18 (GEC-18), Hawaii, USA, October 8-11 2015.

I.Belov; S. Paulussen; A. Bogaerts; "Deposition of Iron Oxide Nanoparticles by means of a CO<sub>2</sub>/O<sub>2</sub> Dielectric Barrier Discharge", **Poster**, Symposium "Synthesis of functional nanomaterials: fundamental understanding, scale-up, and design for applications", Duisburg, January 20-21, 2016

I.Belov; S. Paulussen; A. Bogaerts; "Synthesis of the micro-and nanomaterials in the CO<sub>2</sub> and CO dielectric barrier discharge", **Oral presentation**, IWPEEA-2016, Liverpool, United Kingdom, August 21-24, 2016

I.Belov; S. Paulussen; A. Bogaerts; "Analysis and comparison of the CO<sub>2</sub> and CO dielectric barrier discharge solid product", **Poster**, HAKONE XV, 11-16, September, 2016 Brno, Czech Republic

I.Belov; S. Paulussen; A. Bogaerts; "Synthesis of micro- and nanomaterials in CO<sub>2</sub> and CO Dielectric Barrier Discharges", **Oral presentation**, 4th RAPID Symposium, TU/e Eindhoven University of Technology, 4-7 October 2016

I.Belov; S. Paulussen; A. Bogaerts; "Synthesis of the micro-and nanomaterials in the CO<sub>2</sub> and CO dielectric barrier discharge", **Oral presentation**, Chemical Research in Flanders (CRF-1), Blankenberge, Belgium, 24-26 October, 2016

I.Belov; S. Paulussen; A. Bogaerts; "Pressure as an additional control handle for non-thermal atmospheric plasma processes", **Oral presentation**, International Workshop on Microplasmas, Garmisch-Partenkirchen, Germany, June 6th-9th, 2017

## References

- [1] G. Centi and S. Perathoner, Opportunities and prospects in the chemical recycling of carbon dioxide to fuels *Catalysis Today* **2009**, 148, 191.
- [2] Available:  
<http://www.engineeringchallenges.org/challenges/sequestration.aspx>
- [3] A. Al-Mamoori, A. Krishnamurthy, A. A. Rownaghi, and F. Rezaei, Carbon Capture and Utilization Update *Energy Technology* **2017**, 5, 834.
- [4] A. Goede and R. van de Sanden, CO<sub>2</sub>-Neutral Fuels *Europhysics News* **2016**, 47, 22.
- [5] R. Snoeckx and A. Bogaerts, Plasma technology – a novel solution for CO<sub>2</sub> conversion? *Chem Soc. Rev* **2017**, (under revision),
- [6] J. Ma, N. Sun, X. Zhang, N. Zhao, F. Xiao, W. Wei, and Y. Sun, A short review of catalysis for CO<sub>2</sub> conversion *Catalysis Today* **2009**, 148, 221.
- [7] G. S. Simate, S. E. Iyuke, S. Ndlovu, C. S. Yah, and L. F. Walubita, The production of carbon nanotubes from carbon dioxide: challenges and opportunities *Journal of Natural Gas Chemistry* **2010**, 19, 453.
- [8] S. Yagi and M. Kuzumoto, Silent discharges in ozonisers and CO<sub>2</sub> lasers *Aust. J. Phys.* **1995**, 48, 411.
- [9] W. Rath, CO<sub>2</sub> Laser – Workhorse for Industrial Manufacturing *Laser Technik Journal* **2009**, 6, 32.
- [10] R. Luce, Report: An investigation of the reduction of carbon dioxide in a silent electric discharge *Lockheed Missiles & Space company*, **1978**.
- [11] A. Vesel, M. Mozetic, A. Drenik, and M. Balat-Pichelin, Dissociation of CO<sub>2</sub> molecules in microwave plasma *Chemical Physics* **2011**, 382, 127.
- [12] J. Gruenwald, A Proposal for a Plasma Technology based Hybrid Life Support System for future Mars Habitats *Journal of Space technology* **2014**, 4,
- [13] J. Gruenwald, A hybrid plasma technology life support system for the generation of oxygen on Mars: Considerations on materials and geometry *Acta Astronautica* **2016**, 123, 188.
- [14] A. Bogaerts, T. Kozák, K. van Laer, and R. Snoeckx, Plasma-based conversion of CO<sub>2</sub>: current status and future challenges *Faraday Discussions* **2015**, 183, 217.
- [15] S. Paulussen, B. Verheyde, X. Tu, C. De Bie, T. Martens, D. Petrovic, A. Bogaerts, and B. Sels, Conversion of carbon dioxide to value-added chemicals in atmospheric pressure dielectric barrier discharges *Plasma Sources Science and Technology* **2010**, 19, 034015.
- [16] G. J. van Rooij, D. C. M. van den Bekerom, N. den Harder, T. Minea, G. Berden, W. A. Bongers, R. Engeln, M. F. Graswinckel, E. Zoethout, and M. C. M. van de Sanden, Taming microwave plasma to beat thermodynamics in CO<sub>2</sub> dissociation *Faraday Discussions* **2015**, 183, 233.
- [17] W. Bongers, H. Bouwmeester, B. Wolf, F. Peeters, S. Welzel, D. van den Bekerom, N. den Harder, A. Goede, M. Graswinckel, P. W. Groen, J. Kopecki, M.

- Leins, G. van Rooij, A. Schulz, M. Walker, and R. van de Sanden, Plasma-driven dissociation of CO<sub>2</sub> for fuel synthesis *Plasma Processes and Polymers* **2016**, 14, 201600126.
- [18] N. Barlow, Mars: An Introduction to its Interior, Surface and Atmosphere, *Cambridge University Press* **2008**.
- [19] *Oxygen-creating instrument selected to fly on the upcoming Mars 2020 mission*. Available: <https://phys.org/news/2014-08-oxygen-creating-instrument-upcoming-mars-mission.html>
- [20] U. Kogelschatz, Ozone and beyond: the marvelous development of dielectric barrier discharges *Journal of Physics D: Applied Physics* **2017**, 50, 051001.
- [21] M. Scapinello, E. Delikonstantis, and G. D. Stefanidis, The panorama of plasma-assisted non-oxidative methane reforming *Chemical Engineering and Processing: Process Intensification* **2017**, 117, 120.
- [22] R. Snoeckx, A. Rabinovich, D. Dobrynin, A. Bogaerts, and A. Fridman, Plasma-based liquefaction of methane: The road from hydrogen production to direct methane liquefaction *Plasma Processes and Polymers* **2017**, 14, e1600115.
- [23] H. Sekiguchi, T. Honda, and A. Kanzawa, Thermal plasma decomposition of chlorofluorocarbons *Plasma Chemistry and Plasma Processing* **1993**, 13, 463.
- [24] A. B. Murphy, A. J. D. Farmer, E. C. Horrigan, and T. McAllister, Plasma Destruction of Ozone Depleting Substances *Plasma Chemistry and Plasma Processing* **2002**, 22, 371.
- [25] A. Fridman, Plasma Chemistry, *Cambridge University Press*, New York **2008**.
- [26] D. Mei and X. Tu, Conversion of CO<sub>2</sub> in a cylindrical dielectric barrier discharge reactor: Effects of plasma processing parameters and reactor design *Journal of CO<sub>2</sub> Utilization* **2017**, 19, 68.
- [27] L. F. Spencer and A. D. Gallimore, Efficiency of CO<sub>2</sub> Dissociation in a Radio-Frequency Discharge *Plasma Chemistry and Plasma Processing* **2011**, 31, 79.
- [28] P. Bruggeman and R. Brandenburg, Atmospheric pressure discharge filaments and microplasmas: physics, chemistry and diagnostics *Journal of Physics D: Applied Physics* **2013**, 46, 464001.
- [29] V. G. Samoilovich, V. I. Gibalov, and K. V. Kozlov, Physical Chemistry of the Barrier Discharge 2 ed., *Deutscher Verlag für Schweisstechnik*, Düsseldorf **1997**.
- [30] A. V. Pipa, J. Koskulics, R. Brandenburg, and T. Hoder, The simplest equivalent circuit of a pulsed dielectric barrier discharge and the determination of the gas gap charge transfer *Review of Scientific Instruments* **2012**, 83, 115112.
- [31] R. Li, Y. Yamaguchi, S. Yin, Q. Tang, and T. Sato, Influence of dielectric barrier materials to the behavior of dielectric barrier discharge plasma for CO<sub>2</sub> decomposition *Proc of the 15 Int Symp on the Reactivity of Solids* **2004**, 172, 235.
- [32] R. Li, Q. Tang, S. Yin, Y. Yamaguchi, and T. Sato, Dense and strong plasma initiated by Ca<sub>0.7</sub>Sr<sub>0.3</sub>TiO<sub>3</sub> ceramic *Physics of Plasmas* **2004**, 11, 3715.

- [33] R. Li, Q. Tang, S. Yin, and T. Sato, Plasma catalysis for CO<sub>2</sub> decomposition by using different dielectric materials *Fuel Processing Technology* **2006**, *87*, 617.
- [34] R. Li, Q. Tang, S. Yin, and T. Sato, Investigation of dielectric barrier discharge dependence on permittivity of barrier materials *Applied Physics Letters* **2007**, *90*, 131502.
- [35] S. Wang, Y. Zhang, X. Liu, and X. Wang, Enhancement of CO<sub>2</sub> Conversion Rate and Conversion Efficiency by Homogeneous Discharges *Plasma Chem Plasma Process* **2012**, *32*, 979.
- [36] D. Mei, X. Zhu, Y.-L. He, J. D. Yan, and X. Tu, Plasma-assisted conversion of CO<sub>2</sub> in a dielectric barrier discharge reactor: understanding the effect of packing materials *Plasma Sources Science and Technology* **2015**, *24*, 015011.
- [37] T. Butterworth, R. Elder, and R. Allen, Effects of particle size on CO<sub>2</sub> reduction and discharge characteristics in a packed bed plasma reactor *Chemical Engineering Journal* **2016**, *293*, 55.
- [38] D. Yap, J. M. Tatibouet, and C. Batiot-Dupeyrat, Carbon dioxide dissociation to carbon monoxide by non-thermal plasma *Journal of CO<sub>2</sub> Utilization* **2015**, *12*, 54.
- [39] K. Van Laer and A. Bogaerts, Improving the conversion and energy efficiency of CO<sub>2</sub> splitting in a ZrO<sub>2</sub> packed bed DBD reactor *Energy Technol* **2015**, *3*, 1038.
- [40] I. Michielsen, Y. Uytendhouwen, J. Pype, B. Michielsen, J. Mertens, F. Reniers, V. Meynen, and A. Bogaerts, CO<sub>2</sub> dissociation in a packed bed DBD reactor: First steps towards a better understanding of plasma catalysis *Chemical Engineering Journal* **2017**, (in press).
- [41] R. Aerts, W. Somers, and A. Bogaerts, Carbon Dioxide Splitting in a Dielectric Barrier Discharge Plasma: A Combined Experimental and Computational Study *ChemSusChem* **2015**, *8*, 702.
- [42] D. Mei, X. Zhu, C. Wu, B. Ashford, P. T. Williams, and X. Tu, Plasma-photocatalytic conversion of CO<sub>2</sub> at low temperatures: Understanding the synergistic effect of plasma-catalysis *Applied Catalysis B: Environmental* **2016**, *182*, 525.
- [43] S.-J. Park, K. S. Kim, and J. G. Eden, Nanoporous alumina as a dielectric for microcavity plasma devices: Multilayer Al/Al<sub>2</sub>O<sub>3</sub> structures *Applied Physics Letters* **2005**, *86*, 221501.
- [44] X. Duan, Y. Li, W. Ge, and B. Wang, Degradation of CO<sub>2</sub> through dielectric barrier discharge microplasma *Greenhouse Gases: Science and Technology* **2015**, *5*, 131.
- [45] X. Duan, Z. Hu, Y. Li, and B. Wang, Effect of dielectric packing materials on the decomposition of carbon dioxide using DBD microplasma reactor *AIChE Journal* **2015**, *61*, 898.
- [46] T. Oh, Dissociation of Carbon Dioxide in Atmospheric Pressure Microchannel Plasma Devices, *MSc Thesis Thesis*, University of Illinois at Urbana-Champaign, **2013**.

- 
- [47] C. Shin, Dissociation of carbon dioxide in an Al/Al<sub>2</sub>O<sub>3</sub> microchannel plasma reactor at atmospheric pressure, *MSc Thesis*, University of Illinois at Urbana-Champaign, **2015**.
- [48] R. Aerts, T. Martens, and A. Bogaerts, Influence of Vibrational States on CO<sub>2</sub> Splitting by Dielectric Barrier Discharges *The Journal of Physical Chemistry C* **2012**, 116, 23257.
- [49] S. N. Andreev, V. V. Zakharov, V. N. Ochkin, and S. Y. Savinov, Plasma-chemical CO<sub>2</sub> decomposition in a non-self-sustained discharge with a controlled electronic component of plasma *Spectrochimica Acta Part A: Molecular and Biomolecular Spectroscopy* **2004**, 60, 3361.
- [50] V. I. Arkhipenko, A. A. Kirillov, T. Callegari, Y. A. Safronau, and L. V. Simonchik, Non-Self-Sustained Atmospheric Pressure Glow Discharges Maintained by the DC Helium Glow Discharge *IEEE Transactions on Plasma Science* **2009**, 37, 740.
- [51] J. F. de la Fuente, S. H. Moreno, A. I. Stankiewicz, and G. D. Stefanidis, On the improvement of chemical conversion in a surface-wave microwave plasma reactor for CO<sub>2</sub> reduction with hydrogen (The Reverse Water-Gas Shift reaction) *International Journal of Hydrogen Energy* **2017**,
- [52] Y. Lebedev, Microwave discharges at low pressures and peculiarities of the processes in strongly non-uniform plasma *Plasma Sources Science and Technology* **2015**, 24, 053001.
- [53] T. Kozák and A. Bogaerts, Evaluation of the energy efficiency of CO<sub>2</sub> conversion in microwave discharges using a reaction kinetics model *Plasma Sources Science and Technology* **2015**, 24, 015024.
- [54] J. F. de la Fuente, A. A. Kiss, M. T. Radoiu, and G. D. Stefanidis, Microwave plasma emerging technologies for chemical processes *Journal of Chemical Technology & Biotechnology* **2017**,
- [55] V. D. Rusanov, A. Fridman, and G. V. Sholin, The physics of a chemically active plasma with nonequilibrium vibrational excitation of molecules *Soviet Physics Uspekhi* **1981**, 24, 447.
- [56] G. Chen, N. Britun, T. Godfroid, V. Georgieva, R. Snyders, and M.-P. Delplancke-Ogletree, An overview of CO<sub>2</sub> conversion in a microwave discharge: the role of plasma-catalysis *Journal of Physics D: Applied Physics* **2017**, 50, 084001.
- [57] G. Chen, T. Godfroid, N. Britun, V. Georgieva, M.-P. Delplancke-Ogletree, and R. Snyders, Plasma-catalytic conversion of CO<sub>2</sub> and CO<sub>2</sub>/H<sub>2</sub>O in a surface-wave sustained microwave discharge *Applied Catalysis B: Environmental* **2017**, 214, 114.
- [58] G. Chen, V. Georgieva, T. Godfroid, R. Snyders, and M.-P. Delplancke-Ogletree, Plasma assisted catalytic decomposition of CO<sub>2</sub> *Applied Catalysis B: Environmental* **2016**, 190, 115.
- [59] G. Chen, T. Silva, V. Georgieva, T. Godfroid, N. Britun, R. Snyders, and M. P. Delplancke-Ogletree, Simultaneous dissociation of CO<sub>2</sub> and H<sub>2</sub>O to syngas in a surface-wave microwave discharge *International Journal of Hydrogen Energy* **2015**, 40, 3789.

- 
- [60] H. S. Uhm, H. S. Kwak, and Y. C. Hong, Carbon dioxide elimination and regeneration of resources in a microwave plasma torch *Environmental Pollution* **2016**, 211, 191.
- [61] H. S. Kwak, H. S. Uhm, Y. C. Hong, and E. H. Choi, Disintegration of Carbon Dioxide Molecules in a Microwave Plasma Torch *Sci Rep* **2015**, 5, 18436.
- [62] T. Silva, N. Britun, T. Godfroid, and R. Snyders, Study of CO<sub>2</sub> Decomposition in Microwave Discharges by Optical Diagnostic Methods *InTech* **2016**,
- [63] T. Silva, N. Britun, T. Godfroid, J. v. d. Mullen, and R. Snyders, Study of Ar and Ar-CO<sub>2</sub> microwave surfaguide discharges by optical spectroscopy *Journal of Applied Physics* **2016**, 119, 173302.
- [64] S. Heijkers, R. Snoeckx, T. Kozák, T. Silva, T. Godfroid, N. Britun, R. Snyders, and A. Bogaerts, CO<sub>2</sub> Conversion in a Microwave Plasma Reactor in the Presence of N<sub>2</sub>: Elucidating the Role of Vibrational Levels *The Journal of Physical Chemistry C* **2015**, 119, 12815.
- [65] J. F. de la Fuente, S. H. Moreno, A. I. Stankiewicz, and G. D. Stefanidis, Reduction of CO<sub>2</sub> with hydrogen in a non-equilibrium microwave plasma reactor *International Journal of Hydrogen Energy* **2016**, 41, 21067.
- [66] L. F. Spencer and A. D. Gallimore, CO<sub>2</sub> dissociation in an atmospheric pressure plasma/catalyst system: a study of efficiency *Plasma Sources Science and Technology* **2013**, 22, 015019.
- [67] C. M. Mitsingas, R. Rajasegar, S. Hammack, H. Do, and T. Lee, High Energy Efficiency Plasma Conversion of CO<sub>2</sub> at Atmospheric Pressure Using a Direct-Coupled Microwave Plasma System *IEEE Transactions on Plasma Science* **2016**, 44, 651.
- [68] A. Gutsol, Warm Discharges for Fuel Conversion in *Handbook of Combustion*, ed: Wiley-VCH Verlag GmbH & Co. KGaA, 2010.
- [69] T. Nunnally, K. Gutsol, A. Rabinovich, A. Fridman, A. Gutsol, and A. Kemoun, Dissociation of CO<sub>2</sub> in a low current gliding arc plasmatron *Journal of Physics D: Applied Physics* **2011**, 44, 274009.
- [70] S. Kim, M. Lim, and Y. Chun, Reduction Characteristics of Carbon Dioxide Using a Plasmatron *Plasma Chemistry and Plasma Processing* **2014**, 34, 125.
- [71] M. Ramakers, G. Trenchev, S. Heijkers, W. Wang, and A. Bogaerts, Gliding Arc Plasmatron: providing an alternative method for carbon dioxide conversion *ChemSusChem* **2017**, (in press).
- [72] S. C. Kim and Y. N. Chun, Development of a gliding arc plasma reactor for CO<sub>2</sub> destruction *Environmental Technology* **2014**, 35, 2940.
- [73] S. R. Sun, H. X. Wang, D. H. Mei, X. Tu, and A. Bogaerts, CO<sub>2</sub> conversion in a gliding arc plasma: Performance improvement based on chemical reaction modeling *Journal of CO<sub>2</sub> Utilization* **2017**, 17, 220.
- [74] D. Yuan, Z. Wang, C. Ding, Y. He, R. Whiddon, and K. Cen, Ozone production in parallel multichannel dielectric barrier discharge from oxygen and air: the influence of gas pressure *Journal of Physics D: Applied Physics* **2016**, 49, 455203.

- 
- [75] R. Spitzl, B. Aschermann, and M. Walter, Microwave plasma generator with the short cross-sectional side of the resonator parallel to the chamber axis *Google Patents* **2001**,
- [76] R. Snoeckx, Y. X. Zeng, X. Tu, and A. Bogaerts, Plasma-based dry reforming: improving the conversion and energy efficiency in a dielectric barrier discharge *RSC Advances* **2015**, 5, 29799.
- [77] D. Petrovic, Fluid modelling of an atmospheric pressure dielectric barrier discharge in cylindrical geometry *Journal of Physics D: Applied Physics* **2009**, 42, 205206.
- [78] L. Stollenwerk and U. Stroth, Electric Charging in Dielectric Barrier Discharges with Asymmetric Gamma-Coefficients *Contributions to Plasma Physics* **2011**, 51, 61.
- [79] V. I. Gibalov and J. P. Gerhard, The development of dielectric barrier discharges in gas gaps and on surfaces *Journal of Physics D: Applied Physics* **2000**, 33, 2618.
- [80] V. I. Gibalov and J. P. Gerhard, Dynamics of dielectric barrier discharges in different arrangements *Plasma Sources Science and Technology* **2012**, 21, 024010.
- [81] T. Hoder, R. Brandenburg, R. Basner, D. Weltmann, K. V. Kozlov, and H.-E. Wagner, A comparative study of three different types of barrier discharges in air at atmospheric pressure by cross-correlation spectroscopy *Journal of Physics D: Applied Physics* **2010**, 43, 124009.
- [82] C. L. Enloe, T. E. McLaughlin, R. D. Van Dyken, K. D. Kachner, E. J. Jumper, and T. C. Corke, Mechanisms and Responses of a Single Dielectric Barrier Plasma Actuator: Plasma Morphology *AIAA Journal* **2004**, 42, 589.
- [83] C. L. Enloe, M. McHarg, F. Gabriel, and M. Thomas, Plasma-induced Force and Self-induced Drag in the Dielectric Barrier Discharge Aerodynamic Plasma Actuator *47th AIAA Aerospace Sciences Meeting Aerospace Sciences Meetings* **2009**,
- [84] M. Šimek, S. Pekárek, and V. Prukner, Influence of Power Modulation on Ozone Production Using an AC Surface Dielectric Barrier Discharge in Oxygen *Plasma Chem Plasma Process* **2010**, 30, 607.
- [85] M. Šimek, S. Pekárek, and V. Prukner, Ozone Production Using a Power Modulated Surface Dielectric Barrier Discharge in Dry Synthetic Air *Plasma Chem Plasma Process* **2012**, 32, 743.
- [86] S. Pekárek, Asymmetric properties and ozone production of surface dielectric barrier discharge with different electrode configurations *Eur. Phys. J. D* **2013**, 67, 1.
- [87] K. Allegraud, O. Guaitella, and A. Rousseau, Spatio-temporal breakdown in surface DBDs: evidence of collective effect *Journal of Physics D: Applied Physics* **2007**, 40, 7698.

- 
- [88] I. Biganzoli, R. Barni, C. Riccardi, A. Gurioli, and R. Pertile, Optical and electrical characterization of a surface dielectric barrier discharge plasma actuator *Plasma Sources Science and Technology* **2013**, 22, 025009.
- [89] N. Benard and E. Moreau, Electrical and mechanical characteristics of surface AC dielectric barrier discharge plasma actuators applied to airflow control *Exp Fluids* **2014**, 55, 1.
- [90] Z. Falkenstein and J. Cogan, Microdischarge behaviour in the silent discharge of nitrogen - oxygen and water - air mixtures *Journal of Physics D: Applied Physics* **1997**, 30, 817.
- [91] N. Osawa and Y. Yoshioka, Generation of low-frequency homogeneous dielectric barrier discharge at atmospheric pressure *IEEE Transactions on Plasma Science* **2012**, 40, 2.
- [92] J. Y. Wang, G. G. Xia, A. Huang, S. L. Suib, Y. Hayashi, and H. Matsumoto, CO<sub>2</sub> Decomposition Using Glow Discharge Plasmas *Journal of Catalysis* **1999**, 185, 152.
- [93] S. Futamura and H. Kabashima, Synthesis Gas Production from CO<sub>2</sub> and H<sub>2</sub>O with Nonthermal Plasma *7th International Conference on Carbon Dioxide Utilization* **2004**, 119.
- [94] F. Brehmer, S. Welzel, M. C. M. van de Sanden, and R. and Engeln, CO and byproduct formation during CO<sub>2</sub> reduction in dielectric barrier discharges *J. Appl. Phys.* **2015**, 116, 123303.
- [95] G. Zheng, J. Jiang, Y. Wu, R. Zhang, and H. Hou, The Mutual Conversion of CO<sub>2</sub> and CO in Dielectric Barrier Discharge (DBD) *Plasma Chemistry and Plasma Processing* **2003**, 23, 59.
- [96] T. Tomai, T. Ito, and K. Terashima, Generation of dielectric barrier discharge in high-pressure N<sub>2</sub> and CO<sub>2</sub> environments up to supercritical conditions *The Joint Meeting of 7th APCPST and 17th SPSM* **2006**, 506–507, 409.
- [97] T. Tomai, K. Katahira, H. Kubo, Y. Shimizu, T. Sasaki, N. Koshizaki, and K. Terashima, Carbon materials syntheses using dielectric barrier discharge microplasma in supercritical carbon dioxide environments *The Journal of Supercritical Fluids* **2007**, 41, 404.
- [98] Y. Kim, M. S. Cha, W.-H. Shin, and Y.-H. Song, Characteristics of Dielectric Barrier Glow Discharges with a Low-Frequency Generator in Nitrogen *Journal of Korean Physical Society* **2003**, 43, 732.
- [99] S. Choi, H. N. Joo, H. Inho, K. L. Yong, H. H. Man, W. L. Sung, B. Hong-Koo, M. S. Kie, and L. Yong-Sik, Improvement of plasma uniformity using ZnO-coated dielectric barrier discharge in open air *The 33rd IEEE International Conference on Plasma Science* **2006**, 61.
- [100] Y. Guoqing, L. Anbang, F. Jian, W. Deyi, and L. Boxuan, Effect of Dielectric Surface Conductivity on Atmospheric Dielectric Barrier Discharge *2013 IEEE Conference on Electrical Insulation and Dielectric Phenomena (CEIDP)* **2013**, 278.

- 
- [101] F. Brehmer, Shining light on transient CO<sub>2</sub> plasma, *PhD Thesis Thesis*, Technical University of Eindhoven, **2015**.
- [102] T. Xin, J. G. Hellen, V. T. Martyn, A. G. Peter, and J. C. Whitehead, Dry reforming of methane over a Ni/Al<sub>2</sub>O<sub>3</sub> catalyst in a coaxial dielectric barrier discharge reactor *Journal of Physics D: Applied Physics* **2011**, *44*, 274007.
- [103] D. Dubois, N. Merbahi, O. Eichwald, M. Yousfi, and M. Benhenni, Electrical analysis of positive corona discharge in air and N<sub>2</sub>, O<sub>2</sub>, and CO<sub>2</sub> mixtures *Journal of Applied Physics* **2007**, *101*, 053304.
- [104] K. V. Kozlov, R. Brandenburg, H.-E. Wagber, A. M. Morozov, and P. Michel, Investigation of the filamentary and diffuse mode of barrier discharges in N<sub>2</sub>/O<sub>2</sub> mixtures at atmospheric pressure by cross-correlation spectroscopy *Journal of Physics D: Applied Physics* **2005**, *38*, 518.
- [105] O. Guaitella, F. Thevenet, C. Guillard, and A. Rousseau, Dynamic of the plasma current amplitude in a barrier discharge: influence of photocatalytic material *Journal of Physics D: Applied Physics* **2006**, *39*, 2964.
- [106] M. Ramakers, I. Michielsen, R. Aerts, V. Meynen, and A. Bogaerts, Effect of argon or helium on the CO<sub>2</sub> conversion in a dielectric barrier discharge *Plasma Processes and Polymers* **2015**, *12*, 755.
- [107] S. Kameshima, K. Tamura, Y. Ishibashi, and T. Nozaki, Pulsed dry methane reforming in plasma-enhanced catalytic reaction *Catalysis Today* **2015**, *256*, 67.
- [108] P. Audier, H. Rabat, A. Leroy, and D. Hong, Experimental investigation of a surface DBD actuator at atmospheric pressure in different N<sub>2</sub>/O<sub>2</sub> gas mixtures *Plasma Sources Science and Technology* **2014**, *23*, 065045.
- [109] Y. Akishev, G. Aponin, A. Balakiriev, M. Grushin, V. Karalnik, A. Petryakov, and N. Trushin, 'Memory' and sustention of microdischarges in a steady-state DBD: volume plasma or surface charge? *Plasma Sources Science and Technology* **2011**, *20*, 024005.
- [110] Y. S. Akishev, G. Aponin, A. Balakirev, M. Grushin, V. Karalnik, A. Petryakov, and N. Trushkin, Role of the volume and surface breakdown in a formation of microdischarges in a steady-state DBD *Eur. Phys. J. D* **2011**, *61*, 421.
- [111] D. Pai, S. Strauss, and K. Terashima, Surface dielectric barrier discharges exhibiting field emission at high pressures *Plasma Sources Science and Technology* **2014**, *23*, 025019.
- [112] D. Pai, S. Strauss, and K. Terashima, Field-emitting Townsend regime of surface dielectric barrier discharges emerging at high pressure up to supercritical conditions *Plasma Sources Science and Technology* **2015**, *24*, 025021.
- [113] G. W. Fox, O. S. Duffendack, and E. F. Barker, The Spectrum of CO<sub>2</sub> *Proc. Natl. Acad. Sci. USA* **1927**, *13*(5), 302.
- [114] T. Silva, N. Britun, T. Godfroid, and R. Snyders, Optical characterization of a microwave pulsed discharge used for dissociation of CO<sub>2</sub> *Plasma Sources Science and Technology* **2014**, *23*, 025009.
- [115] R. Brandenburg, M. Bogaczyk, S. Nemschokmichal, R. Tschiersch, M. Kettlitz, L. Stollenwerk, T. Hoder, R. Wild, K.-D. Weltmann, J. Meichsner, and H.-E.

- Wagner, Novel insights into the development of barrier discharges by advanced volume and surface diagnostics *Journal of Physics D: Applied Physics* **2013**, 46, 464015.
- [116] F. Fabry, G. Flamant, and L. Fulcheri, Carbon black processing by thermal plasma. Analysis of the particle formation mechanism *Chemical Engineering Science* **2001**, 56, 2123.
- [117] L. Fulcheri, N. Probst, G. Flamant, F. Fabry, E. Grivei, and X. Bourrat, Plasma processing: a step towards the production of new grades of carbon black *Third International Conference on Carbon Black* **2002**, 40, 169.
- [118] J. R. Fincke, R. P. Anderson, T. A. Hyde, and B. A. Detering, Plasma Pyrolysis of Methane to Hydrogen and Carbon Black *Industrial & Engineering Chemistry Research* **2002**, 41, 1425.
- [119] A. Kobayashi, K. Osaki, and C. Yamabe, Treatment of CO<sub>2</sub> gas by high-energy type plasma *3rd International Symposium on Applied Plasma Science (ISAPS 01)* **2002**, 65, 475.
- [120] W. Cho, S. H. Lee, W. S. Ju, Y. Baek, and J. K. Lee, Conversion of natural gas to hydrogen and carbon black by plasma and application of plasma carbon black *Catalysis Today* **2004**, 98, 633.
- [121] M. P. Srivastava and A. Kobayashi, Carbon Dioxide Decomposition by Plasma Methods and Application of High Energy and High Density Plasmas in Material Processing and Nanostructures *Transactions of JWRI* **2010**, 39, 11.
- [122] R. Pristavita, N. Y. Mendoza-Gonzalez, J. L. Meunier, and D. Berk, Carbon Blacks Produced by Thermal Plasma: the Influence of the Reactor Geometry on the Product Morphology *Plasma Chemistry and Plasma Processing* **2010**, 30, 267.
- [123] H. J. Gallon, X. Tu, M. V. Twigg, and J. C. Whitehead, Plasma-assisted methane reduction of a NiO catalyst – Low temperature activation of methane and formation of carbon nanofibres *Applied Catalysis B: Environmental* **2011**, 106, 616.
- [124] X. Tu and J. C. Whitehead, Plasma dry reforming of methane in an atmospheric pressure AC gliding arc discharge: Co-generation of syngas and carbon nanomaterials *International Journal of Hydrogen Energy* **2014**, 39, 9658.
- [125] S. Mahammadunnisa, E. L. Reddy, D. Ray, C. Subrahmanyam, and J. C. Whitehead, CO<sub>2</sub> reduction to syngas and carbon nanofibres by plasma-assisted in situ decomposition of water *International Journal of Greenhouse Gas Control* **2013**, 16, 361.
- [126] G. Hirson, G. F. Shouse, and M. W. SHUEY, Systems and methods of plasma partial dissociation of carbon dioxide, water, and carbonaceous matter, WO 2015089069 A1, **2015**.
- [127] S. Mori, N. Matsuura, L. L. Tun, and M. Suzuki, Direct Synthesis of Carbon Nanotubes from Only CO<sub>2</sub> by a Hybrid Reactor of Dielectric Barrier Discharge and Solid Oxide Electrolyser Cell *Plasma Chemistry and Plasma Processing* **2015**, 36, 231.

- [128] G. Petitpas, J. D. Rollier, A. Darmon, J. Gonzalez-Aguilar, R. Metkemeijer, and L. Fulcheri, A comparative study of non-thermal plasma assisted reforming technologies *Int Conf on Materials for Hydrogen Energy: Solar Hydrogen (ICMHE 2004)* **2007**, 32, 2848.
- [129] M. Li, G. Xu, Y. Tian, L. Chen, and H. Fu, Carbon Dioxide Reforming of Methane Using DC Corona Discharge Plasma Reaction *The Journal of Physical Chemistry A* **2004**, 108, 1687.
- [130] D. Mei, Y. L. He, S. Liu, J. Yan, and X. Tu, Optimization of CO<sub>2</sub> Conversion in a Cylindrical Dielectric Barrier Discharge Reactor Using Design of Experiments *Plasma Processes and Polymers* **2015**, 13, 544.
- [131] S. L. Brock, M. Marquez, S. L. Suib, Y. Hayashi, and H. Matsumoto, Plasma Decomposition of CO<sub>2</sub> in the Presence of Metal Catalysts *Journal of Catalysis* **1998**, 180, 225.
- [132] S. L. Suib, S. L. Brock, M. Marquez, J. Luo, H. Matsumoto, and Y. Hayashi, Efficient Catalytic Plasma Activation of CO<sub>2</sub>, NO, and H<sub>2</sub>O *The Journal of Physical Chemistry B* **1998**, 102, 9661.
- [133] A. Ozkan, T. Dufour, T. Silva, N. Britun, R. Snyders, A. Bogaerts, and F. Reniers, The influence of power and frequency on the filamentary behavior of a flowing DBD—application to the splitting of CO<sub>2</sub> *Plasma Sources Science and Technology* **2016**, 25, 025013.
- [134] K. Jogan, A. Mizuno, T. Yamamoto, and J. Chang, The effect of residence time on the CO<sub>2</sub> reduction from combustion flue gases by an AC ferroelectric packed bed reactor *Industry Applications, IEEE Transactions on* **1993**, 29, 876.
- [135] P. Nikolaev, M. J. Bronikowski, R. K. Bradley, F. Rohmund, D. T. Colbert, K. A. Smith, and R. E. Smalley, Gas-phase catalytic growth of single-walled carbon nanotubes from carbon monoxide *Chemical Physics Letters* **1999**, 313, 91.
- [136] P. Nikolaev, Gas-phase production of single-walled carbon nanotubes from carbon monoxide: a review of the hipco process. *J Nanosci Nanotechnol* **2004**, 4, 307.
- [137] A. G. Nasibulin, A. S. Anisimov, P. V. Pikhitsa, H. Jiang, D. P. Brown, M. Choi, and E. I. Kauppinen, Investigations of NanoBud formation *Chemical Physics Letters* **2007**, 446, 109.
- [138] A. S. Anisimov, A. G. Nasibulin, H. Jiang, P. Launois, J. Cambedouzou, S. D. Shandakov, and E. I. Kauppinen, Mechanistic investigations of single-walled carbon nanotube synthesis by ferrocene vapor decomposition in carbon monoxide *Carbon* **2010**, 48, 380.
- [139] E. Plönjes, P. Palm, G. Babu Viswanathan, V. V. Subramaniam, I. V. Adamovich, W. R. Lempert, H. L. Fraser, and J. William Rich, Synthesis of single-walled carbon nanotubes in vibrationally non-equilibrium carbon monoxide *Chemical Physics Letters* **2002**, 352, 342.
- [140] Y. Su, Z. Yang, H. Wei, E. S.-W. Kong, and Y. Zhang, Synthesis of single-walled carbon nanotubes with selective diameter distributions using DC arc discharge under CO mixed atmosphere *Applied Surface Science* **2011**, 257, 3123.

- [141] Z. Bo, Y. Yang, J. Chen, K. Yu, J. Yan, and K. Cen, Plasma-enhanced chemical vapor deposition synthesis of vertically oriented graphene nanosheets *Nanoscale* **2013**, 5, 5180.
- [142] S. Mori and M. Suzuki, Effect of oxygen and hydrogen addition on the low-temperature synthesis of carbon nanofibers using a low-temperature CO/Ar DC plasma *Diamond and Related Materials* **2008**, 17, 999.
- [143] S. Mori and M. Suzuki, The Role of C<sub>2</sub> in Low Temperature Growth of Carbon Nanofibers *Journal of Chemical Engineering of Japan* **2009**, 42, S249.
- [144] S. Mori and M. Suzuki, Characterization of carbon nanofibers synthesized by microwave plasma-enhanced CVD at low-temperature in a CO/Ar/O<sub>2</sub> system *Diamond and Related Materials* **2009**, 18, 678.
- [145] S. Mori and M. Suzuki, Catalyst-free low-temperature growth of carbon nanofibers by microwave plasma-enhanced CVD *The proceedings of the 1st International Conference on Microelectronics and Plasma Technology (ICMAP 2008)* **2009**, 517, 4264.
- [146] Y. Anekawa, S. Mori, and M. Suzuki, Synthesis of graphene-based conductive thin films by plasma-enhanced chemical vapor deposition in a CO/H<sub>2</sub> microwave discharge system *The 21st International Symposium on Plasma Chemistry (ISPC-21)* **2013**,
- [147] A. D. C. Permana, A. Kameyama, M. Suzuki, and S. Mori, Synthesis of carbon nanowalls by plasma-enhanced chemical vapor deposition and their rapid intercalation behaviour as lithium ion capacitor anode material *The 22nd International Symposium on Plasma Chemistry (ISPC-22)*
- [148] R. Geiger and D. Staack, Analysis of solid products formed in atmospheric non-thermal carbon monoxide plasma *Journal of Physics D: Applied Physics* **2011**, 44, 274005.
- [149] C. Gorse, M. Cacciatore, and M. Capitelli, Kinetic processes in non-equilibrium carbon monoxide discharges. I. Vibrational kinetics and dissociation rates *Chemical Physics* **1984**, 85, 165.
- [150] A. Vesel, R. Zaplotnik, J. Iacono, M. Balat-Pichelin, and M. Mozetic, A Catalytic Sensor for Measurement of Radical Density in CO<sub>2</sub> Plasmas *Sensors* **2012**, 12, 16168.
- [151] Z. Machala, M. Janda, K. Hensel, I. Jedlovský, L. Leštinská, V. Foltin, V. Martišovitéš, and M. Morvová, Emission spectroscopy of atmospheric pressure plasmas for bio-medical and environmental applications *Journal of Molecular Spectroscopy* **2007**, 243, 194.
- [152] Y. Babou, P. Rivière, M. Y. Perrin, and A. Soufiani, Spectroscopic study of microwave plasmas of CO<sub>2</sub> and CO<sub>2</sub>-N<sub>2</sub> mixtures at atmospheric pressure *Plasma Sources Science and Technology* **2008**, 17, 045010.
- [153] D. L. Quang, Y. Babou, and P. Andre, Investigations of a microwave plasma source operating with air, N<sub>2</sub>, CO<sub>2</sub> and argon gases *IOP Conference Series: Materials Science and Engineering* **2012**, 29, 012009.

- 
- [154] P. Caubet and G. Dorthe, Origin of C<sub>2</sub> high-pressure bands observed in the products of a microwave discharge through CO *Chemical Physics Letters* **1994**, 218, 529.
- [155] N. Krstulovic, U. Cvelbar, A. Vesel, S. Milosevic, and M. Mozetic, An Optical-Emission-Spectroscopy characterization of oxygen plasma during the oxidation of aluminium foils *Materials and Technology* **2009**, 43, 245.
- [156] M. Mozetic, U. Cvelbar, A. Vesel, N. Krstulovic, and S. Milosevic, Interaction of Oxygen Plasma With Aluminium Substrates *Plasma Science, IEEE Transactions on* **2008**, 36, 868.
- [157] D. Kozak, E. Shibata, A. Iizuka, and T. Nakamura, Growth of carbon dendrites on cathode above liquid ethanol using surface plasma *Carbon* **2014**, 70, 87.
- [158] M. P. Danilae, E. A. Bogoslov, O. G. Morozov, A. R. Nasybullin, D. M. Pashin, and Y. E. Pol'skii, Obtaining Carbon Dendrites from the Products of Conversion of Polymer Materials *Journal of Engineering Physics and Thermophysics* **2015**, 88, 774.
- [159] C. Cunha, S. Panseri, D. Iannazzo, A. Piperno, A. Pistone, M. Fazio, A. Russo, M. Marcacci, and S. Galvagno, Hybrid composites made of multiwalled carbon nanotubes functionalized with Fe<sub>3</sub>O<sub>4</sub> nanoparticles for tissue engineering applications *Nanotechnology* **2012**, 23, 465102.
- [160] M. J. Lipp, W. J. Evans, B. J. Baer, and C. S. Yoo, High-energy-density extended CO solid *Nat Mater* **2005**, 4, 211.
- [161] W. J. Evans, M. J. Lipp, C. S. Yoo, H. Cynn, J. L. Herberg, R. S. Maxwell, and M. F. Nicol, Pressure-Induced Polymerization of Carbon Monoxide: Disproportionation and Synthesis of an Energetic Lactonic Polymer *Chemistry of Materials* **2006**, 18, 2520.
- [162] P. K. Chu and L. Li, Characterization of amorphous and nanocrystalline carbon films *Materials Chemistry and Physics* **2006**, 96, 253.
- [163] S. Praver and R. J. Nemanich, Raman spectroscopy of diamond and doped diamond *Philosophical Transactions of the Royal Society of London A: Mathematical, Physical and Engineering Sciences* **2004**, 362, 2537.
- [164] Y.-S. Li, J. S. Church, and A. L. Woodhead, Infrared and Raman spectroscopic studies on iron oxide magnetic nano-particles and their surface modifications *Journal of Magnetism and Magnetic Materials* **2012**, 324, 1543.
- [165] M. Ceppatelli, A. Serdyukov, R. Bini, and H. J. Jodl, Pressure Induced Reactivity of Solid CO by FTIR Studies *The Journal of Physical Chemistry B* **2009**, 113, 6652.
- [166] D. J. Babu, S. Yadav, T. Heinlein, G. Cherkashinin, and J. Â. J. Schneider, Carbon Dioxide Plasma as a Versatile Medium for Purification and Functionalization of Vertically Aligned Carbon Nanotubes *The Journal of Physical Chemistry C* **2014**, 118, 12028.
- [167] A. Fridman, A. F. Gutsol, and Y. I. Cho, Production and uses of carbon suboxides, US 7,569,203 B2, **2009**.

- [168] F. Pourfayaz, Y. Mortazavi, A. A. Khodadadi, and S.-H. Jafari, Rapid and enhanced functionalization of MWCNTs in a dielectric barrier discharge plasma in presence of diluted CO<sub>2</sub> *Applied Physics A* **2012**, 106, 829.
- [169] P. Gushin, Plasma-catalytic conversion of CO<sub>2</sub> and CH<sub>4</sub> in the Microwave Discharge (*in russian*), *PhD-thesis Thesis*, Gubkin Russian State Oil and Gas University, Moscow, **2008**.
- [170] J. P. Borra, N. Jidenko, J. Hou, and A. Weber, Vaporization of bulk metals into single-digit nanoparticles by non-thermal plasma filaments in atmospheric pressure dielectric barrier discharges *Journal of Aerosol Science* **2015**, 79, 109.
- [171] T. V. Pfeiffer, J. Feng, and A. Schmidt-Ott, New developments in spark production of nanoparticles *Advanced Powder Technology* **2014**, 25, 56.
- [172] L. Lin and Q. Wang, Microplasma: A New Generation of Technology for Functional Nanomaterial Synthesis *Plasma Chemistry and Plasma Processing* **2015**, 35, 925.
- [173] I. Belov, S. Paulussen, and A. Boagaerts, Appearance of a conductive carbonaceous coating in a CO<sub>2</sub> dielectric barrier discharge and its influence on the electrical properties and the conversion efficiency *Plasma Sources Science and Technology* **2016**, 25, 015023.
- [174] H. Höft, M. Kettlitz, K. D. Weltmann, and R. Brandenburg, The bidirectional character of O<sub>2</sub> concentration in pulsed dielectric barrier discharges in O<sub>2</sub>/N<sub>2</sub> gas mixtures *Journal of Physics D: Applied Physics* **2014**, 47, 455202.
- [175] A. Drenik, L. Salamon, R. Zaplotnik, A. Vesel, and M. Mozetič, Erosion of amorphous carbon layers in the afterglow of oxygen microwave plasma *Vacuum* **2013**, 98, 45.
- [176] A. Vesel, K. Eleršič, M. Modic, I. Junkar, and M. Mozetič, Formation of Nanocones on Highly Oriented Pyrolytic Graphite by Oxygen Plasma *Materials* **2014**, 7, 2014.
- [177] Y. Tamaura and M. Tahata, Complete reduction of carbon dioxide to carbon using cation-excess magnetite *Nature* **1990**, 346, 255.
- [178] T. Kodama, T. Sano, T. Yoshida, M. Tsuji, and Y. Tamaura, CO<sub>2</sub> decomposition to carbon with ferrite-derived metallic phase at 300 °C *Carbon* **1995**, 33, 1443.
- [179] K. Ehrensberger, R. Palumbo, C. Larson, and A. Steinfeld, Production of Carbon from Carbon Dioxide with Iron Oxides and High-Temperature Solar Energy *Industrial & Engineering Chemistry Research* **1997**, 36, 645.
- [180] A. Ozkan, T. Dufour, G. Arnoult, P. De Keyzer, A. Bogaerts, and F. Reniers, CO<sub>2</sub>–CH<sub>4</sub> conversion and syngas formation at atmospheric pressure using a multi-electrode dielectric barrier discharge *Journal of CO<sub>2</sub> Utilization* **2015**, 9, 74.
- [181] R. Aerts, R. Snoeckx, and A. Bogaerts, In-Situ Chemical Trapping of Oxygen in the Splitting of Carbon Dioxide by Plasma *Plasma Processes and Polymers* **2014**, 11, 985.
- [182] H.-H. Kim, Y. Teramoto, A. Ogata, H. Takagi, and T. Nanba, Plasma Catalysis for Environmental Treatment and Energy Applications *Plasma Chemistry and Plasma Processing* **2016**, 36, 45.

- 
- [183] D. Mariotti, T. Belmonte, J. Benedikt, T. Velusamy, G. Jain, and V. Švrček, Low-Temperature Atmospheric Pressure Plasma Processes for “Green” Third Generation Photovoltaics *Plasma Processes and Polymers* **2016**, 13, 70.
- [184] J. Gruenwald, K. Fricke, M. Fröhlich, and M. Polak, Deposition of Copper Oxide Coatings With an Atmospheric Pressure Plasma Source: I – Characterization of the Plasma *Plasma Processes and Polymers* **2016**, 946.
- [185] J. Gruenwald, K. Fricke, M. Fröhlich, J. F. Kolb, and M. Polak, Deposition of Copper Oxide Coatings with an Atmospheric Pressure Plasma Source: II – Characterization of the Films *Plasma Processes and Polymers* **2016**, 13, 766.
- [186] D. Mariotti, A. C. Bose, and K. Ostrikov, Atmospheric-Microplasma-Assisted Nanofabrication: Metal and Metal-Oxide Nanostructures and Nanoarchitectures *IEEE Transactions on Plasma Science* **2009**, 37, 1027.
- [187] J. Fang, L. Schlag, S.-C. Park, T. Stauden, J. Pezoldt, P. Schaaf, and H. O. Jacobs, Approaching Gas Phase Electrodeposition: Process and Optimization to Enable the Self-Aligned Growth of 3D Nanobridge-Based Interconnects *Advanced Materials* **2016**, 28, 1770.
- [188] B. Arumugam Chandra, S. Yoshiki, M. Davide, S. Takeshi, T. Kazuo, and K. Naoto, Flow rate effect on the structure and morphology of molybdenum oxide nanoparticles deposited by atmospheric-pressure microplasma processing *Nanotechnology* **2006**, 17, 5976.
- [189] A. A. Garamoon, F. F. Elakshar, A. M. Nossair, and E. F. Kotp, Experimental study of ozone synthesis *Plasma Sources Science and Technology* **2002**, 11, 254.
- [190] F. Tanaka, T. Iwaishi, T. Sakugawa, and H. Akiyama, Influence of gas flow rate and pressure in reactors on ozone production using a compact pulsed power generator *IEEE Pulsed Power Conference* **2011**, 1570.
- [191] S. Boonduang, S. Limsuwan, W. Kongsri, and P. Limsuwan, Effect of Oxygen Pressure and Flow Rate on Electrical Characteristic and Ozone Concentration of a Cylinder-Cylinder DBD Ozone Generator *Procedia Engineering* **2012**, 32, 936.
- [192] D. C. Seok, H. Y. Jeong, Y. H. Jung, and T. Lho, Optimizing Factors on High Concentration of Ozone Production with Dielectric Barrier Discharge *Ozone: Science & Engineering* **2015**, 37, 221.
- [193] S. A. Stepanyan, A. Y. Starikovskiy, N. A. Popov, and S. M. Starikovskaia, A nanosecond surface dielectric barrier discharge in air at high pressures and different polarities of applied pulses: transition to filamentary mode *Plasma Sources Science and Technology* **2014**, 23, 045003.
- [194] S. A. Shcherbanev, S. A. Stepanyan, N. A. Popov, and S. M. Starikovskaia, Dielectric barrier discharge for multi-point plasma-assisted ignition at high pressures *Philosophical Transactions of the Royal Society A: Mathematical, Physical and Engineering Sciences* **2015**, 373, 20140342.
- [195] S. V. Pancheshnyi, D. A. Lacoste, A. Bourdon, and C. O. Laux, Ignition of Propane-Air Mixtures by a Repetitively Pulsed Nanosecond Discharge *IEEE Transactions on Plasma Science* **2006**, 34, 2478.

- [196] P. Čermák, J. Varga, P. Macko, V. Martišovič, and P. Veis, Study of nitrogen molecular systems observed in NIR spectra in DBD at near and over atmospheric pressure *28th ICPIG Prague, Czech Republic* **2007**,
- [197] I. Belov, J. Vanneste, M. Aghaee, S. Paulussen, and A. Bogaerts, Synthesis of Micro- and Nanomaterials in CO<sub>2</sub> and CO Dielectric Barrier Discharges *Plasma Processes and Polymers* **2017**, 3, 1600065.
- [198] H. Höft, M. Kettlitz, T. Hoder, K. D. Weltmann, and R. Brandenburg, The influence of O<sub>2</sub> content on the spatio-temporal development of pulsed driven dielectric barrier discharges in O<sub>2</sub>/N<sub>2</sub> gas mixtures *Journal of Physics D: Applied Physics* **2013**, 46, 095202.
- [199] E. Thimsen and P. Biswas, Nanostructured photoactive films synthesized by a flame aerosol reactor *AIChE Journal* **2007**, 53, 1727.
- [200] K. De Bleecker, A. Bogaerts, and W. Goedheer, Role of the thermophoretic force on the transport of nanoparticles in dusty silane plasmas *Physical Review E* **2005**, 71, 066405.
- [201] F. Brehmer, S. Welzel, B. L. M. Klarenaar, H. J. v. d. Meiden, M. C. M. v. d. Sanden, and R. Engeln, Gas temperature in transient CO<sub>2</sub> plasma measured by Raman scattering *Journal of Physics D: Applied Physics* **2015**, 48, 155201.
- [202] B. Jean-Pascal, Nucleation and aerosol processing in atmospheric pressure electrical discharges: powders production, coatings and filtration *Journal of Physics D: Applied Physics* **2006**, 39, R19.
- [203] A. Ozkan, T. Dufour, T. Silva, N. Britun, R. Snyders, F. Reniers, and A. Bogaerts, DBD in burst mode: solution for more efficient CO<sub>2</sub> conversion? *Plasma Sources Science and Technology* **2016**, 25, 055005.
- [204] A. Berthelot and A. Bogaerts, Modeling of CO<sub>2</sub> Splitting in a Microwave Plasma: How to Improve the Conversion and Energy Efficiency? *J. Phys. Chem. C* **2017**, 121, 8236.
- [205] T. Kozák and A. Bogaerts, Splitting of CO<sub>2</sub> by vibrational excitation in non-equilibrium plasmas: a reaction kinetics model *Plasma Sources Science and Technology* **2014**, 23, 045004.
- [206] N. den Harder, D. C. M. van den Bekerom, R. S. Al, M. F. Graswinckel, J. M. Palomares, F. J. J. Peeters, S. Ponduri, T. Minea, W. A. Bongers, M. C. M. van de Sanden, and G. J. van Rooij, Homogeneous CO<sub>2</sub> conversion by microwave plasma: Wave propagation and diagnostics *Plasma Processes and Polymers* **2016**, e1600120.
- [207] S. M. Chun, D. H. Choi, J. B. Park, and Y. C. Hong, Optical and Structural Properties of ZnO Nanoparticles Synthesized by CO<sub>2</sub> Microwave Plasma at Atmospheric Pressure *Journal of Nanoparticles* **2014**, 2014, 7.
- [208] A. Bogaerts, A. Berthelot, S. Heijkers, S. Kolev, R. Snoeckx, S. Sun, G. Trenchev, K. Van Laer, and W. Wang, CO<sub>2</sub> conversion by plasma technology: Insights from modeling the plasma chemistry and plasma reactor design *Plasma Sources Science and Technology* **2017**, 26, 063001.

- 
- [209] S. Mori and L. L. Tun, Synergistic CO<sub>2</sub> conversion by hybridization of dielectric barrier discharge and solid oxide electrolyser cell *Plasma Processes and Polymers* **2016**, *14*, e1600153.
- [210] J. C. Whitehead, Plasma-catalysis: the known knowns, the known unknowns and the unknown unknowns *Journal of Physics D: Applied Physics* **2016**, *49*, 243001.
- [211] S. Mori, Synthesis of nanocarbon materials by PECVD: challenges to direct synthesis via CO<sub>2</sub> reduction using plasma-SOEC hybrid reactor *The 22nd International Symposium on Plasma Chemistry (ISPC22)* **2015**,
- [212] K. Zhang, G. Zhang, X. Liu, A. N. Phan, and K. Luo, A Study on CO<sub>2</sub> Decomposition to CO and O<sub>2</sub> by the Combination of Catalysis and Dielectric-Barrier Discharges at Low Temperatures and Ambient Pressure *Industrial & Engineering Chemistry Research* **2017**, *56*, 3204.
- [213] R. T. J. Porter, M. Fairweather, M. Pourkashanian, and R. M. Woolley, The range and level of impurities in CO<sub>2</sub> streams from different carbon capture sources *International Journal of Greenhouse Gas Control* **2015**, *36*, 161.
- [214] R. Snoeckx, S. Heijckers, K. Van Wesenbeeck, S. Lenaerts, and A. Bogaerts, CO<sub>2</sub> conversion in a dielectric barrier discharge plasma: N<sub>2</sub> in the mix as a helping hand or problematic impurity? *Energy & Environmental Science* **2016**, *9*, 999.
- [215] M. Dors, T. Izdebski, M. Tański, and J. Mizeraczyk, The influence of hydrogen sulphide and configuration of a dbd reactor powered with nanosecond high voltage pulses on hydrogen production from biogas *Eur. Chem. Bull.* **2014**, *8*, 798.

